



university of
 groningen

faculty of science
 and engineering

kapteyn astronomical
 institute

RIJKSUNIVERSITEIT GRONINGEN

BACHELOR THESIS

Imaging techniques for archival ALMA data
 illustrating stages of planetary formation for
 use in planetaria.

Comparisons between techniques used for outreach and communication or
 research

8 JULY 2022

Author:
 Floor van der Kolk
 (S3986225)

Supervisor:
 Jake Noel-Storr
 Veronica Allen

Contents

1	Introduction	4
2	Scientific background	7
2.1	Different Phases in star and planet formation	7
2.2	Observations of these classes	7
2.3	Planet formation	9
2.4	Observational methods for star and planet formation	12
3	Technical background	14
4	Communication background and choices	17
4.1	Imaging using colors	17
4.2	Medium of presenting images	17
4.3	The talk	18
5	Selected objects	21
6	Method	24
7	Results	26
7.1	Moment maps	26
7.2	Continuum	31
7.3	Final images	38
7.4	Guidelines for the script of the show on planet formation	43
8	Discussion	47
8.1	Moment maps	47
8.2	Continuum images	50
8.3	Final images	55
9	Conclusions	57
10	Appendix	65
10.1	Images	65
10.2	Instruction data reduction	68
10.3	Script for imaging	80
10.4	Script for implementing data in planetarium	84

Abstract

A planetarium is a useful way to present new data to the general public as it results in greater learning. An interesting approach for a planetarium show, is to communicate how astronomers gather data from across the sky to confirm the theories on planet formation to the audience.

The stages that need to be shown to explain planet formation are the molecular cloud, the rotating gaseous disk that points to the formation of a disk, the structures in the dust disk made by planets, and a planetary system. The Atacama Large Millimeter/submillimeter Array (ALMA) made it possible to have high resolution observations of protoplanetary disks. So, in this thesis ALMA data will be used to produce moment maps using *immoments* to show the rotating gaseous disk and produce continuum images using *tclean* to show structured disks. In this thesis I experimentally determine the best settings for cleaning a continuum image looking at the visual appearance and the numerical properties of the image. I came to the conclusion that weak lines spotted with *plotms* can be neglected for outreach purposes, as well as the deconvolver settings and the primary beam correction. Briggs weighting with a robust parameter of 0.5 is generally a safe choice as it has the highest signal-to-noise ratio and interactive cleaning should be tried if time allows. This part of the thesis resulted in a set of instructions for imaging ALMA data together with a script for imaging and implementing images in the planetarium. I compared the final images of both the moment maps and the continuum images to the ones produced by literature.

This thesis also creates guidelines on communicating astronomy. Attention needs to be paid to colors and adding scaling to the figures for comprehending astronomical images. Generally a red (and orange) color scheme is recommended and the selected colors should be explained. Concerning the communication of science to the audience, it is advised to use storytelling techniques. This part of the thesis resulted set up for a script for a planetarium show on star and planet formation.

1 Introduction

Curiosity about the formation of the planets in our solar system has driven scientists, especially astronomers, to come up with models and theories on planet formation based on the laws of physics. Nowadays, in scientific literature, these theories are being confirmed, extended, or even changed based on observations of planetary systems at different stages of their evolution. But why is this information not commonly communicated to the general public? Science communication is of great importance as it is the link between the scientific community and the general public, it brings scientific developments to the attention of the public and helps the government develop science-based policies. Besides, curiosity about planet formation has not only driven astronomers, it also gave rise to philosophical discussions for the general public. Questions the audience might wonder about are often related to the fundamental question: *‘Is there life elsewhere in the universe?’* (Christensen 2007). Which often leads to the question *‘Is the earth a unique planet?’*. The theories on planet formation developed by astronomers can be communicated to the public, but often the question remains: *‘How do you know?’*. This thesis aims to guide science communicators to explain how astronomers gather data from the night sky to confirm their theories on planet formation. Which gives rise to one of my driving questions: *‘How can we communicate to the general public how astronomers gather data and use it to form theories (on planet formation)?’*

To answer this question, I will address the scientific background of planet formation, the technical background and the communication background. The scientific background of star and planet formation must be understood so that the different stages of evolution can be explained to the audience. One of stages I will be imaging, is the rotating gaseous envelope, which can be observed with the help of line transition and points to the formation of a disk as a consequence of conservation of angular momentum. Another important stage I will image is the continuum, produced by the heated dust in the disk, which shows the different structures caused by forming planets. The Atacama Large Millimeter/submillimeter Array (ALMA) is a radio observatory which is useful to image these stages, as both the line and continuum emission is in the millimeter to sub-millimeter wavelengths. ALMA has 66 antennas that work together to produce images of high resolution and has been revolutionary in showing planetary disk structures (ALMA 2021).

To produce the best images for the planetarium show, different settings of the imaging function (*tlean* and *immoments*) are examined. I will study the visual appearance of the images as well as the numerical properties of the images. The final images are also compared to the images produced in literature to show the difference between imaging for research purposes and imaging for communication purposes. With the goal of simplifying the imaging process for a non-expert, we ensure that the resulting images, while not identical to previous published images, are appropriate for the public and display the desired astronomical concepts.

Besides understanding the scientific, technical and communication background it is important for a science communicator to choose a suitable communication medium, for example a planetarium. Yu, K. Sahami, V. Sahami, et al. 2015 and Yu, K. Sahami, Denn, et al. 2016 explain that a immersive full dome planetarium show result in greater attention and reduces cognitive loads because of the large display and the wide field of view. Because of that, both groups concluded that a lecture which shows images in a full dome planetarium show, leads to greater learning compared to the exact same lecture with the images shown on a flat screen. Alt and Shaw 1984 give three qualities visitors would like in their ideal exhibition; it should make

the subject come alive, it should be memorable, and it should be quickly understood. This all points to the fact that a planetarium is a useful medium for science communication (especially for astronomy), that's why this thesis focuses on the use of a planetarium, as it will be useful to visualize how different patches of the night sky are used for doing research.

The Data2Dome project of ESO recognized a problem with a planetarium as communication medium. Namely implementing new content to present it in a planetarium takes days or even weeks, while the new findings are posted the very same day on websites of research institutions, blogs, and the news. So to make a planetarium a relevant way of communicating new findings, the implementation of new content needs to be optimized (Christensen 2007). This thesis will be a step in facilitating the use of a planetarium for presenting new data or content, as I will create new guidelines for fellow astronomers and planetarium operators for formatting data so it can be implemented in the planetarium. This gives rise to the question: *'What is a simple way for data to be imaged so it can be implemented in a planetarium show and is understandable for the audience?'*

Science communication does not only require knowledge about science but also about visual communication. Images are especially important in astronomy as it historically is the way astronomers record our discoveries about the universe and the images give a 'Wow'-factor, which is important for non-experts. In this thesis I will therefore experimentally determine the best way to image ALMA observations for clear communication to the general public. I will find the right ALMA data, reduce, and format it properly and produce a set of instructions while doing so, so other astronomers can easily reduce ALMA data and use it in a planetarium. I will explain how astronomy can be communicated to the general public and will produce guidelines for a show on planet formation with this knowledge. The end result will be a new planetarium show for the general public about how astronomers use the night sky to gather data and form theories on star and planet formation, so I can answer my main question: *'How can communicators produce a planetarium show using ALMA data to explain to the audience how the theory behind planet formation is produced?'*

By using recent ALMA observations in this planetarium show about planet formation, the audience will increase their scientific knowledge while having an incredible visual experience. The audience will improve their critical thinking and become able to discuss subjects concerning astronomy. They will get to understand how astronomers form theories using observations, but also learn that it's still an ongoing field of research. The planetarium show specifically will increase the audience's knowledge about and interest in planet formation.

This thesis consists of eight chapters, the Scientific background (Chapter 2) explains the theory behind the different evolutionary phases and the observables during star and planet formation. Technical background (Chapter 3) explains the concepts behind ALMA data reduction. Communication background (Chapter 4) explains what to focus on when imaging data for and explaining astronomy to the general public. In Chapter 4 I will also substantiate certain choices I made during the process of imaging and writing a script. In Chapter 5, Selected objects, I will discuss the objects that I will be imaging in this thesis. In Chapter 6 I explain the method of the data reduction processes, that are explained in Chapter 3 and explain how I took measurements of the produced images. In Results (Chapter 7) the images produced are shown together with tables that list certain properties of the images. Additionally guidelines for a script for the planetarium show are given in this section. In the discussion (Chapter 8) I will discuss which image

parameters are best for communicating star and planet formation theories based on the visual appearance as well as the measurements, and compare my final images to the once produced in other literature. Chapter 9 summarizes the conclusions. Finally, in the appendix there are data reduction and imaging scripts for formatting ALMA data, a script on how to implement images in a planetarium using the software SkySkan and a detailed set of instructions for imaging ALMA data.

2 Scientific background

2.1 Different Phases in star and planet formation

Star formation starts off in a molecular cloud, where prestellar cores form within dense filaments (André et al. 2010). If the the core is dense ($n \sim 10^4 - 10^5 \text{ cm}^3$) and cold ($T \sim 20 - 30 \text{ K}$) ('t Hof 2019) enough so that the gas pressure will not be strong enough to balance the gravity, the core collapses. This so called Jeans instability will occur when the mass of the core succeed the Jeans mass and gravity dominates over gas pressure. The temperature and pressure rise and a hydrostatic stellar core is produced. As the temperature of the core rises even more, it experiences another collapse which then forms the protostar according to numerically solved equations governing the collapse by Larson 1969. During this collapse there are turbulent motions of the gas or a gravitational torque between overdensities in the cloud which give the cloud and core angular momentum (Tobin, Sheehan, et al. 2020). During the collapse of the core, material moves inward. To conserve the angular momentum, a rotating disk of gas and dust is formed which is surrounded by an in-falling envelope (Terebey, Shu, and Cassen 1984). When material accretes to the protostar it first falls onto the disk to be transported to the protostar (Larson 1969).

The early evolution of the newly formed protostar can be divided into four stages. Class 0 is the first stage in which the rotational disk is formed, Murillo et al. 2013 confirmed the presents a disk with Keplerian velocity in the Class 0 source VLA1623A. The protostar is still fully embedded in the massive envelope. Jørgensen et al. 2009 observed 20 Class 0 and Class I sources and determined the mass of the disk and the envelope. The disk of the Class 0 stars is typically 1 to 10% of the corresponding envelope. Most of the accretion occurs during this stage, which results in the most prominent outflow jets (Maury et al. 2019) (Tobin, Hartmann, et al. 2012). During Class I, accretion via the disk onto the protostar occurs and causes the mass of the envelope to decrease and that of the protostar to grow. Jørgensen et al. 2009 observed the disk mass of a Class I star to be 20 to 60% of the corresponding envelope mass. The outflows have a wider opening angle and are less powerful, as most of the mass of the envelope has already accreted to the disk and protostar (Arce and Sargent 2006). In Class 0 the disks are hardly visible because the envelope is prominent, but in Class I the disk is less embedded in the envelope so it becomes more visible (Łukasz Tychoniec 2021). The disks surrounding the Class 0 and Class I protostars are generically referred to as protostellar disks according to Tobin, Sheehan, et al. 2020. During Class II the envelope is fully dissipating away, leaving a well-defined, clear disk in which structures may occur (Tobin, Sheehan, et al. 2020). During this stage, the outflows are very weak since very little accretion from the envelope is taking place. Sometimes a fifth class is used between Class I and Class II which is called the Flat spectrum, based on their Spectral energy distribution (Tobin, Sheehan, et al. 2020). Finally, in Class III most dust has been accreted to the planetesimals starting to form planets, and most of the gas has been dissipated away (Whitney et al. 2003). The disks surrounding the Class II and Class III protostars are often called protoplanetary disks according to Tobin, Sheehan, et al. 2020.

2.2 Observations of these classes

Different physical properties can be used to distinguish between these classes, using images, spectral index, effective temperatures and spectral energy distributions (SED).

The central star itself emits mainly in the optical band, but in the early stages the star is fully embedded in the envelope, making it difficult to observe. Astronomers are interested in observing the surrounding disk and envelope that contain lots of information about the protostar. To observe the disk properties three different types of observation can be used. First of all you can observe scattered light, which is light reflected by small dust grains around the star. These observations depend on the distribution of grains and their albedo which in turn depends on the size, shape and composition of the grains. With this observation method it's difficult to observe material close to the star because of the lack of contrast and also difficult to observe material far out since the stellar radiation field is not strong enough at large distances. Secondly, the continuum emission of the dust grains can be observed where the dust grains are heated by the central star and emit as a blackbody of around 20/30K (Tobin, Sheehan, et al. 2020). This observation method does not have stellar contrast limitations. Finally, you can also observe spectral line emission, when a photon is emitted by an atom or molecule as an electron loses energy. This observation method only traces the gas, and is used to determine the chemical composition and temperature of the gas and uses Doppler shift to measure the kinematics (S. M. Andrews 2020).

Lada and Wilking 1984 used the infrared spectral index to distinguish the different classes, which gives the slope of the spectral energy distribution (Armitage 2020):

$$\alpha_{IR} = \frac{d \log(\lambda F_{\lambda})}{d \log(\lambda)} \quad (1)$$

Where λ is the wavelength, F_{λ} is the observed flux, where the fraction represents the derivative of the SED so the slope can be calculated, which gives α_{IR} , the infrared spectral index. A redder protostar, which means it emits more in the longer wavelengths, has a positive α_{IR} value and corresponds to younger stars (Lada and Wilking 1984). For the Class 0 source α_{IR} is undefined because the spectral energy distribution is shifted to longer wavelength as the star is deeply buried in the envelope. Class I is defined to have values of $\alpha_{IR} > 0.3$, a flat spectrum source is defined to have values of $-0.3 < \alpha_{IR} < 0.3$, Class II is defined to have values of $-1.6 < \alpha_{IR} < -0.3$, and Class III is defined to have values of α_{IR} to be $\alpha_{IR} < -1.6$ (Armitage 2020).

Another way to distinguish between the different classes is using the bolometric temperature (T_{bol}). The bolometric temperature is the temperature a black body would have when emitting at the mean frequency of the observed continuum spectrum (Myers and Ladd 1993). H. Chen et al. 1995 constructed the bolometric-luminosity diagram based on 128 young stellar objects to compare the evolutionary stages. A Class 0 star has a $T_{bol} \leq 70K$ whereas a Class I protostar has a T_{bol} between 70-650K (Łukasz Tychoniec 2021). As these objects are both still fully embedded in the envelope and thus might look alike, measuring the bolometric temperature can be a good way to distinguish between both the classes. These infrared sources have a much broader spectrum than a black body, therefore the bolometric temperature is lower than the effective temperature (H. Chen et al. 1995). The class II protostars have a T_{bol} between 650-2800K whereas the class III protostars have $T_{bol} \geq 2800$ (Łukasz Tychoniec 2021). As the protostar evolves to become a main sequence star the bolometric temperature will approach the effective temperature, as the star is nearly a black body (H. Chen et al. 1995).

Finally, the classes can also be distinguished by their emitted light. Part of the light from the protostar will be scattered by the surrounding dust. The central star also heats up the surrounding disk and envelope of both gas and dust, which will then emit in different wavelengths

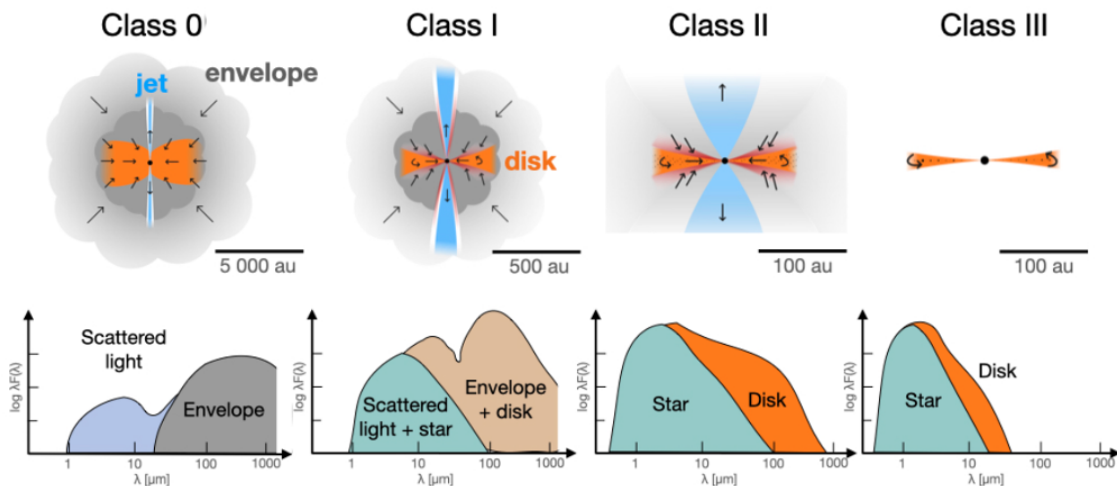


Figure 1: Schematic image of a protostar at different stages in the top, together with its expected Spectral energy distribution in the bottom (from Łukasz Tychoniec 2021; their Figure 1.1).

close to the infrared. The hot inner parts of the disk emit in the near infrared, whereas the cooler outer parts of the disk and the envelope emit at (sub)millimeter (sub-mm) wavelengths. Due to these differences in emission and physical structure, different classes of protostars have different SED shapes (Figure 1). Robitaille et al. 2006 analysed many different young stars using different models of all physical properties and found that different classes can be identified using their SED shape. Whitney et al. 2003 has modelled different evolutionary stages and their SED so they can be compared to observations and tells us that the emission in the longer wavelengths (sub-mm) of the Class 0 disk is caused by the emission of the opaque envelope. The starlight is only visible by the scattered light, as the star is fully embedded in the massive envelope. For Class I, the envelope is less massive, so the emission of the central star is more visible. Whitney et al. 2003 tells us that the emission in the longer wavelength emerges from the disk since the disk is growing in this stage. In Class II, the envelope almost dissipated away, leaving only the disk and star emission. Finally, in Class III the emission of the disk becomes negligible compared to that of the central star. So the shape of the SED can be used to determine the evolutionary stage. Some disks do not fit the SED classification, and are therefore called transition disks. They often show some sort of disk structure which alters the SED (Armitage 2020).

2.3 Planet formation

For planets to form, dust particles need to grow into pebbles by coagulation and condensation. Overdense pebble filaments undergo gravitational collapse which causes planetesimals to form. These planetesimals accrete more dust and smaller planetesimals to form protoplanets (Bitsch, Lambrechts, and Johansen 2015). This method forms terrestrial planets, but for gas giants there are two theories of planet formation: the widely accepted theory of core accretion and another theory called disk instability. Core accretion is a process where small planetesimals grow more massive during runaway growth. During this process a gaseous atmosphere is acquired, which will collapse when the isolation mass (of about $10 M_{\oplus}$) is reached, causing runaway gas accretion (Bitsch, Lambrechts, and Johansen 2015)(Boss 2000). Since this process takes a very long

time, the question arises whether it can form a gas giant during the lifetime of the disk. Disk instability requires a shorter time scale to create giant planets. In this process fragments of the disk become gravitationally unstable and immediately create self-gravitating clumps of gas and dust. These clumps will contract and form giant gas planets (Boss 2000).

The disk consists of gas and dust that is moving around the central star. The velocity of the gas is influenced by the pressure gradient ($\frac{dP}{dr}$). If the pressure gradient is negative, the gas will rotate at a sub-Keplerian speed, if the pressure gradient is zero the gas rotates at Keplerian speed and where the pressure gradient is positive, the gas rotates at super-Keplerian speeds. If we would assume the gas has a smooth monotonically decreasing pressure, all the gas would be rotating at sub-Keplerian speeds and solids would feel a gas drag and move towards the central star (Takeuchi and Lin 2002). However, the pressure is not monotonic and consists of local pressure maxima. As the radial velocity of the gas outside the pressure maxima points inwards, and inside the pressure maxima points outwards, the particles move towards the pressure maxima causing a pile up of solids (S. M. Andrews 2020).

Different structures of pressure maxima and minima with different origins occur in disks surrounding the protostars. These structures are well observable in protoplanetary disks of Class II and III protostars. They also occur in Class I and possibly Class 0 disks, but S. M. Andrews, Huang, et al. 2018 who observed 20 protoplanetary disks to find their substructure, explains that these protostars should be excluded to avoid confusion with the envelope emission. The different substructures can be categorized into four morphologies, ring/cavity structure, ring/gap structure, arcs and spirals (S. M. Andrews 2020). The ring/cavity structure has a narrow ring encircling the depleted cavity (S. M. Andrews, D. J. Wilner, et al. 2011). Transition disks often look like this, causing their unusual SEDs (Armitage 2020). In the rings/gaps structure rings (intensity enhancements) and gaps (intensity depletions) alternate (S. M. Andrews 2020). This substructure is most commonly identified in the mm continuum (Brogan et al. 2015) and has variations from the whole disk alternating with rings and gaps to only one gap between the core and the the outer ring (S. M. Andrews, Huang, et al. 2018). The difference between this last structure and the ring/cavity, is that the cavity has a completely empty cavity encircled by a ring, whereas the ring/gap structure still has a core inside the ring. Another morphology is the arcs, which is a non-axisymmetric feature the location of which ranges from being a partial ring surrounding a cavity to an additional substructure in a ring, cavity or gap (S. M. Andrews 2020) (Kraus et al. 2017). The final classified substructure is the spiral. These spirals range from open spirals with a two armed pattern to more complex or asymmetric structures that may be tightly wrapped. (Laura M Pérez et al. 2016) (Monnier et al. 2019).

These substructures themselves have different possible origins. Figure 2 shows a schematic illustration of the different structures and the different causes. Panel a of this figure shows how a cavity can be formed by magnetohydrodynamical (MHD) winds, these outflowing winds are induced by the magneto-centrifugal forces induced by electrically conducting fluids in a rotating disk. The cavity can also be cleared out by photo-evaporation flows that are flows of evaporated material induced by the radiation of the central star or another close source (Takahashi and Muto 2018)(Ercolano and Ilaria Pascucci 2017). The cavity could also be formed by giant planets that orbit inside the cavity and have overlapping gaps, clearing out the cavity (Zhu et al. 2011). Magnetohydrodynamical turbulence, which are chaotic motions in electrically conducting fluids, and circular shaped magnetic flux concentrations can create a rings and gaps structure, since the created zonal flow generates a banded density structure where the gas is repelled at the peaks and piles up at the dips (Johansen, Youdin, and Klahr 2009) (S. M. Andrews 2020). Smaller

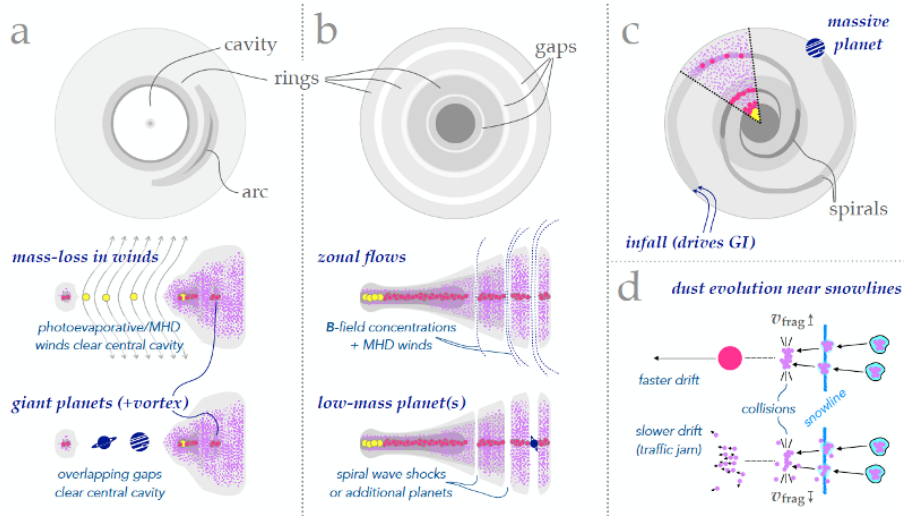


Figure 2: Schematic illustrations of the different substructures and their possible origin (from S. M. Andrews 2020; their Figure 10).

planets can also generate gaps and bright rings at the edge of the gap clearing its path (Rosotti et al. 2016). The different formation methods for the rings/gaps structure can be found in Figure 2 panel b. Gaps and rings can also occur at snow lines, there where a specific volatile sublimates. Snow lines can alter the fragmentation velocity v_{frag} , which is the threshold velocity for fragmentation to happen. If v_{frag} is higher, particles stick together more easily, while a lower v_{frag} , also called a traffic jam causes more fragmentation, which is displayed in Figure 2 (d) (Pinilla et al. 2017). These dust density alterations can cause substructures to occur (Marel, Williams, and Simon Bruderer 2018).

Spiral density waves (Figure 2 panel (c)) can be caused by magneto-rotational instability, which occurs when the rotational velocity of material in the disk decreases, in this case because of the presence of a planet, as the radius increases which makes the disk turbulent (Heinemann and Papaloizou 2009). These spiral structures can also be caused by gravitational instabilities which arise from asymmetric envelope accretion occurring in more massive protostars. (S. M. Andrews 2020). If the disk is essentially inviscid, which means turbulences are suppressed enough, low mass planets can make variations in particle distributions causing spiral arms. The more massive the planet the larger the pitch angles (Bae and Zhu 2018). More massive planets can also cause these spirals to occur interior to their large orbits (S. M. Andrews 2020).

To determine what the origin of these structures is, numerical models and simulations of physical processes are used to see what model matches the observation (S. M. Andrews 2020). Once a planetary system is fully formed, the gas and dust in the disk are gone.

2.4 Observational methods for star and planet formation

The universe emits in all wavelengths of the electromagnetic spectrum, which can be observed with different telescopes. As two important features in planet formation, line emission from gas and continuum emission from dust, are observable using long wavelengths, radio and sub-mm telescopes should be considered. With these types of telescopes we can observe gas and dust from the star and planet forming systems.

One of the two features that is observed in the process of planet formation is the line emission of the gaseous envelope, which is produced by discrete low energy transitions of atoms or molecules. This is used to see if the gas is rotating and thus forming a disk around the protostar, these observations are done at millimeter to sub-millimeter wavelengths. To image the rotating gas of a Class 0/ Class I protostar, integrated intensity (moment 0) and velocity (moment 1) maps are needed. Figure 3 shows some of the key molecular tracers.

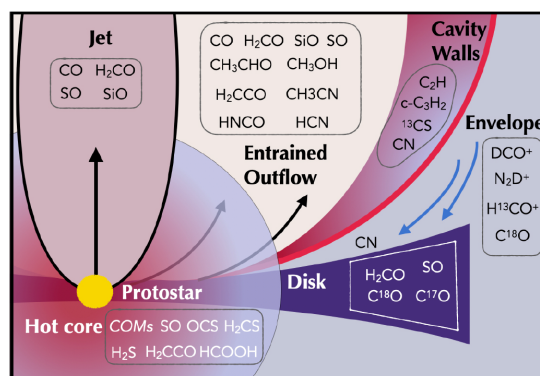


Figure 3: Which molecule traces a certain part of the protostar (from Łukasz Tychoniec, Dishoeck, et al. 2021; their Figure 11)

We are interested in the embedded disk, which according to Łukasz Tychoniec, Dishoeck, et al. 2021 is mainly traced by $C^{17}O$ and H_2CO . CN can be found in the upper layers of the embedded disk as it is the main tracer of the outflow cavity walls. H_2CO at high velocities can also be used to trace the molecular jets and at lower velocities to trace the outflows.

The other feature that is observed in the process of planet formation is the continuum emission of the heated dust in the disk, which emits almost like a black body. The substructures in the disk can be used to model possible planet formation, and the observed flux density is used to calculate the mass of the dust particles in the disk. This can be done using the following equation (Tobin, Sheehan, et al. 2020):

$$M = \frac{D^2 F_\nu}{\kappa_\nu B_\nu(T_{dust})} \quad (2)$$

where F_ν is the flux density, D is the distance to the star, κ_ν is the dust opacity, B_ν is the Planck function with a temperature of the dust (T_{dust}) which is about 30K for the embedded disks and 20K for Class II protostars. At these temperatures, the emission of the dust peaks at longer wavelengths as well. This formula is used to determine the mass of the disk around different protostars. κ_ν can range from 0.1 to 2 and can be a large factor of uncertainty in calculating the mass of the disks (Tobin, Sheehan, et al. 2020). If a high opacity is taken, the calculated disk mass is a lower bound.

Łukasz Tychoniec, Manara, et al. 2020 used observations of ALMA and VLA to set determine

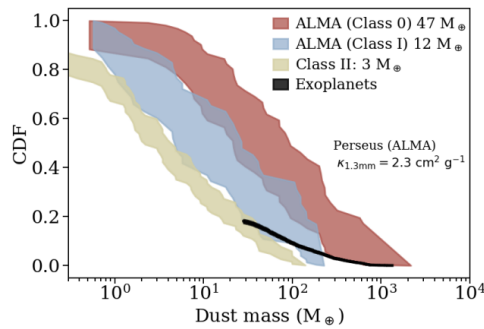


Figure 4: The cumulative distribution plots of the dust disk masses (from Łukasz Tychoniec, Manara, et al. 2020; their Figure 2 top panel)

the mass of the disks surrounding protostars of different classes, using equation 2. The disk mass was compared to the mass of observed exoplanetary systems to set constraints on the time-scale and efficiency of planet formation. Figure 4 shows some of the results. The Cumulative distribution plots of the dust disk masses, which means that at a CDF of 1, all disks in that class have a minimal mass of the according disk mass. The black line gives the cumulative mass of observed exoplanets. It can be seen that mass in Class II stars does not account for the mass found in exoplanetary systems. Whereas the disk mass of Class 0 and I is five to ten times higher than the disk mass of Class II stars, and thus can account for the mass of the observed exoplanets. These results claim that planet formation can already begin in the first 0.5 Myr.

To observe radio waves with a precision of about one arcsecond, a kilometer sized telescope would be needed, since the diffraction limit of a telescope is calculated by the observed wavelength divided by the diameter of the telescope. A telescope this size is impractical, so to make radio observations with a high precision, interferometry is needed, which uses multiple smaller telescopes, located on Earth, to work together to act as a larger aperture (D. Wilner 2005). An additional difficulty in observing sub-mm waves is the distortion of the signal by the water in the atmosphere. So when building the Atacama Large Millimeter/submillimeter Array (ALMA), the location was important, namely at the Chajnantor Plateau in the Atacama Desert of Chile at a height of 5000m. The atmosphere in the desert is very dry and together with the elevation the distortion is limited and since the desert is very dark as well, the signal is strong enough to get detected by ALMA (ALMA 2021).

3 Technical background

The data used in this thesis has been observed with ALMA. ALMA consists of 66 high precision antennas: Four antennas working as single dishes with a diameter of 12 meters, 12 antennas working together with a diameter of seven meters, and the remaining 50 antennas have a diameter of 12 meter and work together via interferometry (ALMA 2021), which uses the tiny delay in detecting the same signal between two antennas to measure the so-called coherence or the visibility function. The visibilities can later be converted using the Fourier transformation to obtain information on the sky brightness distribution. The rotation of the Earth causes the antennas to take different samples. The antennas can also be moved around on the surface of Earth to change the baseline between the two antennas which can be used to 'zoom'. Each unique set of baselines improves the completeness of the resulting image. The produced "dirty" images are corrupted by the structure of the point spread function, which is caused by the diffraction of light in the aperture and is based on the sampling structure. To get a better point spread function and thus a clearer image in the end, more antennas or samples are needed (D. Wilner 2005).

The ALMA default data calibration can be performed without any prior experience in interferometry as a calibration process with automated pipeline can be used by executing a script. The scriptForPI, which is provided with the raw data, calls the ALMA science pipeline which calibrates the visibilities and generates the calibrated Measurement Set containing the calibrated visibilities, the data weights and information about the point spread function. To create an image (referred to as cleaning) from the visibilities that the ALMA telescope produces the *tclean* command is used, which can generate data cubes and continuum maps from the calibrated measurement set. *tclean* runs iterations of major and minor cycles. The minor cycle operates only in the image plane and does the deconvolution, which removes the noise and resolves the signal. During the minor cycle the point spread function, the cleaning model itself and the gridded residual of the data with the model subtracted, are passed to the cleaning algorithm. The cleaning algorithm then searches for peaks in the residual image, subtracts the point spread function, and adjusts the model repeatedly. During this process the model is constructed with discrete components which can be based on delta functions or multi-scale, depending on the type of deconvolution algorithm used. The updated model will then be transferred to the visibilities plane where it is subtracted from the data during the major cycle to produce a new residual image. This new residual can then be used in the minor cycle again. These cycles are iterated until the stopping criteria are met. This stopping criterion is often based on having the residual maximum to be lower than a statistically relevant threshold (NRAO 2022).

The *deconvolver* parameter within *tclean* is used to choose the algorithm of the minor cycle. The default deconvolver is the 'hogbom' algorithm which constructs the model with components based on the delta functions by estimating the strength of the pixels. This was originally used to reconstruct point sources as it identifies the source pixel for pixel, but has been proven to work well for extended objects as well, though it might take longer and instabilities can occur for this reason. Another deconvolver algorithm that is used is the multi-scale algorithm, produced to improve stability, which first smooths the residual image and then constructs the model as if the object is composed of various different scale sizes by estimating the strength of these scale sizes (Cornwell 2008) (NRAO n.d.).

Another argument of the *tclean* command is the *weighting* argument, which has three options: natural, uniform and Briggs weighting. The natural weighting weighs the visibilities

according to the data weights, meaning it will enhance the contribution from shorter baselines (corresponding to lower resolution) and decreases the contribution from the longer baselines (corresponding to higher resolution). This will result in a lower RMS noise level but also a lower angular resolution. Uniform weighting weighs all baselines equally, meaning extra weight is given to longer baselines. This results in a higher angular resolution, but the RMS noise will also be higher. Uniform weighting also reduces the sidelobes, which are caused by the diffraction of light in the antennas. Finally, there is a compromise between natural and uniform weighting called Briggs weighting. Briggs weighting has a robust parameter that sets the relative importance of uniform (robust = -2) and natural (robust = 2) weighting. The default robust value is 0.5 when using Briggs weighting (Bemis 2021).

The *tclean* command also has the arguments *cell* and *imsize*, which can both be calculated. The cell size, in arcseconds, can be calculated using the following formula:

$$Cell = \frac{206265}{\text{'longest baseline in wavelength'} \cdot \text{'number of cells across the beam'}} \quad (3)$$

The image size can be calculated from the Half Power Beam Width (HPBW) of the Primary Beam which is calculated using:

$$HPBW = \frac{1.02\lambda}{D} \quad (4)$$

(multiplied by some factor of 1.5-2 (Bemis 2021)) where λ is the observed wavelength and D is the diameter of the antenna. Based on measurement,s Cortes et al. 2022 suggests using the following formula:

$$HPBW = \frac{1.13\lambda}{D} \quad (5)$$

The imaging process when making a continuum, will convert the signal of the telescope into intensities in Jy/beam. Another useful unit for the intensity is the brightness temperature (K), which can be calculated using the Rayleigh-Jeans law:

$$B_\nu(T_b) = \frac{2\nu^2 k_B T_b}{c^2} \quad (6)$$

where T_b is the brightness temperature, ν is the observed frequency, k_B is the Boltzmann constant, c is the speed of light and $B_\nu(T_b)$ is the spectral radiance with units $\text{W}\cdot\text{sr}^{-1}\cdot\text{m}^{-2}$. Finally, to use this formula a conversion from Jy/beam (the signal) to $\text{W}\cdot\text{sr}^{-1}\cdot\text{m}^{-2}$ (the spectral radiance) needs to be used:

$$Jy/beam = \frac{10^{-23} \cdot (\text{beam size in arcsec}^2)}{4.25 \cdot 10^{10}} B_\nu \quad (7)$$

Another argument of the *tclean* command is the *specmode* argument, which sets the spectral gridding type when cleaning the calibrated measurement set. This spectral mode should be set to *mfs* when producing a continuum image, as it will give only one output image channel, and should be set to *cube* to produce a data cube for spectral line imaging. A data cube is a 3D array of which two dimensions are spatial, producing an image, and the third dimension gives the spectral data based on wavelength or frequency. In short, the cube contains a full spectrum for every pixel in the image. A moment map can be produced out of a data cube, which means 'collapsing' one of these axis to gather a value from the combined moment axis into one pixel. This can be done in different ways to obtain different forms of moment maps. For explaining star and planet formation, moment 0 and moment 1 maps are useful. A moment 0 map gives the

integrated intensity of the spectral line. This essentially gives the amount of gas at each point. Moment 0 can be calculated using:

$$M_0 = \Delta v \sum I_i \quad (8)$$

Where Δv is the pixel width in direction of the moment axis and I_i is the intensity of the spectrum of the i th pixel. A moment 1 map is the intensity weighted coordinate, which gives the velocity field based on Doppler shifts. This essentially tells whether most of the gas at each point is moving towards or away from the observer. Moment 1 can be calculated using:

$$M_1 = \frac{\sum I_i v_i}{M_0} \quad (9)$$

where v_i is the coordinate of the i th pixel. (NRAO [2016](#))

4 Communication background and choices

4.1 Imaging using colors

Telescopes based in space and on the ground, covering the whole electromagnetic spectrum, release hundreds of astronomical images to the public every year (K. Arcand et al. 2010). These astronomical images are a powerful tool in communication as they are aesthetically pleasing, convey information (Smith et al. 2015) and are of great importance as they ‘sell’ astronomy (Christensen 2007). But it is important to think of the way the public perceive these images. Do they perceive the message of the image as intended by the astronomer? And what role does color play in perceiving an image?

K. Arcand et al. 2010 and Smith et al. 2015 looked at the aesthetics and understanding of astronomical images. They gave some guidelines and focus points when formatting images for the general public. For conveying the message of the image, the viewers as well as the experts, chose the red coloration (which is primarily red, medium green and high blue) as best fit. This color scheme was also the most pleasing for about two thirds of the viewers. Whereas orange or purple was the most appealing color for imaging (Smith et al. 2015). These are things to keep in mind when imaging for the general public as non-experts look at the aesthetic qualities of the image first (K. Arcand et al. 2010). The produced continuum images will thus have a specified color map that is focused on red and orange, and designed to show the structures and contrasts in the image the best. This color scheme should also be chosen so that colorblind people can still see the structures and contrasts. To meet these criteria I produced a color scheme myself using ‘*LinearSegmentedColormap*’ from the `matplotlib.colors` package with the colors black, red, orange-red, dark-orange, orange, gold and yellow.

It is important when choosing a color to explain why this color was chosen and especially what it represents. So the viewers do not feel misled by the colors that are picked by the scientist, they want to know that the colors have a certain purpose (K. K. Arcand et al. 2013). This explanation needs to be added in the text that accompanies the image. Viewers also indicated that a provided scale would help comprehending the image (K. Arcand et al. 2010). So I will be adding an ellipse and bar with the size of our solar system to most images to provide a bit of perspective, as our solar system is something familiar to the audience.

4.2 Medium of presenting images

At the moment, a planetarium is not yet a relevant way of communicating new findings. New data is constantly posted on websites of research institutions, blogs and the news, but this new content typically takes days or even weeks to be presented in the planetarium, if ever. Christensen et al. 2016 of ESO recognised this and concluded that there are several problems: it takes too much manual work to import and visualize the data, the pipeline and procedures to import and visualize the data are planetarium software dependent which makes the process inconvenient, it’s difficult for the operator to find the new content as it is widely distributed over the research institutions and finally, the operator would have a hard time learning the background story. The project Data2dome was created to make the flow between the content from the research institutions to the planetarium better, so that new data could be implemented in the dome, directly ready for outreach (Christensen et al. 2016).

To avoid these difficulties we thought of another way of using the planetarium for presenting new findings. We would like to start off with showing the night sky at the location of the telescope. Then an image of the first object will be enlarged from their exact location in the sky. Non-experts indicated that knowing the location of the object helps in comprehending the image (K. Arcand et al. 2010), which is a benefit of presenting the images in a planetarium. When the image is explained in the enlarged form, it will move to left the bottom of the dome. Then the second image or graph will be enlarged from its location on the sky, explained and also moves to the bottom of the dome, next to the first image. This will be continued with all the gathered images, representing the data gathered by the telescope. All images together at the bottom of the dome will then present some sort of timeline. This is a fairly easy way of implementing new findings, as you would only need the directory path of the image and the right location on the night sky. In this script, the image settings can also be altered to the users preferences. A detailed script based on the software used in DOT planetarium, which is called the SkySkan system (SkySkan 2022), can be found in the Appendix 10.4.

Since this way of implementing is rather quick, the operator does not need much time to create a show containing new data. This method therefore allows the operators to spend more time deciding exactly what and how to communicate as a thorough background research can be done, or the operator can spend more time making the data understandable for the public instead of spending time understanding the complex mechanisms of the planetarium. The operators could also format the ALMA data themselves following the instructions in Appendix 10.2, making it for example possible to update the show on planet formation.

It is also possible for the astronomer who gathered and formatted the data, and thus knows the background of the theory, to give a science talk with the help of communication guidelines. This would make the process of producing a show with new data even less time consuming. Additionally, direct contact between the public and the scientist can have a large impact, as they can ask questions face-to-face after the show, according to Christensen 2007.

4.3 The talk

Christensen 2007 explains that defining and knowing your target audience is of great importance. The narrower your target audience is, the better you can understand their needs and level of understanding. So the talk can be altered more specifically based on their knowledge but also pre-existing misconceptions about the scientific and technical details. These pre-existing misconceptions should be addressed to avoid further misunderstandings. Besides the misconceptions, the interest of the audience in science should be known so recent developments and concrete examples applicable to their daily life can be presented. These things can make science communication more successful.

When writing for the general public it is best to assume they know nothing and make the text as simple as possible. It's necessary, though, to find a balance between simplification and scientific correctness. The science should not be left out completely as showing the process and rewards of getting the solution helps appreciating the research, but keep it as simple as possible. For example, the equations should be minimized and only the most interesting parts should be selected to keep the attention of the audience. To keep the audience even more engaged, questions can be asked, for example: *'What do you think?'* (Christensen 2007).

I defined my target audience as students of other faculties, which means they all passed secondary school. Since Groningen has a large proportion of international students (26% of the students and 52% of the PhD candidates (Groningen 2020, 2021)) and the English level of the average Dutch student is high (assuming all students have either finished HAVO, achieving CERF level of B1 (97.1%) or B2 or higher (79.1%), in English, or finished VWO, achieving a level of B2 or higher (93.3%) (Fasoglio and Tuin 2018)), the talk may be given in English. This is in agreement with the fact that English shows at DOT Live Planetarium are better attended than Dutch shows (Hoek 2022, Private Communication) But the knowledge of physics and its terminology varies greatly between individuals. Among the Dutch students, some will know most terms in physics, if they have taken physics exams within the past few years, while others know very little if they only had physics lessons up to the age of 14 or 15. This means that introducing the subject, concepts and terminology is of great importance, as well as the usage of easy language, otherwise the story will not be conveyed.

Besides an extensive introduction on the subject and the concepts used, other issues need to be addressed during the talk. The viewers surveyed in Smith et al. 2015 gave some suggestions for what they would like to hear to improve the comprehension of images. First, they would like to have some historical background of the object together with a sense of scaling and the location of the object, which is partly taken into account when producing the image and implementing it in the planetarium. Most images are already accessible for the general public, but to understand the images, people find it interesting to know how the data was gathered and how the images were produced (Hiramatsu and Amano 2021). To accomplish this, the telescope that gathered the data should first be shown and introduced. When showing the images produced, parts of the imaging process should be explained as well. For example, what the colors represent and if this is what we would see with the naked eye. The viewers also want to know if the images shown are used for research or only produced to show to the public and they are curious how astronomers perceive these images (Smith et al. 2015). During the talk, uncertainties in theories and imaging can be shared with the public. At the end of the show, it is then useful to give a future perspective as well and what type of revolutionary new telescope could remove some of the uncertainties.

Another way to increase the chance of getting your story being conveyed well is using storytelling techniques. When people listen to facts only two parts of the brain are activated, but when they listen to a narrative story, seven parts of the brain are activated (Schwertly 2022). That is because parts of the brain that aren't part of the traditional "language network" are activated. These are parts of the brain that are coupled to our senses, as we experience what happens in the story by evoking mental images, causing a chemical, physical and emotional response (Martinez-Conde et al. 2019). The audience will then participate in the story since there are recognizable parts. As a result of this response, storytelling can increase information retention by 26%, compared to stating facts (Schwertly 2022). This can be a very useful technique when communicating science to the public, as viewers also indicated that they would like to have some context given, preferably in a narrative text style (Smith et al. 2015).

There are many different methods of (scientific) story telling, there are different templates, structures and approaches. Wibisono 2022 explains that most stories have characters, like a hero, a nemesis and a sage. In scientific stories this can be the researcher themselves, someone who has inspired the researcher, or perhaps the object you want to show or explain. Next a setting should be explained, give the background to the study. Then there should be some tension or conflict that your hero is trying to overcome, think of the setbacks during the study. The story

then needs some action, what did the hero do to overcome these setbacks. Then the story needs a climax, what is the final solution to solve your main challenge and a resolution, what does it mean for the rest of the world or your field that this problem is solved. This can be done in different formats. For example a classic Fairytale story line can be used, starting with *Once upon a time...*. Other storytelling structures that are useful can talk about the past, *'What did we learn?'* or the future, *'What can we do?'* (Schwertly 2022).

I used another simple template: *'Because I saw/knew that ...'* sketches the scene and explains inspiration, *'I wondered ...'* states the research question, *'I suspected that if (this happened) then (I would observe this)'* is used to state your hypothesis, *'So I (did this) and (this happened)'* gives the method, approach and results. *'Which finally told me that ...'* concludes your story and can give future perspectives.

When telling a story it is useful to follow the three-act structure, that is essentially explained as: "Say what you are going to say; say it; then say what you said." Wibisono 2022 explains this exact structure might be a bit boring for storytelling purposes, but it is advised to use the three-act structure where you state the problem or issue, then the action and finally the result or benefit. This structure with a beginning, middle and end is used by novels, movies and other media as well and makes the content more memorable (Stahl and Davis 2009). Using a three-act structure still leaves many different story shapes. For example the 'mountain', where the drama piles up after the start until the top of the mountain is reached, and ends at a different place than the start. Or the 'sparkline', where the beginning paints the world as it is now, the middle presents comparisons to what could be and what is, and the ends with a call for action.

When writing a story, think also about what the inspiration was for the research or theory you want to present and try to understand your audience so you can tell a story they want to take part in so they get invested. It is also important to use sensory details and descriptions so it's easier to be part of the story and try to connect new concepts to things that are familiar to the audience (Schwertly 2022) (Wibisono 2022).

5 Selected objects

Now that the theory on planet and star formation is clear, it's necessary to think of the stages that need to be explained, and especially shown, to the general public for a complete story. It's important to note that not all steps need to be explained in detail, and some steps are easier to visualize than others. In this section, a selection of objects that can be imaged to explain some main stages in the theory of planet formation are laid out .

The first stage that should be shown is a molecular cloud. This is the location where many new stars, and thus planets, are formed so it's an important stage to start with. We start off with an image of the Orion nebula (M42) made by Hubble, shown in Figure 5. This is a huge cloud 500pc from the sun that provides a large sampling of all stages, containing at least 428 Class 0 / Class I sources and 2990 class II / Class III sources(Tobin, Sheehan, et al. 2020). Tobin, Sheehan, et al. 2020 used sources from these clouds to find the average mass of protostars in each class. The location of the Orion nebula:

M42: 05h 35m, -05° 23' J2000 (SIMBAD 2022).

The image of the Orion nebula is also widely known, so most of the audience will be able to relate to this object as it is a familiar image.



Figure 5: Hubble image of Orion nebula.(from: NASA 2006) Credits: NASA n.d., ESO n.d., M. Robberto (Space-Telescope-Science-Institute n.d./ESO n.d.) and the Hubble Space Telescope Orion Treasury Project Team

After the molecular cloud is shown, Class 0 and Class I should be shown. This stage is characterized by a rotating gaseous envelope surrounding the protostar and a disk that is formed as a consequence of the conservation of angular momentum. To show this, moment 1 maps are needed that will demonstrate the movement of the gaseous envelope. The Taurus molecular cloud is one of the closest star forming regions, located at 140 pc from our sun. Van't Hoff et al. 2020 have observed 5 sources in the Taurus molecular cloud and show moment maps that indicate the kinematics of these objects. Aso et al. 2015 and Yen et al. 2014 both show extensive analyses using ALMA observations of two of these objects: TMC1A and L1489 IRS. The Taurus cloud is located at 140 pc (Yen et al. 2014) from our sun. The exact locations of the objects are:
 L1489 IRS: 04h 04m 43.1s, +26° 18' 56.2" J2000 (*Catalog of Circumstellar Disks* 2022).
 TMC1A: 04h 39m 35.2s, +25° 41' 44.2" J2000 (*Catalog of Circumstellar Disks* 2022).
 The systematic velocity of L1489 IRS is 7.2 km/s (Yen et al. 2014) and the systematic velocity of TMC1A is measured to be 6.4 km/s (Aso et al. 2015). L1489 IRS and TMC1A are both classified as Class I protostars with a bolometric temperature of 226K and 164 K respectively. A

disk and Keplerian motion have been established at both sources (Van't Hoff et al. 2020). Aso et al. 2015 and Yen et al. 2014 also present moment 1 maps that show the rotational motion. So I will be making moment maps of these two objects to show the audience the second phase of star and thus planet formation. Relevant properties of the objects selected for the moment maps are shown in Table 1

Source name	L1489 IRS	TMC-1A
Class	I	I
Right Ascension (J2000)	04h 39m 35.2s	04h 04m 43.1s
declination (J2000)	+25° 41' 44.2"	+26° 18' 56.2"
Velocity	7.2 km/s	6.4 km/s
Distance	140 pc	140 pc
Disk radius	600 AU	100 AU
T_{bol}	226 K	164 K
Reference	1 & 2	1 & 3

Table 1: Overview of the properties of selected objects for the moment maps. References (1) (Van't Hoff et al. 2020), (2) (Yen et al. 2014), (3) (Aso et al. 2015)

Next we need to show the Class II and Class III protostars and disks. The main feature to show the audience in this phase are the substructures in the disk. S. M. Andrews, Huang, et al. 2018 show high resolution images of some disks in the Rho Ophiuchi cloud complex, but because the show is about planet formation we need to make sure the gaps are likely to be formed by planets. Fedele et al. 2018 and Dipierro et al. 2018 predict, with ALMA observations and the help of simulations, that the gaps of the disks around AS209 and Elias24 are formed by planets. This makes these sources especially interesting to look at and ideal objects for a planetarium show about planet formation. Both stars are classified as K5 stars and as Class II sources based on their SED (S. M. Andrews, Huang, et al. 2018). AS209 is located at the northern part of Rho Ophiuchi 3a, at 121pc from the sun (S. M. Andrews, Huang, et al. 2018) whereas Elias24 is located at the main cloud L1688 which is located 136 pc from the sun (S. M. Andrews, Huang, et al. 2018). The exact location of the objects are:

AS209: 16h 49m 15.31s, -14° 22' 08.6" J2000 (*Catalog of Circumstellar Disks 2022*).

Elias24: 16h 26m 24.09s, -24° 16' 13.3" J2000 (*Catalog of Circumstellar Disks 2022*).

The disk of AS209 has a diameter of 278 AU and the disk of Elias24 has a diameter of 272 AU. The observations of AS209 done in project ID 2015.1.00486.S have an angular resolution of 0.172 arcsecond, which corresponds to a spatial resolution of 20.1 AU at the distance of AS209. Later observations of AS209 in project ID 2016.1.00484.L have an angular resolution of 0.033 arcsecond, which corresponds to a spatial resolution of 4.0 AU at the distance of AS209. The higher resolution of project ID 2016.1.00484.L allows for the structures to be imaged more precisely. The observations of Elias24 have an angular resolution of 0.022 arcsecond, which corresponds to 3.0 AU at the distance of Elias24 (*ALMA Science Archive 2022*). The high angular resolution data of these two objects from project ID 2016.1.00484.L are used to produce continuum images to show the next stage of planet formation to the audience. Relevant properties of the objects selected for the continuum images are shown in Table 2.

To make the story complete, a planetary system needs to be shown. The planets in system HR8799 can actually be shown since they have been imaged directly (Figure 6) reflecting the

Source name	Elias24	AS209
Class	II	II
Right Ascension (J2000)	16h 26m 24.09s	16h 49m 15.31s
declination (J2000)	-24° 16' 13.3"	-14° 22' 8.6"
Spectral type	K5	K5
Distance (pc)	136	121
Disk radius (AU)	136	139
$\log(T_{eff})$ (K)	3.63	3.63
Reference	4 & 5	4 & 5

Table 2: Overview of the properties of selected objects for the continuum images. References (4) (*Catalog of Circumstellar Disks 2022*), (5) (S. M. Andrews, Huang, et al. 2018)

light of their central star. Showing an image of this planetary system will be a step to something the audience might already know: the reflection of light, just as we can see the reflection of Jupiter or Mars some nights. HR8799 has 4 directly imaged planets which are all classified as super Jupiters. It also contains a debris belt outside the planetary orbits, with a disk size of 1136 AU (Marois, Zuckerman, et al. 2010). This debris belt can still be observed in the continuum, which does not have a high resolution but would be a nice extra feature to make the bridge to show there is very little dust left when the planets are formed. HR8799 is classified as a A5 star and is located at about 40 pc away from the sun (Marois, Macintosh, et al. 2008). The exact location of the object is:

HR8799: 23h 07m 28.71s, +21° 08' 03.3" J2000 (*Catalog of Circumstellar Disks 2022*).

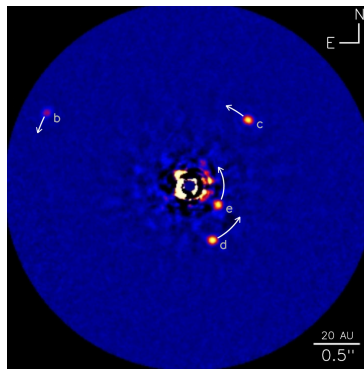


Figure 6: Image of HR8799 by Keck Observatory. (from Observatory 2018) Credits: NRC-HIA/C. MAROIS/W. M. KECK OBSERVATORY.

Ideally, more objects should be selected in order to clarify the story about how astronomers verify their theories on star and planet formation using observations. Objects from different locations should also be used, where this thesis was limited by time and therefore only used two locations.

6 Method

The ALMA archive (*ALMA Science Archive* 2022) was used to collect the data needed from different objects. To analyse the data and make images, the Common Astronomy Software Applications (CASA) was used (NRAO *Release 6.5*).

For L1489 IRS and TMC1A the cubes from project ID 2017.1.01413.S were used. For L1489 IRS the cubes of spectral windows 27 and 29 show activity that can be used for imaging and for TMC1A the cubes with spectral windows 29 and 30 are used. Spectral window 27 traces the line emission of CN with the rest frequency of 226.87478 GHz, spectral window 29 traces the line emission of H₂CO the transition 3_{1,2} – 2_{1,1} with rest frequency 225.697775 GHz and finally spectral window 33 traces the line emission of C¹⁷O the transition 2-1 with a rest frequency of 224.714385 GHz (Van't Hoff et al. 2020). For these observations 47 antennas were used with baselines between 15m and 1.4 km (Van't Hoff et al. 2020).

For AS209, first the data from project ID 2015.1.00486.S was used, in which AS209 is observed in 2016, in band 6 (211–275 GHz), once with 22 and once with 41 antennas. For the continuum the spectral window was centred at 230 GHz (Fedele et al. 2018). To calibrate this data set the raw and auxiliary data was downloaded and reduced with the CASA pipeline version 4.7.0.

To get images of AS209 with a higher resolution the raw and auxiliary data was downloaded from project ID 2016.1.00484.L. These observations were also taken in band 6, and the continuum was sampled in three spectral window's that were centred at 232.6, 245.0, and 246.9 GHz (S. M. Andrews, Huang, et al. 2018). The data reduction was done with CASA version 4.7.2. The same project and CASA version was used to image Elias 24.

All images were made using *immoments* and *tclean* in the newest CASA version 6.2.1.

Once all images are produced, different measurements, from both the moment maps and the continuum images, are taken using CARTA. For the continuum image, the header is used to find the beam size and the central frequency, and the statistics tool is used to make measurements for the peak intensity and the rms noise level. The data gathered from CARTA is also used to produce a brightness profile to analyzed the continuum of of AS209. The brightness profile plots the observed brightness temperature (in Kelvin), converted using the formulas 6 and 7 of Section 3, vs the radial displacement of the disk.

Another measurement that can be done for the produced continuum images and moment maps, is the inclination angle and position angle of the disk, to get these values an ellipse is fitted to the emission. To calculate the inclination angle I assumed the disk is circular and used:

$$\cos(i) = \frac{minor}{major}$$

where i is the inclination angle, *minor* is the minor axis of the fitted ellipse and *major* is the major axis of the fitted ellipse. The errors on the inclination angle and emission area corresponding to the fitted ellipse are calculated assuming a measurement error of two pixels for both the major and minor axis.

For the continuum images, a disk can be fitted just by looking at the edge of the disk. For the moment maps I fitted an ellipse in three different ways focusing on different parts of the

emission since the emission of the moment map is not perfectly symmetric, I fitted an ellipse in three different ways, focusing on different parts of the emission. The first time I only looked at the centre of the emission, the brightest parts of the moment 1 map. For the second ellipse, I plotted the contours of the moment 0 map, that show 50% of the flux and fitted an ellipse closely related to these contours. For the final ellipse I plotted the contours of the moment 0 map that correspond to 5σ ($\sigma = 7\text{mJy/beam}$) and fitted an ellipse closely related to the contours. I performed these measurements and calculations for all spectral windows for both Class I sources, the results can be found in Tables 3, 4, 5, 6 and 7.

The fitted ellipse is also used to determine the integrated flux density of the disk for both the continuum and the moment maps and is used to calculate the area of emission for the moment maps.

7 Results

In this chapter, I discuss the different results; section 7.1 shows the different Moment map imaging parameters I explored and some properties of these images, section 7.2 the continuum imaging parameters and the properties of these images and section 7.3 shows the guidelines for a script for a show on planet formation.

7.1 Moment maps

In this section, combined moment 0 (white contours) and moment 1 (color scale) maps are shown of L1489 IRS and TMC 1A. Different chemical species are mapped in different figures. The different subfigures shown have different intensity inclusion levels which are set with *includepix*, in which the pixels of a specified intensity and higher are included. The lower the first value of this argument, the lower the threshold intensity and thus the more pixels are included, whereas the higher the value the fewer pixels are included. This is used to avoid mapping the background noise, and it is recommended to have the lower boundary at about three times the RMS noise level. Since this value fluctuates between five and 10 mJy/beam, for all cubes, a minimum of 20 mJy/beam was chosen to begin with. To see the effects of these settings, the images must be viewed and based on the amount of noise remaining new boundaries for '*includepix*' can be set to finalize the moment 1 map.

This section also lists the properties position angle, inclination angle, area of emission and flux density of three different methods discussed in Section 6 of the moment maps produced.

L1489 IRS moment maps

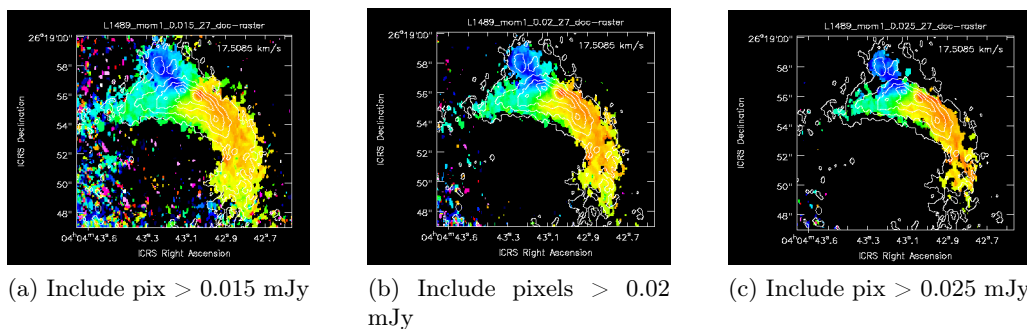


Figure 7: Moment 0 (white contours) and moment 1 (color scale) maps of CN towards L1489 IRS. Contours at (0.015, 0.0524, 0.0898, 0.1272, 0.1646) Jy/beam. Color scale runs from 10.6 km/s (blue) to 15.2 km/s (red). Beam size 0.5447" x 0.3825". Left (panel a) moment 1 maps includes pixels with fluxes above 15 mJy, middle (panel b) includes pixels with fluxes above 20mJy/beam, right (panel c) includes pixels with fluxes above 25mJy/beam.

Figure 7 shows combined moment 0 and moment 1 maps of CN towards L1489 IRS. To produce these maps the channels 803 to 914 were used. The three subfigures are created with different noise levels included, with *includepix* = [0.015,100], *includepix* = [0.02,100] and *includepix* = [0.025,100]. The CN molecule can be found in the upper layers of the disk and in the cavity walls (see Figure 3). Figure 7 panel (a) shows too much noise as there are randomly colored dots appearing, further from the main gas emission. Figure 7 panel (b) shows a bit too much noise as there are still some random colored dots in the bottom left corner. Figure 7 panel (c) shows

minimal noise, but the emission is cut, as some black patches occur in the uniformly colored emission.

Method	PA ($^{\circ}$)	Inclination ($^{\circ}$)	Area (arcsec 2)	Flux (Jy)
(1)	(2)	(3)	(4)	(5)
Central	62^{+3}_{-7}	$66.6^{+8.5}_{-11.5}$	$1.74^{+0.74}_{-0.63}$	1.1
50%	60^{+12}_{-10}	$62.3^{+4.6}_{-5.3}$	$9.40^{+1.60}_{-1.50}$	4.0
5σ	54^{+11}_{-10}	$63.1^{+4.5}_{-3.4}$	$20.2^{+2.31}_{-2.23}$	6.0

Table 3: Properties of fitted ellipses of L1489 IRS spectral window 27, corresponding to the emission of CN with $includepix = 20mJy$, corresponding to Figure 7 panel (b). The rows show the three different methods used to fit an ellipse. Column 1: The part of the emission the ellipse is fitted to. Column 2: The position angle of the fitted ellipse. Column 3: The inclination angle of the fitted ellipse assuming a circular disk. Column 4: The emitting area corresponding to the area of the fitted ellipse. Column 5: The flux density of the moment 0 map inside the fitted ellipse.

Table 3 shows the measured disk properties for CN towards L1489 IRS based on Figure 7 panel (b). The fitted ellipse has an inclination angle between 62° and 67° , a position angle between 54° - 62° , and enclosed fluxes of 1.1 Jy within the central emission, corresponding to 1.74 arcsec 2 , 4.0 Jy within the 50% contour (9.4 arcsec 2), and 6.0 Jy within the 5σ contour (20.2 arcsec 2)

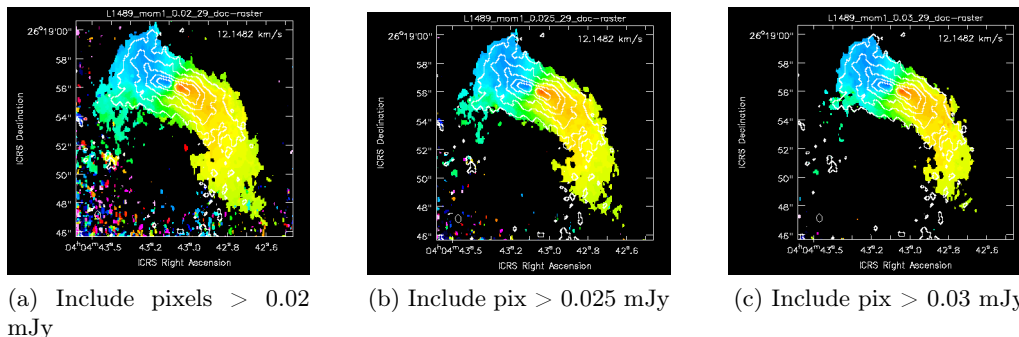


Figure 8: Moment 0 (white contours) and moment 1 (color scale) maps of H_2CO towards L1489 IRS. Contours at (0.025, 0.073, 0.121, 0.169, 0.217) Jy/beam. Color scale runs from 5.4 km/s (blue) to 9.5 km/s (red). Beam size $0.5532'' \times 0.3874''$. Left (panel a) moment 1 maps includes pixels with fluxes above 20 mJy, middle (panel b) includes pixels with fluxes above 25mJy/beam, right (panel c) includes pixels with fluxes above 30mJy/beam.

Figure 8 shows combined moment 0 and moment 1 maps of H_2CO towards L1489 IRS. To produce these maps the channels 390 to 508 were used. The three subfigures are created with different noise levels included, with $includepix = [0.02,100]$, $includepix = [0.025,100]$ and $includepix = [0.03,100]$. The H_2CO molecule traces the embedded disk and can also be found in the outflows and molecular jets (see Figure 3). Figure 8 panel (a) shows too much noise as there are randomly colored dots appearing, further from the main gas emission. Figure 8 panel (b) shows a bit too much noise as there are still some random colored dots in the bottom left corner. Figure 8 panel (c) shows minimal noise and uniform colored emission.

Method	PA ($^{\circ}$)	Inclination ($^{\circ}$)	Area (arcsec 2)	Flux (Jy)
(1)	(2)	(3)	(4)	(5)
Central	68 $^{+6}_{-4}$	73.7 $^{+5.5}_{-6.6}$	2.52 $^{+0.95}_{-0.85}$	2.1
50%	69 $^{+6}_{-10}$	62.3 $^{+6}_{-3.5}$	9.10 $^{+1.59}_{-1.47}$	5.6
5 σ	60 $^{+11}_{-8}$	64.7 $^{+2.9}_{-3.1}$	21.2 $^{+2.38}_{-2.32}$	8.9

Table 4: Properties of fitted ellipses of L1489 IRS spectral window 29, corresponding to the emission of H₂CO with *includepix* = 30mJy, corresponding to Figure 8 panel (c). Columns as in Table 3.

Table 4 shows the measured disk properties for H₂CO towards L1489 IRS based on Figure 8 panel (c). The fitted ellipse has an inclination angle between 62 $^{\circ}$ and 74 $^{\circ}$, a position angle between 60 $^{\circ}$ -69 $^{\circ}$, and enclosed fluxes of 2.1 Jy within the central emission, corresponding to 2.52 arcsec 2 , 5.6 Jy within the 50% contour (9.10 arcsec 2), and 8.9 Jy within the 5 σ contour (21.2 arcsec 2).

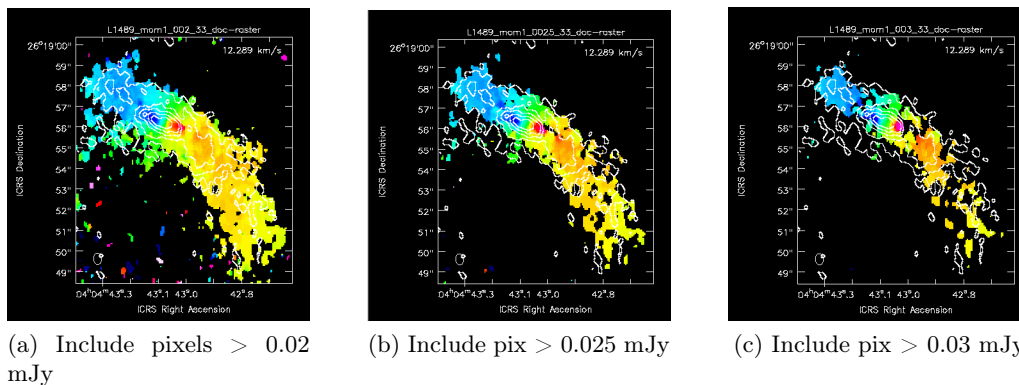


Figure 9: Moment 0 (white contours) and moment 1 (color scale) maps of C¹⁷O towards L1489 IRS. Contours at (0.023, 0.0494, 0.0758, 0.1022, 0.1286) Jy/beam. Color scale runs from 5.0 km/s (blue) to 10.8 km/s (red). Beam size 0.5562'' x 0.3877''. Left (panel a) moment 1 maps includes pixels with fluxes above 20 mJy, middle (panel b) includes pixels with fluxes above 25mJy/beam, right (panel c) includes pixels with fluxes above 30mJy/beam.

Figure 9 shows combined moment 0 and moment 1 maps of C¹⁷O towards L1489 IRS. To produce these maps the channels 387 to 505 were used. The three subfigures are created with different noise levels included, with *includepix* = [0.02,100], *includepix* = [0.025,100] and *includepix* = [0.03,100]. The C¹⁷O molecule is an isotope of CO and is used to trace the embedded disk. Figure 9 panel (a) shows too much noise as there are some randomly colored dots appearing, further from the main gas emission. Figure 9 panel (b) shows minimal noise but a bit too much emission is cut as black patches are appearing in the uniformly colored emission. Figure 9 panel (c) has excluded too much emission, indicated by all black patches between the uniformly colored emission patches.

Method	PA ($^{\circ}$)	Inclination ($^{\circ}$)	Area (arcsec 2)	Flux (Jy)
(1)	(2)	(3)	(4)	(5)
Central	67^{+4}_{-5}	$64.3^{+9.2}_{-12.9}$	$1.75^{+0.73}_{-0.62}$	0.78
50%	66^{+7}_{-10}	$55.2^{+13.1}_{-13}$	$3.29^{+0.94}_{-0.82}$	1.2
5σ	55^{+6}_{-5}	$70.1^{+3}_{-3.3}$	$12.5^{+1.90}_{-1.89}$	6.7

Table 5: Properties of fitted ellipses of L1489 IRS spectral window 33, corresponding to the emission of $C^{17}O$ with $includepix = 20mJy$, corresponding to Figure 9 panel (a). Columns as in Table 3.

Table 5 shows the measured disk properties for $C^{17}O$ towards L1489 IRS based on Figure 9 panel (a). The fitted ellipse has an inclination angle between 55° and 71° , a position angle between 55° - 67° , and enclosed fluxes of 0.78 Jy within the central emission, corresponding to 1.75 arcsec 2 , 1.2 Jy within the 50% contour (3.29 arcsec 2), and 6.7 Jy within the 5 sigma contour (12.5 arcsec 2).

Other quantities that are obtained from the images are the central velocity which is 13.0 km/s based on the emission of CN, 7.4 km/s based on the emission of H_2CO and 7.5 km/s based on the emission of $C^{17}O$, and the integrated flux within a circular aperture with $6.0''$ diameter that resulted in 6.19 Jy km/s for the emission of CN, 8.72 Jy km/s for the emission of H_2CO and 3.43 Jy km/s for the emission of $C^{17}O$.

TMC1A moment maps

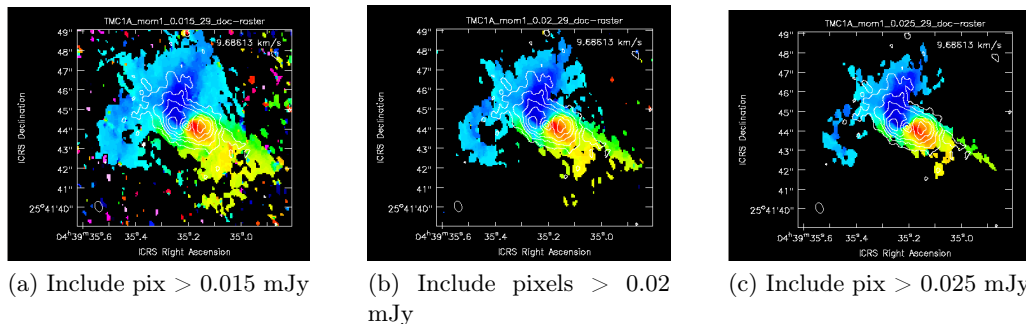


Figure 10: Moment 0 (white contours) and moment 1 (color scale) maps of H_2CO towards TMC1A. Contours at (0.022, 0.042, 0.062, 0.082, 0.102) Jy/beam. Color scale runs from 5.1 km/s (blue) to 8.2 km/s (red). Beam size $0.5647'' \times 0.3701''$. Left (panel a) moment 1 maps includes pixels with fluxes above 15 mJy, middle (panel b) includes pixels with fluxes above 20mJy/beam, right (panel c) includes pixels with fluxes above 25mJy/beam.

Figure 10 shows combined moment 0 and moment 1 maps of H_2CO towards TMC1A. To produce these maps the channels 430 to 504 were used. The three subfigures are created with different noise levels included, with $includepix = [0.015,100]$, $includepix = [0.02,100]$ and $includepix = [0.025,100]$. Figure 10 panel (a) shows too much noise as there are randomly colored dots appearing further from the main gas emission. Figure 10 panel (b) shows only a few colored dots, so there is still too much noise included. Figure 10 panel (c) shows no noise but has excluded

too much emission, as a black patch has appeared in the centre of the uniformly colored emission.

Method	PA °	Inclination °	Area arcsec ²	Flux Jy
(1)	(2)	(3)	(4)	(5)
Central	75^{+8}_{-5}	$55.9^{+10.1}_{-14.9}$	$2.53^{+0.83}_{-0.72}$	0.93
50%	65^{+9}_{-7}	$47.3^{+9.6}_{-13.8}$	$5.13^{+1.13}_{-1.03}$	1.6
5σ	58^{+5}_{-14}	$53.5^{+6.9}_{-8.6}$	$7.30^{+1.36}_{-1.25}$	1.9

Table 6: Properties of fitted ellipses of TMC1A spectral window 29, corresponding to the emission of H₂CO with *includepix* = 20mJy, corresponding to Figure 10 panel (b). Columns as in Table 3.

Table 6 shows the measured disk properties for H₂CO towards TMC1A based on Figure 10 panel (b). The fitted ellipse has an inclination angle between 47° and 56°, a position angle between 58°-75°, and enclosed fluxes of 0.93 Jy within the central emission, corresponding to 2.53 arcsec², 1.6 Jy within the 50% contour (5.13 arcsec²), and 1.9 Jy within the 5 σ contour (7.30 arcsec²).

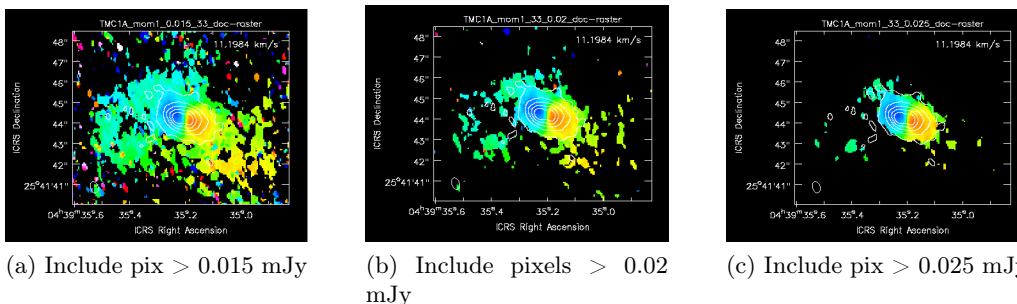


Figure 11: Moment 0 (white contours) and moment 1 (color scale) maps of H₂CO towards TMC1A. Contours at (0.035, 0.121, 0.207, 0.293, 0.379) Jy/beam. Color scale runs from 4.3 km/s (blue) to 8.5 km/s (red). Beam size 0.5625'' x 0.3695''. Left (panel a) moment 1 maps includes pixels with fluxes above 15 mJy, middle (panel b) includes pixels with fluxes above 20mJy/beam, right (panel c) includes pixels with fluxes above 25mJy/beam.

Figure 11 shows combined moment 0 and moment 1 maps of C¹⁷O towards TMC1A. To produce these maps the channels 410 to 528 were used. The three subfigures are created with different noise levels included, with *includepix* = [0.015,100], *includepix* = [0.02,100] and *includepix* = [0.025,100]. The C¹⁷O molecule is an isotope of CO and is used to trace the embedded disk. Figure 11 panel (a) shows a significant amount of noise as there are randomly colored dots appearing around the main emission. Figure 11 panel (b) shows only a few colored dots, so still too much noise is included. Figure 11 panel (c) shows minimal noise.

Method	PA °	Inclination °	Area arcsec ²	Flux Jy
(1)	(2)	(3)	(4)	(5)
Central	75^{+12}_{-8}	$45.6^{+7}_{-45.6}$	$1.42^{+0.62}_{-0.51}$	2.0
50%	70^{+7}_{-7}	$49.0^{+12}_{-19.9}$	$2.66^{+0.83}_{-0.73}$	2.9
5 σ	60^{+15}_{-11}	$47.1^{+9.5}_{-14}$	$5.25^{+1.1}_{-1.0}$	3.6

Table 7: Properties of fitted ellipses of TMC1A spectral window 33, corresponding to the emission of C¹⁷O with *includepix* = 25mJy, corresponding to Figure 11 panel (c). Columns as in Table 3.

Table 6 shows the measured disk properties for C¹⁷O towards TMC1A based on Figure 11 panel (c). The fitted ellipse has an inclination angle between 45° and 49°, a position angle between 60°-75°, and enclosed fluxes of 2.0 Jy within the central emission, corresponding to 1.42 arcsec², 2.9 Jy within the 50% contour (2.66 arcsec²), and 3.6 Jy within the 5 σ contour (5.25 arcsec²).

Other quantities that are obtained from the images are the central velocity which is 6.6 km/s based on the emission of H₂CO and 6.4 km/s based on the emission of C¹⁷O, and the integrated flux within a circular aperture with 6.0" diameter that resulted in 2.8 Jy km/s for the emission of H₂CO and 5.1 Jy km/s for the emission of C¹⁷O.

7.2 Continuum

In this section, the resulting continuum images created with different parameter settings are shown. When producing the continuum images, different settings in the CASA imaging task *tclean* were used to see what the consequences are for imaging purposes, especially to determine the settings that work best for presenting to the general public. A selection of the results are given here and the rest of the images can be found in Appendix 10.1.

This section also lists the properties central frequency, beam size, integrated flux inside the disk, peak intensity, rms noise and signal-to-noise ratio of these images. An ellipse was fitted to the continuum images as well, the boundaries of which are less uncertain than for the moment maps since the disk is mapped clearly. These ellipses were used to find the integrated flux of the disk and the inclination and position angle. This resulted in an inclination angle of 33.6°⁺¹_{-1.2} for AS209 and 31.6°^{+1.1}_{-1.2} for Elias 24. And the position angle for AS209 is 85° ± 4° and for Elias 24, PA = 43° ± 12°.

Channel selection

The first thing that was tested, was the inclusion or exclusion of lines as well as the inclusion or exclusion of multiple spectral windows.

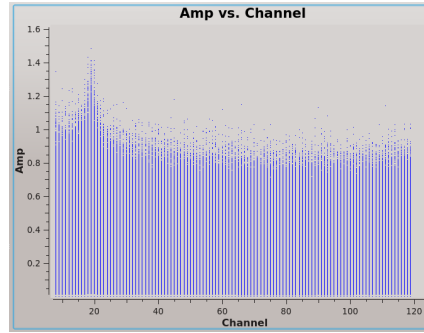


Figure 12: Signal amplitude in each channel of AS209 indicated by blue points, shown in *plotms*. This CASA function allows the user to identify any channels which contain spectral lines.

Figure 12 shows the signal amplitude in each channel of spectral window 0 toward AS209 from project ID 1015.1.00486.S. This shows a line ranging from channel 0 to channel 40. The common practice in making continuum images is to exclude any channels containing spectral line emission.

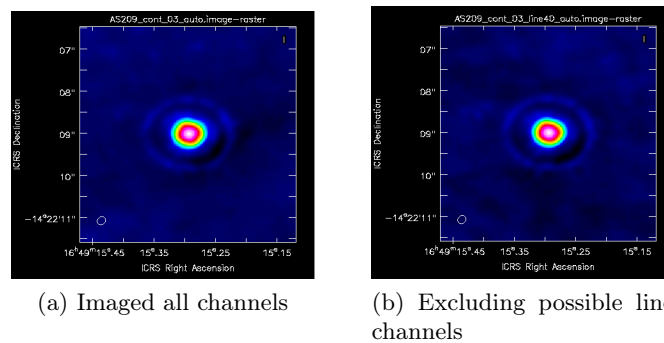


Figure 13: 230 GHz continuum (color scale) images of low resolution observations of AS209 produced with natural weighting. Beam size approximately $0.2094'' \times 0.1794''$. Left (panel a) includes all channels, right (panel b) excludes the line channels (0-40)

Figure 13 shows the difference between an image that has included the line ranging from channel 0-40 (panel a) when producing a continuum image and an image excluding this line emission (panel b). These images look very much alike, but Figure 13 panel (b) has slightly more contrast in the rings.

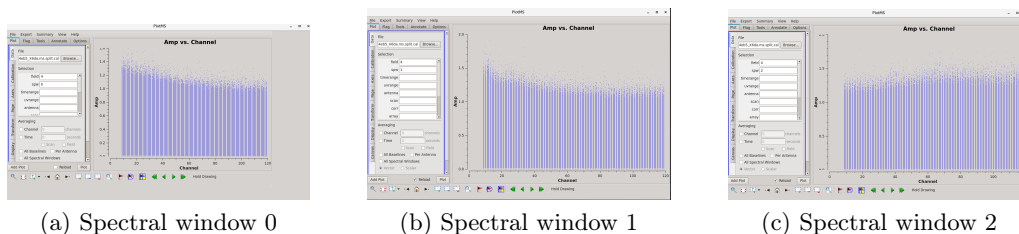


Figure 14: Three spectral windows containing the signal amplitude in each channel indicated with blue dots from high resolution observations of AS209, shown with *plotms*. This function allows the user to identify any channels which contain spectral lines.

Figure 14 shows the amplitude per channel of three different spectral windows. No clear line emission (like in Figure 12) can be seen because it comes from different observation in a different frequency range. Spectral window zero (Figure 14 panel a) and spectral window one (Figure 14 panel b) show a similar slope in the first 50 channels, whereas spectral window two (Figure 14 panel (c)) shows a dip in these channels but is almost flat.

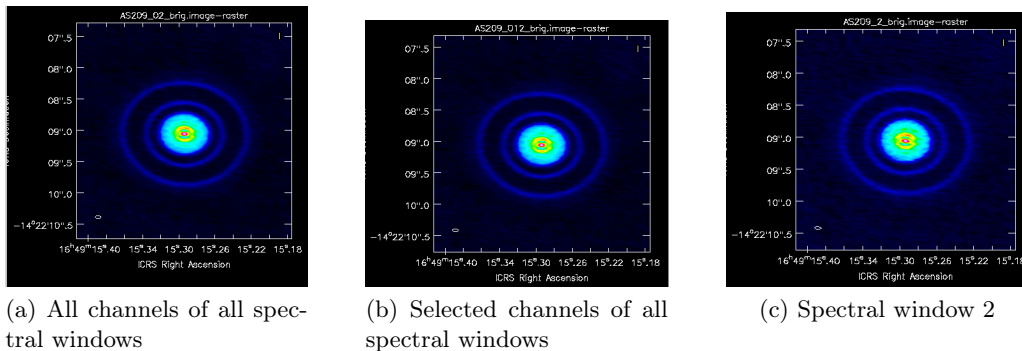


Figure 15: 240 GHz continuum (color scale) images of AS209, produced with Briggs weighting robust 0.5. Left (panel a) includes all channels of all spectral windows. Middle (panel b) excludes the slope channels (0-50 of spectral window 0 and 1) both have approximately beam size $0.0989'' \times 0.0430''$. Right (panel c) includes all channels of spectral window 2 and has beam size $0.1026'' \times 0.0507''$.

In Figure 15 there are three images for which the channel and spectral window selection is different. Figure 15 panel (a) was produced using all channels of all three spectral windows, including the bumps and dips. Figure 15 panel (b) was produced using all three spectral windows but imaging only the channels that do not have a bump: for spectral windows 0 and 1, channel 50 till 120, and for spectral window 2, all channels. Figure 15 panel (c) has been produced using all channels from spectral window 2. The differences are not clearly visible, especially Figure 15 panel (a) and Figure 15 panel (b) look the same, but in Figure 15 panel (c) the background noise is visibly higher, resulting in a brighter background and thus a less clear disk versus the background.

Image	ν (GHz)	Beam size	Flux density (mJy)	Peak intensity (mJy/beam)	Rms Noise (μ Jy/beam)	SNR
(1)	(2)	(3)	(4)	(5)	(6)	(7)
15a	239.7	$0.0989'' \times 0.0430''$	211	3.60	21	175
15b	239.8	$0.0989'' \times 0.0430''$	213	3.62	23	161
15c	249.9	$0.1026'' \times 0.0507''$	233	3.80	36	106

Table 8: Properties of the continuum images from Figure 15, which shows the effect of varying spectral window and channel selection. Column 1: figure number. Column 2: central frequency. Column 3: synthesized beam size. Column 4: flux density of the disk taken from within a fitted ellipse. Column 5: peak intensity in the image. Column 6: averaged rms noise level of image. Column 7: signal to noise ratio.

Table 8 lists the properties of the images shown in Figure 15. The central frequency values vary from 239.7 to 249.9 GHz depending on which spectral windows are included. The beam sizes for panel (a) and (b) are the same at $0.0989'' \times 0.0430''$ and $0.1026'' \times 0.0507''$ for panel (c). The flux densities range from 211-233 mJy with peak intensities from 3.60-3.80 mJy/beam.

The rms noise levels are 21-36 $\mu\text{Jy}/\text{beam}$ resulting in signal-to-noise ratio of 175, 161, and 106 for panel a, b and c respectively. The higher rms for 15c listed in Table 8 reflects the brighter background seen in Figure 15 (c)

The same analysis was done for Elias 24, Figures 30 and 31 and Table 15 in the appendix, giving the same result.

Weighting and deconvolver

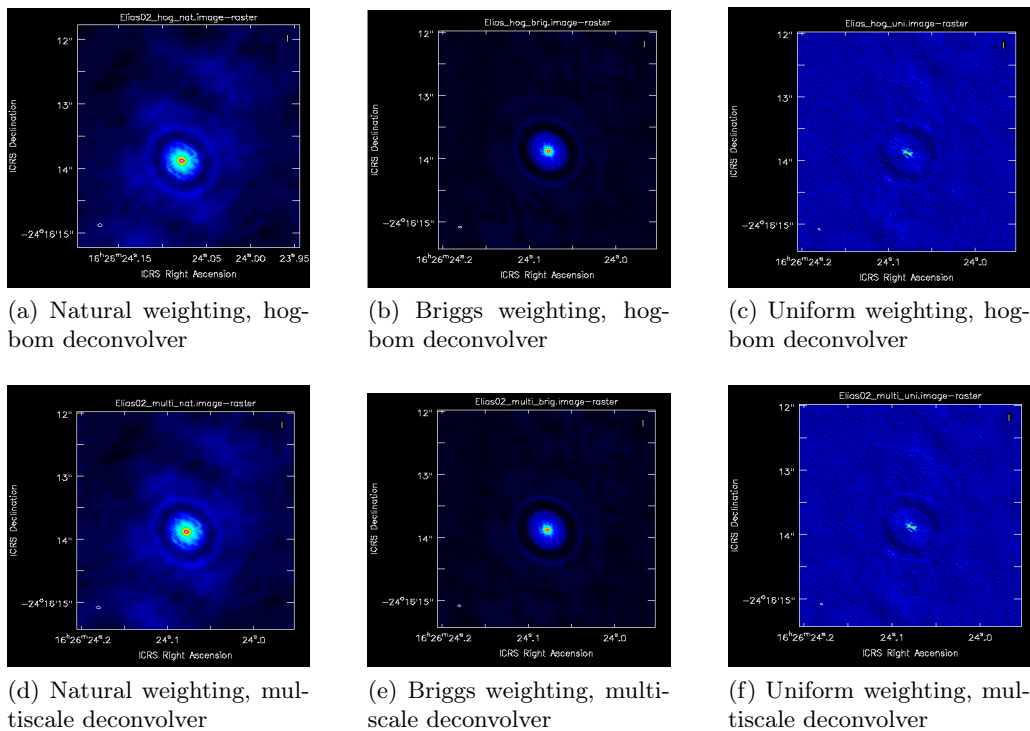


Figure 16: 240 GHz continuum (color scale) images of Elias24. The left images (panel a & panel d) are produced with natural weighing and have beam size $0.0722'' \times 0.0381''$. The middle images (panel b & panel e) are produced with Briggs weighing with robust parameter 0.5 and have beam size $0.0494'' \times 0.0287''$. The right images (panel c & panel f) are produced with uniform weighing and have beam size $0.0405'' \times 0.0202''$. Images in the upper row (panel a & panel b & panel c) are produced with the hogbom deconvolver. Images in the lower row (panel d & panel e & panel f) are produced with the multi-scale deconvolver.

Figure 16 shows six images representing different deconvolver- and weighting-settings. The images in the top row (panels a & b & c) are produced using the default deconvolver setting of 'hogbom', whereas the images in the bottom row (panels d & e & f) are produced using the deconvolver setting 'multiscale'. The visual difference between these two deconvolvers is minimal. In the left column (panels a & d) the images are produced using natural weighting. These images show a very bright ring and a larger but more transparent ring, which is difficult to see as the background is has a very bright patch at the location of the ring as well. In the central column (panels b & e) the images are produced using the Briggs weighting with a robust parameter of 0.5. These images show less background noise, the large gap and the bright ring are clearly visible and the larger more transparent ring is difficult to distinguish from its background. The

right column (panels c & f) contains images that are produced using uniform weighting. These images have a very grainy look, which makes the gap clearly visible, the ring less visible and the larger more transparent ring invisible as it is blended with the background.

Image	ν (GHz)	Beam size	Flux density (mJy)	Peak intensity (mJy/beam)	Rms Noise (μ Jy/beam)	SNR
(1)	(2)	(3)	(4)	(5)	(6)	(7)
16a	239,7	0.0722" x 0.0381"	583	7,12	210	34
16b	239,7	0.0494" x 0.0287"	216	4,41	29	154
16c	239,7	0.0405" x 0.0202"	22,5	2,59	86	30
16d	239,7	0.0722" x 0.0381"	583	7,12	210	34
16e	239,7	0.0494" x 0.0287"	215	4,41	29	154
16f	239,7	0.0405" x 0.0202"	22,5	2,59	86	30

Table 9: Properties of the continuum images from Figure 16 which shows the effect of different deconvolver and weighting settings. Columns as in Table 8

Table 9 lists the properties of the images shown in Figure 16. The central frequency is 239.7 GHz for all images. The beam sizes for panel (a) and (d) are the same at 0.0722" x 0.0381", the beam sizes for (b) and (e) are the same at 0.0494" x 0.0287" and for (c) and (f) are the same at 0.0405" x 0.0202". The flux densities range from 22-583 mJy with peak intensities from 2.95-7.12 mJy/beam, and the rms noise levels are between 29-210 μ Jy/beam both depending on the different weightings, resulting in signal-to-noise ratio of 34 for panel (a) and (d), 154 for panel (b) and (e), and 30 for panel (c) and (f).

As the values in Table 9 for a, b and c are the same as those in d, e and f, respectively, it can be seen numerically as well as visually that the choice of deconvolver is not important to this type of imaging. And as can be seen in Figure 16, the images using Briggs weighting show the structures the best and have the lowest rms noise according to Table 9.

The same analysis was done for both data sets of AS209 and can be found in the appendix in Figure 32 and 34 and Table 16.

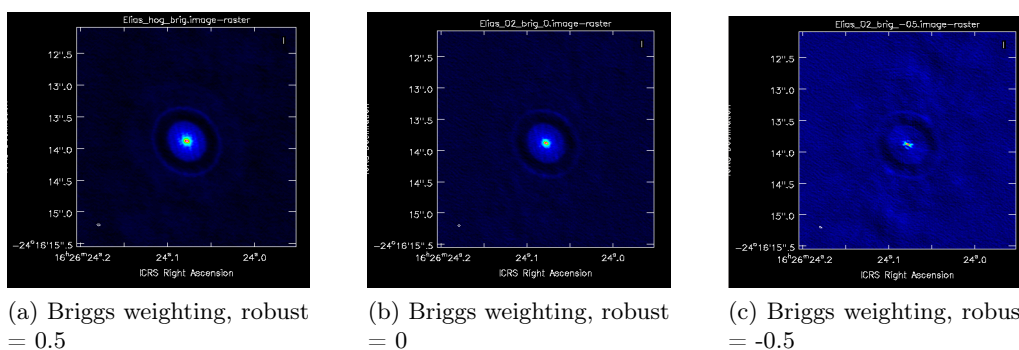


Figure 17: 240 GHz continuum (color scale) images of Elias24. Left (panel a) has Briggs weighing, robust parameter 0.5 and beam size 0.0424" x 0.0238". Middle (panel b) has Briggs weighing, robust parameter 0 and beam size 0.0494" x 0.0287". Right (panel c) has Briggs weighing, robust parameter -0.5 and beam size 0.0413" x 0.0210".

In Figure 17 three images are shown that are all created using Briggs weighting with three different robust values. The lower the value of the robust parameter, the more the image looks like uniform weighting, the grainier the image looks and the harder the extended ring is to distinguish from the background.

Image	ν (GHz)	Beam size	Flux density (mJy)	Peak intensity (mJy/beam)	Rms Noise (μ Jy/beam)	SNR
(1)	(2)	(3)	(4)	(5)	(6)	(7)
17a	239,7	0.0424" x 0.0238"	216	4,41	29	154
17b	239,7	0.0494" x 0.0287"	148	3,57	34	105
17c	239,7	0.0413" x 0.0210"	24,5	2,66	47	56,4

Table 10: Properties of the continuum images from Figure 17, which shows the effect of different Briggs robust values. Columns as in Table 8

Table 10 lists the properties of the images shown in Figure 17. The central frequency is 239.7 GHz for all images. The beam sizes is for panel (a): 0.0424" x 0.0238", for panel (b): 0.0494" x 0.0287" and for panel (c): 0.0413" x 0.0210". The flux densities range from 24-216 mJy with peak intensities from 2.66-4.41 mJy/beam, and the rms noise levels are between 29-47 μ Jy/beam both depending on the different values for the robust parameter, resulting in a signal-to-noise ratio of 154 for panel (a), 105 for panel (b) and 56.4 for panel (c).

The same analysis was done for both data sets of AS209 in the appendix, Figures 33 and 35 together with Table 17 show the results.

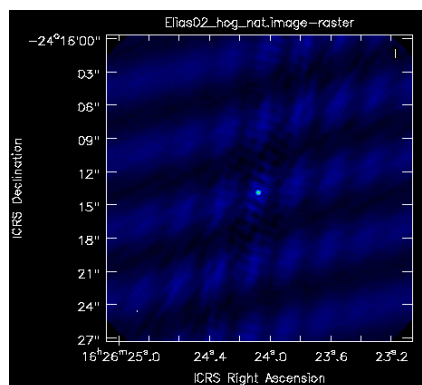


Figure 18: Non-zoomed 240 GHz continuum (color scale) image of Elias24 with natural weighting shown in Figure 16 panel (a) . Beam size 0.0722" x 0.0381".

In Figure 16, the images produced with natural weighting have a bright patch in the background, making it more difficult to distinguish the structures. Figure 18 shows the complete pattern of brighter patches of this image produced with natural weighting. Figure 36 in the appendix shows the exact same pattern for three different deconvolver settings; hogbom (panel a), multi scale (panel b) and multi-term multi-frequency synthesis (panel c). The values are listed in the first row of Table 9.

Interactive cleaning

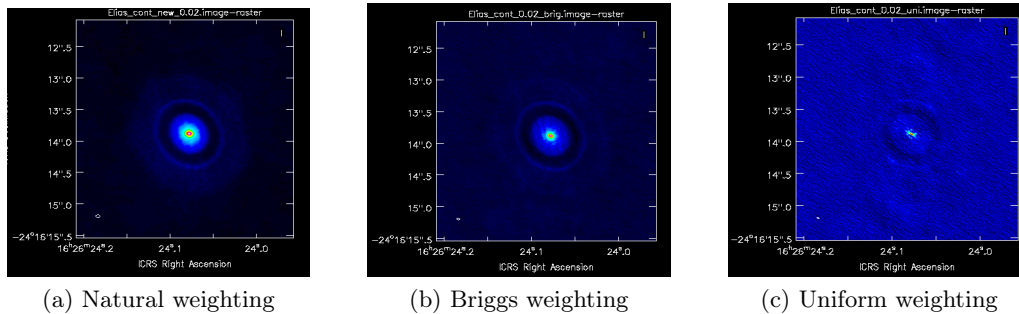


Figure 19: 240 GHz continuum (color scale) images of Elias24 produced with interactive cleaning. Left (panel a) has natural weighting and beam size $0.0722'' \times 0.0381''$. Middle (panel b) has Briggs weighing, robust parameter 0.5 and beam size $0.0494'' \times 0.0287''$. Right (panel c) has uniform weighing, beam size $0.0405'' \times 0.0202''$.

Figure 19 shows three images that are all made using interactive cleaning instead of auto-masking, but have different weightings. The image in panel (a) of this figure is produced with natural weighting and shows all three feature, the inner gap, the brighter ring and the more extending transparent ring clear. The image in panel (b) of this figure is produced with Briggs weighting and shows the gap and the ring clearly, but the more extending, more transparent ring is barely visible. The image in panel (a) of this figure produced with uniform weighting is very grainy, which makes the gap clearly visible, the ring less visible and the larger more transparent ring invisible compared to the background.

Image	ν (GHz)	Beam size	Flux density (mJy)	Peak intensity (mJy/beam)	Rms Noise (μ Jy/beam)	SNR
(1)	(2)	(3)	(4)	(5)	(6)	(7)
19a	239,7	$0.0722'' \times 0.0381''$	405	7,05	49	144
19b	239,7	$0.0494'' \times 0.0287''$	202	4,43	29	154
19c	239,7	$0.0405'' \times 0.0202''$	227	2,59	86	30

Table 11: Properties of the continuum images from Figure 19, which shows the effect of different weighting methods using interactive cleaning. Columns as in Table 8

Table 11 lists the properties of the images shown in Figure 19. The central frequency is 239.7 GHz for all images. The beam sizes is for panel (a): $0.0722'' \times 0.0381''$, for panel (b): $0.0494'' \times 0.0287''$ and for panel (c): $0.0405'' \times 0.0202''$. The flux densities range from 202-405 mJy with peak intensities from 2.59-7.05 mJy/beam, and the rms noise levels are between 29-86 μ Jy/beam both depending on the different values for the robust parameter, resulting in a signal-to-noise ratio of 144 for panel (a), 154 for panel (b) and 30 for panel (c).

Primary beam correction

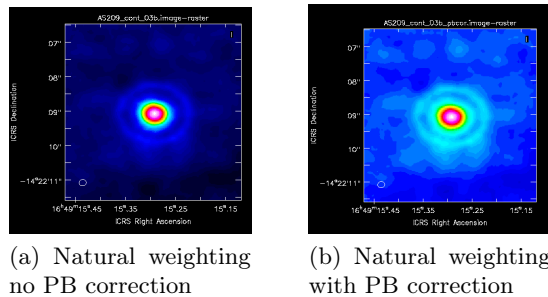


Figure 20: 240 GHz continuum (color scale) images of AS209 produced with natural weighting. Left (20a) has no primary beam correction. Right (20b) has a primary beam correction. Beam size $0.2098'' \times 0.1816''$

Figure 20 shows the difference between an image that did not have a primary beam correction (panel a) and an image that is corrected for the primary beam (panel b). It can be seen that the images with a primary beam correction shows brighter patches in the background, which might make the rings mess distinguishable.

7.3 Final images

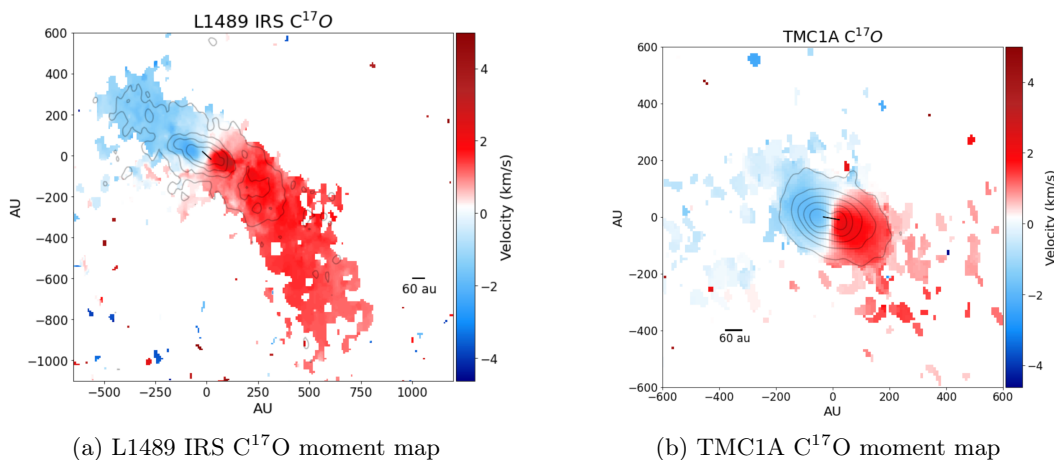
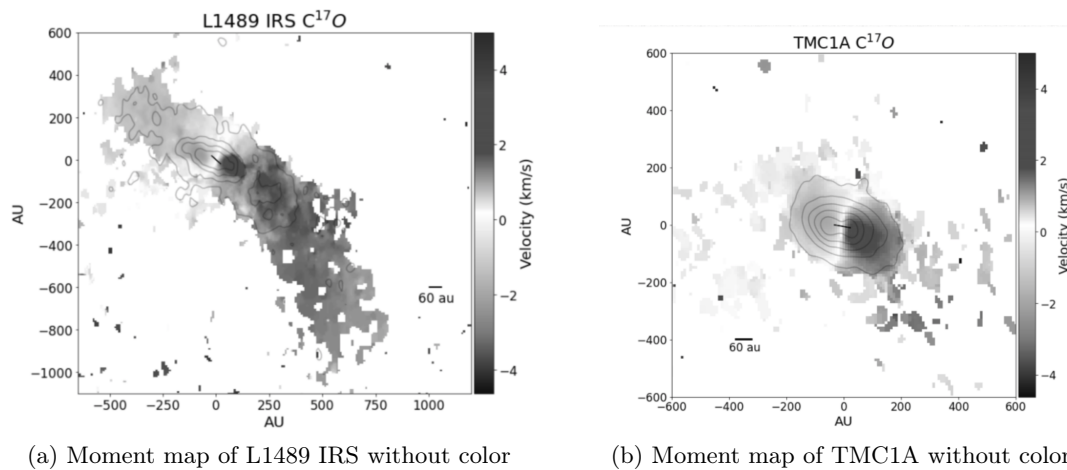


Figure 21: Left (panel a) Moment 0 (white contours) and moment 1 (color scale) maps of $C^{17}O$ towards L1489 IRS. Contours at (0.015, 0.045, 0.075, 0.105, 0.135) Jy/beam. Color scale runs from 5.0 km/s (blue) to 10.8 km/s (red). Beam size $0.5562'' \times 0.3877''$. Right (panel b) Moment 0 (white contours) and moment 1 (color scale) maps of H_2CO towards TMC1A. Contours at (0.045, 0.135, 0.225, 0.315, 0.405) Jy/beam. Color scale runs from 4.3 km/s (blue) to 8.5 km/s (red). Beam size $0.5625'' \times 0.3695''$.

The final moment 0 and 1 maps, shown in Figure 21, were chosen to show the kinematics of the disk the best. For L1489 IRS the Figure 9 panel a and for TMC1A the image of Figure 11 panel c were selected as they show the emission of $C^{17}O$, which traces the disk best. The arguments of the imaging processes are given in Table 12 These images were formatted in python, so the color and scales could be altered. A color scheme was made using '*LinearSegmentedColormap*' from the matplotlib.colors package with the colors; darkblue, dodgerblue, lightskyblue , white,

red, firebrick, darkred to make sure the difference between red and blue is also visible for color blind people (Figure 22). The axis are in AU and the size of our solar system was added with a black line together with a black bar of 60 AU in the right (for L1489 IRS) or left (for TMC1A) corner for scaling purposes.



(a) Moment map of L1489 IRS without color

(b) Moment map of TMC1A without color

Figure 22: Same moment maps as shown in Figure 21, in grayscale as an approximation of how color blind people would see the images

Image	L1489 IRS mom 0	L1489 IRS mom 1	TMC1A mom 0	TMC1A mom 1
imagenname	... sp33.cube	... sp33.cube	... sp33.cube	... sp33.cube
Moments	0	1	0	1
Axis	spectral	spectral	spectral	spectral
Chans	387-505	387-505	410-528	410-528
Includepix	-1	[0.02,100]	-1	[0.025,100]

Table 12: CASA *immoments* input parameters for the final moment maps of both L1489 IRS and TMC1A.

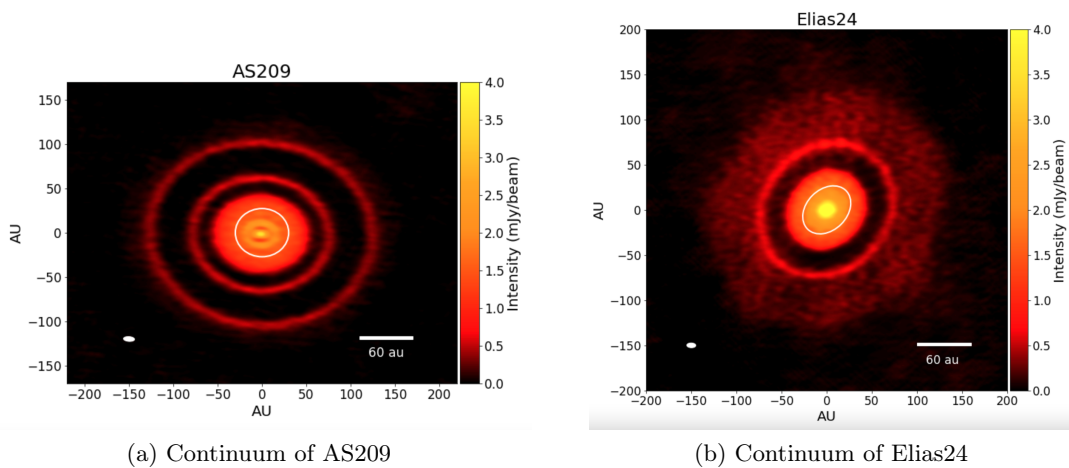


Figure 23: Left (panel a) shows the final 240 GHz continuum (color scale) image of AS209, produced with natural weighing and has Beam size $0.0992'' \times 0.0429''$. Right (panel b) shows the final 240 GHz continuum (color scale) of Elias24 produced with interactive cleaning and natural weighting, and beam size $0.0722'' \times 0.0381''$.

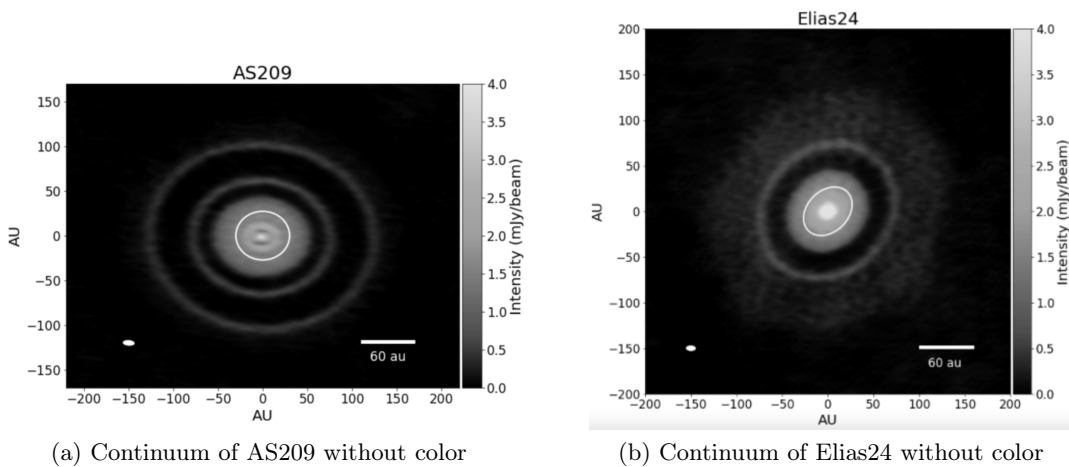


Figure 24: Same continuum images as shown in Figure 23, in greyscale as an approximation of how color blind people would see the images

The final continuum images, shown in Figure 23, were chosen to show the structures of the disk the best. For Elias24 the structures are best visible in Figure 19 panel a, and for AS209 the structures are best shown in Figure 35 panel (a). The arguments of these cleaning processes are given in Table 13. These images were also formatted in python. A color scheme was made using *'LinearSegmentedColormap'* from the *matplotlib.colors* package with the colors black, red, orange-red, dark-orange, orange, gold and yellow. The scale bar is set to zero so most noise is neglected, making the background darker and thus the structures better visible. The beam size is plotted in the left corner, the axis are labeled in astronomical units and size of our solar system was plotted as a white contour as well as with the black bar of 60 AU in the right corner. Finally Figure 24 shows the continuum image in greyscale as an approximation of how color blind people would see the images of Figure 23.

Image	Elias 24	AS209
Vis	uid_..._A002_Xc53e4e...	uid_..._A002_Xc44eb5...
Field	4	4
Spw	02	0:50-120, 1:50-120, 2'
Imsize	9216	9216
Cell	0.003arcsec	0.003arcsec
Specmode	mfs	mfs
Weighting	natural	briggs
Robust	-	0.5
Niter	10000	10000
Usemask	user	auto-multithresh
Interactive	True	False

Table 13: CASA *clean* input parameters for the final continuum images of both Elias24 and AS209.

Figure 25 shows a brightness profile produced from the final image of AS209 shown in Figure 23 panel (a).

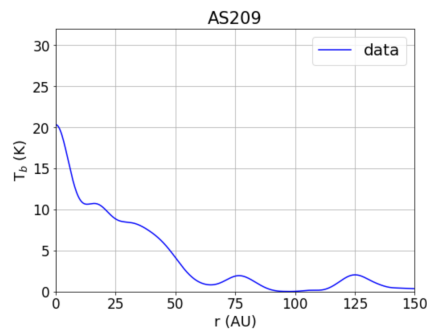


Figure 25: Brightness temperature profile of AS209 from Figure 23 (a) (originally from Figure 35 (a)) obtained with equation 6.

Figure 25 shows a brightness profile produced from the final image of AS209 shown in Figure 23 panel (a). The data shows the intensity converted to brightness temperature vs the radial displacement. The line shows multiple bumps and dips in intensity, caused by piled up and repelled gas and representing rings and gaps. There are two smaller bumps close to the centre, located at approximately 20 and 30 AU and two larger bumps at approximately 77 AU and 123 AU.

Compare with DSHARP

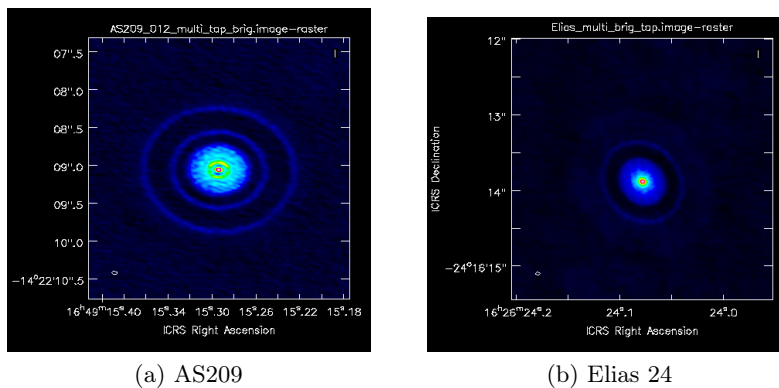


Figure 26: Left (panel a) shows continuum image of AS209 produced with settings similar to Dsharp (Briggs weighting, robust -0.5 and tapering $0.037'' \times 0.01'' \times 162.0^\circ$). Beam size $0.0797'' \times 0.0378''$. Right (panel b) shows continuum image of Elias24 produced with settings similar to Dsharp (Briggs weighting robust parameter 0.5 and tapering $0.035'' \times 0.01'' \times 166.0^\circ$). Beam size $0.0573'' \times 0.0376''$.

For AS209, a Briggs weighting with robust parameter of -0.5 is used, together with the multi scale deconvolver and a tapering of 37 by 10 milli-arcsecond and 162° . The inner ring is clearly distinguishable, but the background is slightly brighter than in Figure 23 (a), making the contrast a bit less clear.

In Figure 26, the images were produced with settings similar to the ones used in S. M. Andrews, Huang, et al. 2018. For Elias 24, a Briggs weighting with robust parameter of 0.0 was used, together with the multi-scale deconvolver and a tapering of 35 by 10 milliarcsecond and 166° . The large gap and its ring are clearly visible, the larger more transparent ring is just visible.

S. M. Andrews, Huang, et al. 2018 produced the images using self calibration, so the images shown here do not look the same as the images in the paper. The images in Figure 26 look similar to the final images. Especially for AS209, the differences between Figure 26 panel (a) and Figure 35 panel (a) are minimal. The structures of Elias24 are better visible in Figure 19 panel (a), which shows the power of interactive cleaning.

7.4 Guidelines for the script of the show on planet formation

Throughout the whole show, use storytelling techniques and make the theory understandable by using real life examples, but avoid overusing metaphors as they can also confuse the audience.

Get attention of the audience and introduce subject

'Have you ever wondered if there is life elsewhere in the universe? And is our Earth a unique planet? To answer this we need to know how our Earth and solar system are formed.' (*Show our solar system*) The ancient Greeks thought about these questions as well. They first thought the sun was orbiting our Earth because the sun rises and sets everyday. Later our perception was altered when Copernicus realized the Earth and the other planets were orbiting the sun. Later, with the understanding of the laws of gravity, the theory of planet formation started to form and our own solar system helped us to develop this theory. For example, the fact that all the planets orbit roughly in the same plane, is linked to the formation of the planets.

Geology has helped astronomers understand the age of the Earth, with the help of radioactive dating. This technique uses the decay properties of radioactive isotopes to calculate the age. (*Show image of radioactive decay cycle, like Figure 27*) Radioactive isotopes have a certain property called the half life, the time in which exactly half of all isotopes will have decayed (*explain what the image shows*). By looking at the ratio between the original isotopes and their products, the age of the Earth can be determined. Astronomers now know the age of the Earth is about 4.5 billion years, which is approximately the same as the age of our sun.

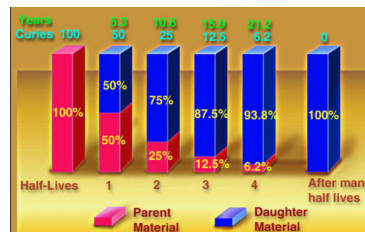


Figure 27: Example of half life image to show to the public (University n.d.).

Explain the research question / inspiration of the research

Astronomers used all these 'natural laws' to build a theory about planet formation, but because this was mainly theoretical, astronomers wondered if they could find observational evidence for the expected evolutionary stages, so they started using telescopes.

Introduce concepts needed to convey your story

In 1655, Christiaan Huygens built one of the first simple optical telescopes, which was used to look at Saturn and its moons, for example. (*Show image of Christiaan Huygens telescope*). You could place your eye at one side of the telescope, point the other side toward the planet and directly observe the reflected light of the sun.

But this form of light, called 'visible light' as we can observe it with our own eyes, is not the only form of light that is emitted by astronomical objects. Let's have a look at the different forms of radiation, that are used to look at different properties of the source. (*Show overview of electromagnetic spectrum*) (*and name all relevant forms of radiation*), (*Show an object observed in different wavelengths*) (*and explain what the radiation traces*). Gamma rays are the most

energetic and trace things like supernovae and pulsars. With visible light we see stars. With infrared and radio we can see heated dust etc...

An atom can also emit light, when an electron in the atom loses energy or when a molecule rotates (*Show image of line emission, something like Figure 28*). Every transition in an atom emits at a very specific wavelength. We will come back to this later as it can be used to determine velocities.

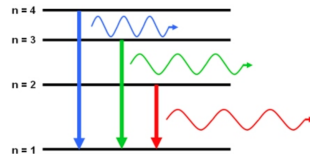


Figure 28: Example of line emission image to show to the public (Cosmos [n.d.](#))

Introduce the telescope used, to show people how the data was gathered

In 1990 the Hubble telescope was launched (*Show Hubble telescope*), this telescope is used to image our first stage of planet formation

Explain what you see in the first image, Orion nebula

To obtain observational evidence, the first evolutionary stage that is imaged is the molecular cloud. Hubble has observed different forms of radiation emitted by the Orion nebula. (*Show Hubble image of Orion nebula*) You might recognise this image as it is a gorgeous colorful image. But note that this image is not how we would see it with our eyes, as Hubble has combined different images of different forms of radiation to get this final image. Which means the image shows visible, blue, infrared and line emission of ionized hydrogen together in one image.

Explain the goal of this stage/image.

A molecular cloud is a very cold and dense, which means many molecules compact together. This is the place where stars are born, and thus sets the environment of planet formation. A small disturbance can cause a dense patch to collapse under its own gravity, forming a prestellar core. The cloud was spinning very very slowly because of the disturbances, and when the cloud collapsed, it began to spin faster due to the conservation of angular momentum. Think of the ice skater doing a pirouette, when she brings her hands in, she spins faster, just as the molecular cloud brings mass inward and will spin faster, this spinning gas is visible in the next stage.

Introduce the telescope used, to show people how the data was gathered

To image the next stage the radio observatory of ALMA is used (*Show image/movie of ALMA*), which means it images the light in radio waves. This is an observatory in which 66 antennas work together to get high resolution images.

Give extra background information needed, so images can really convey information

So astronomers let ALMA observe a molecular cloud in the constellation of Taurus. Every cloud contains multiple young stars in different evolutionary stages, but from this cloud two Class I sources were imaged, to show the next crucial state. This stage is imaged by looking at the line emission of the gas (*Show an absorption line*). Which means the gas emits light at a certain

wavelength as the molecule loses energy as seen before. (*Show blue shifted and red shifted line*) If the observed wavelength is slightly different than the expected specific wavelength, the velocity of the source can be traced. If the source is moving towards us, the wave will be compressed resulting in bluer light, whereas the light of source moving away from us is stretched out resulting in redder light. This effect is called the Doppler effect, and also happens with sound waves. Ever noticed that an ambulance driving towards you has a higher pitch and an ambulance driving away has a lower pitch.

Explain your second image or step, L1489 IRS and TMC1A

This movement of the gas can be seen in a moment map (*Show moment map enlarged from the right location on the sky*). Where the blue color represents gas moving towards us and red is gas moving away from us, thus showing a clear rotation of the gas. The axis are given in astronomical units, where 1 AU is the distance between Earth and the sun. And to give a bit of perspective, a thin green line is added to the image that shows the size of our solar system. You can see that the gas is extending way further out, as these stars are still very young and still need to get compacter.

When the gaseous cloud is rotating, a disk will form due to the laws of angular momentum. Maybe you can imagine, the harder you spin the stronger you feel the force pulling you outwards (*If possible show simulation rotating and flattening out*). You can also imagine the pizza dough spinning on the bakers finger feels a force and will flatten out, the same happens for the material in the rotating cloud, forming a flat disk due to the conservation of angular momentum. In these images we used a molecular line that mainly appears in the disk, and thus shows the rotational movement of gas in the newly formed disk. This disk is the place where planets will start to form, which starts in these early stages as dust particles, mixed in with the gas, stick together to form larger particles. That these planets form in a disk agrees with the fact that the orbits of our solar system are all in the same plane.

Explain the next image/stage, Elias24 and AS209

To understand the observational evidence of the next evolutionary stage, I show two images that ALMA took of two different objects in the Rho Ophiuchi cloud complex, near the constellation of Libra. (*Show continuum images*) These images show the dust, which are tiny particles, smaller than sand, in the disk. The dust in the disk around the star is heated, just as we get heat from the sun and when the dust is heated it will emit in radio waves, you can compare this with red glowing coal when it's heated, but now the dust is not emitting in visual but in radio, which is not visible by eye but is made visible by ALMA.

The dust in the disk shows interesting structures. Astronomers made simulations to mimic these structures and came to the conclusion that the structures of these disks are probably caused by forming planets. The planets had already started to form in the earlier stage when dust began clumping together, but now larger particles are sticking together and grow in size. These planetesimals, which are solid objects formed by clumped dust particles, keep collecting and accumulating dust, clearing all material in their paths, leaving an empty lane while growing in size. These forming planets therefore cause structures to occur. (*Maybe point to the place where models think planets should be forming, or explain in words: right inside/outside that ring*). To give some more perspective the size of our solar system is added as a white ellipse. It can be seen that the planet formed here is located way further from the star than Neptune is from our sun.

Introducing the final stage

Now we look at observational evidence of the final stage: a planetary system. Until now we have already found more than 5000 exoplanets with different detection techniques. One of these techniques is directly imaging.

Introduce the telescope used, to show people how the data was gathered

For this technique an observatory is needed that uses optical telescopes, which means it images the light we can also see with our own eyes. (*Show images observatory*). This form of radiation is observed because the planets reflect the visible light from their star. For the source we show here, the telescopes of Gemini North Observatory and W.M. Keck Observatory in Hawaii are used.

Explain the next image/stage → HR8799

(*Show animation of planetary system (by J. Wang, Caltech/C. Marois, NRC-HIA)*). This planetary system shows 4 planets that are orbiting their star. These planets are observed as they reflect the light from the stars, just as we can see the reflection from Jupiter or Mars sometimes. When we look at the dust, using the radio waves as before, only a ring of dust is observed outside the orbiting planets, which can be compared to our Kuiper Belt, which is a ring outside our solar system consisting of small bodies. Inside this ring, most dust and gas is cleared out by these massive planets. (*If good enough resolution: show the continuum*).

Give a summary / conclusion

(*Show all 4 stages next to each other*). Now we can see that different parts of the sky are observed with different types of telescopes, to obtain observational evidence for the evolutionary timeline of the formation of planets. First, we have a dense cold molecular cloud that collapses and forms a core. The gas will then be rotating, as we can see in the second image, and due to the laws of physics, conservation of angular momentum to be precise, we know a disk of material is forming. Astronomers think that planets start to form in this stage when dust sticks together and form larger particles. Next, we see the structures in the dust disk, that are created by forming. Finally, we see a directly imaged planetary system, where most of the dust and gas has been cleared away by four large planets.

Give future perspectives

But be aware that this is just the bigger picture. There are still many uncertainties and especially the details on how planets exactly gain all the mass is still unknown. We started the show with the question if the Earth is unique, and by getting to know the details of planet formation we get closer to this answer. This also brings us closer to the question if there is life elsewhere in the universe. (*Show image James Webb*) A new space telescope called James Webb might take a step in answering this question as it will look at the atmospheric properties of exoplanets, to see if it looks habitable. (*Maybe explain what observation methods it uses?*) So to get to know the details on planet formation, new observations need to be done and precise models need to be made in which the conditions of the environment need to be implemented to simulate the processes happening around planet formation. So with the power of ALMA and the new data of James Webb we can unravel more details in the story of planet formation.

8 Discussion

In this section I will discuss the results of the images produced with different settings for both the moment maps produced with *immoments* and the continuum images produced with *tclean*. I will conclude what are useful arguments and settings for imaging for outreach purposes.

8.1 Moment maps

In this section different moment maps of L1489 IRS and TMC1A, produced using the emission of different molecular species, are discussed. The moment maps were produced to show the rotation of the gas that point to the formation of a disk as the second step of planet formation

L1489 IRS

For L1489 IRS three moment maps using the emission of three different molecular species: CN with frequency 226.87478 GHz, H₂CO with frequency 225.697775 GHz and C¹⁷O with frequency 224.714385 GHz.

Figure 7 shows the moment maps of the CN molecule. Besides the upper layers of the embedded disk, this molecule also traces the outflow cavity walls. It clearly shows some sort of rotation, but is more chaotic than C¹⁷O in Figure 9, as more emission is included. This chaotic emission is likely caused by the emission from the outflow cavity walls since they are located next to the envelope and the disk (Figure 3). For the threshold of the pixels included, it can be seen in Figure 7 panel (a) the image still contains some noise, whereas panel (b) and panel (c) do not contain noise. The moment map in Figure 5 panel (b) is the best as it contains all emission whereas Figure 7 panel (c) has excluded too many pixels.

Figure 8 shows the emission of H₂CO, which mainly traces the disk, but can also be tracing some parts of the outflow and the jets. The map shows clear rotation of the gas again, but compared to the disk in Figure 9, the emission is more extended around the disk. This is probably caused by the emission of H₂CO in the outflows that are close to the disk according to Figure 3. This does give a more complete image of the rotating gas cloud but not specifically for the disk. For this molecular species, Figure 8 panel (c), the image with the least pixels included, shows the emission the best as the other two still show some noise.

Figure 9 shows the emission of C¹⁷O, which is used to trace the disk. This image shows that L1489 IRS has a long extending rotating disk, as part of the disk is moving towards us (blue) and part is moving away from us (red). An image with the settings in between Figure 9 panel (a) and 9 panel (b) would show the emission of the disk the best, since Figure 9 panel (a) still shows some noise in the form of random colors, whereas Figure 9 panel (b) has excluded too many pixels resulting in some gaps.

Besides looking at the observable outcomes of the images, the measurements can be discussed as well and compared to other papers. Van't Hoff et al. 2020 found a systematic velocity of 7.2km/s, which is 2.7% and 5.2% different from the velocity I got when using the emission of H₂CO and C¹⁷O which is reasonable within error bound of a standard 10%. However, the value obtained from the CN emission is very different from the velocity measured for the other molecular species. It is possible that other physical components got mixed in as CN is not only

tracing the disk.

The inclination angle of L1489 IRS found in Yen et al. 2014 is 66° which is approximately the same angle I found when fitting ellipses by hand with three different methods. All the angles I found, except for the ellipse fitting the central zone of the H_2CO map (Table 4) and the ellipse fitting the 5σ contours of the C^{17}O map (Table 5), are in accordance with the angle found in Yen et al. 2014 within the observational error bounds. Van't Hoff et al. 2020 also found the position angle to be 69° , which is within the errors of most angles I found except for the ellipse fitted using 50% of the emission of CN and the ellipse fitted using 5σ of the emission of CN and C^{17}O .

It is likely that these cases are out of agreement because I fitted the ellipses manually rather than by using a model. When doing so I neglected part of the redshifted emission, as the emission is asymmetric. This emission could originate in an accretion stream of gas located between us and the disk which is falling onto the disk making the gas appear redshifted. The corresponding blue shifted accretion stream, which is not detected might not be visible because the disk and envelope block the emission. It is possible for this gas to be mapped in these moment maps if the molecular species is abundant. This asymmetry makes it more difficult to determine the inclination angle as well as the position angle, as the fitting of an ellipse is affected by this additional gas.

The area of emission found by Van't Hoff et al. 2020 27.86 arcsec^2 for both H_2CO and C^{17}O . The integrated flux in this area is 4.3 Jy km/s for H_2CO and 1.5 Jy km/s for C^{17}O . I used different areas that covered the emission best, where 5σ covers most of the emission, and central emission only covers the most intense emission. These differences make it difficult to compare these values, so I used the integrated flux measured in a circular aperture with a diameter of $6.0''$ to compare the flux densities of my work and Van't Hoff et al. 2020.

Van't Hoff et al. 2020 has measured the integrated flux within a circular aperture with $6.0''$ diameter, which resulted in 8.0 Jy km/s for the emission of H_2CO and 2.9 Jy km/s for the emission of C^{17}O . The values I measured (8.72 Jy km/s and 3.43 Jy km/s respectively) are slightly higher than the values found in this paper, which might be due to different settings of *includepix* when making a moment map using *immoments* which sets a minimum level of intensity. For H_2CO I used 0.03 Jy (which is higher than 3σ , taking $\sigma = 7\text{mJy}$) and for C^{17}O I used 0.02 Jy (which approximately 3σ , taking $\sigma = 7\text{mJy}$). Van't Hoff et al. 2020 states that they use 3σ with $\sigma = 5 \text{ mJy/beam}$, which means I excluded more pixels. The difference in including pixels could have led to a different value for flux density as well as the difference in the centre of the ellipse.

As final image to show the rotation of the gas and thus the formation of a disk of material, I've chosen Figure 9 panel (a) as C^{17}O , and CO isotopologues in general, traces the disk the best. I picked panel (a) as it shows the complete emission without black patches.

TMC1A

For TMC1A two moment maps were made, using the emission of two different molecular species: H_2CO with frequency 225.697775 GHz and C^{17}O with frequency 224.714385 GHz .

Figure 10 shows the emission of H_2CO , which mainly traces the disk, but can also be tracing some parts of the outflow and the jets. Rotation of the gas is clear since one part of the image is moving towards us (blue) and the other one is moving away (red), but the upper left blue part

is smeared out. This is possibly because the emission from the jets and outflows is also observed and thus imaged. For this molecular species an image with settings somewhere between the settings of Figure 10 panel (b) and (c) would show the velocity gradient the clearest, as Figure 10 panel (a) shows too much noise.

Figure 11 shows the emission of $C^{17}O$ of TMC1A, which is only used to trace the disk. It can be seen that the disk is quite compact and has a clear rotation. Panel (c) shows this rotation the best, as it does not contain any noise like panel (a) and (b).

Besides looking at the observable outcomes of the images, the measurements can be discussed as well and compared to other papers. Van't Hoff et al. 2020 found a systematic velocity of 6.4km/s, which is in accordance with the velocity found using the emission of $C^{17}O$ and has only a 3% difference with the velocity found using the emission of H_2CO which is reasonable within error bounds of a standard 10%.

The inclination angle of TMC1A found in Aso et al. 2015 is 65° which is higher than the angles I found when fitting an ellipse by hand, which have an average of 50° . It is likely that my values are different because I fitted ellipses by hand while they used models and because the emission of the moment maps is asymmetric and extended making it more difficult to fit an ellipse precisely. The ellipse fitted using the central emission of H_2CO is the same as found in Aso et al. 2015 within the errors. Van't Hoff et al. 2020 found a position angle of 73° for TMC1A which is within the errors of all the angles I found except for the ellipse fitted using 5σ of the emission of H_2CO .

The area of emission found by Van't Hoff et al. 2020 is 2.57 arcsec^2 for both H_2CO and $C^{17}O$. The integrated flux in this area is 0.1 Jy km/s for the emission of H_2CO and 1.1 Jy km/s for the emission of $C^{17}O$. I used different areas that covered the emission best, where 5σ covers most of the emission, and central emission only covers the most intense emission. These differences make it difficult to compare these values, so to compare the flux density, the integrated flux is measured in a the circular aperture with a diameter of $6.0''$.

Van't Hoff et al. 2020 also measured the integrated flux within a circular aperture with a diameter of $6.0''$, which resulted in 2.3 Jy km/s for the emission of H_2CO and 4.1 Jy km/s for the emission of $C^{17}O$. The values I measured (2.8 Jy km/s and 5.1 Jy km/s respectively) are slightly higher than the values found in this paper, which might be due to different settings of *includepix* when making a moment map using *immoments* which sets a minimum level of intensity. For H_2CO I used 0.02 Jy (which roughly corresponds to 3σ , taking $\sigma = 7\text{mJy}$) and for $C^{17}O$ I used 0.025 Jy (which slightly higher than 3σ , taking $\sigma = 7\text{mJy}$). Van't Hoff et al. 2020 states that they use 3σ with $\sigma = 5 \text{ mJy/beam}$, which means I excluded more pixels. The difference in including pixels could have led to a different value for flux density as well as the difference in the centre of the ellipse.

As the final image of TMC1A to show the rotation of the gas and thus the formation of a disk of material, I've chosen Figure 11 panel (c) as $C^{17}O$, and CO isotopologues in general, traces the disk the best. I picked panel (c) as it does not contain noise and shows a compact disk.

8.2 Continuum images

In this section, some of the settings of the cleaning algorithm *tclean* are discussed that are used to produce a continuum image. The continuum image is produced to show the structures in the disk and thus shows the third stage of planet formation. In this section I will discuss the influence of the primary beam correction, channel selection, the weighting, the deconvolver and interactive cleaning on imaging for outreach purposes and discuss the settings used in S. M. Andrews, Huang, et al. 2018 and my final images and make some comparisons based on the measurements I did.

Ellipse fitting

Fedele et al. 2018 found a position angle for AS209 of 85.8° which is in agreement with the value I found ($85^\circ \pm 4^\circ$). For the inclination they found an angle of 34.9° , which is just outside the error bound of the value I got ($33.6^\circ \pm_{-1.2}^{+1}$). The difference of the inclination angle of AS209 may be due to the fact that Fedele et al. 2018 found the values by modeling the disk instead of fitting an ellipse by hand. Dipierro et al. 2018 found an inclination angle of $28.5^\circ \pm 3.8^\circ$ and a position angle of $46.7^\circ \pm 6.5^\circ$, which are both in accordance within errors with the values I found ($31.6^\circ \pm_{-1.2}^{+1.1}$ and $43^\circ \pm 12^\circ$ respectively). The small difference is likely because I fitted the ellipse by hand instead of a model and the edge of Elias 24 is a bit blurry.

Primary beam correction

Primary beam correction is needed if images are used for flux measurements, but when we look at the influence it has on the imaging (Figure 20) it is clear that the image with primary beam correction has a more uniform intensity which makes the image less pleasing and makes the edges of the rings are less well defined. So primary beam correction can be neglected for public communication purposes, as we want the image to be aesthetically pleasing and the structures to be as clear as possible.

Channel selection

To make a proper continuum, line emission should be excluded. When plotting the amplitude over the channels, with *plotms*, a weak line (approximately 1.67 times the amplitude of the continuum emission) is visible for the image of AS209 produced with older data set, Figure 12. I produced an image with all the channels, including the line and an image without the channels that represent the line, Figure 13. The difference between these images is barely visible, but if you look closely, you can see a small difference in the darker area in between the rings, especially in the top left part. The difference is so small because the line was quite weak. This shows that for public communication purposes, flagging out the weak lines is not per se necessary. For stronger lines it might be necessary to exclude them, so it is still useful to analyze the data in *plotms* before imaging.

The same holds when we look at Figures 14 and 30 where there are small bumps visible in spectral windows 0 and 1. The plots look very similar because the exact same frequency range is observed. The line that was visible in Figure 12 is not detected in Figure 14, as the observed frequency range is different. The first image in Figure 15 and 31 is made including these bumps in the amplitude, while the second image excludes these bumps. The difference between those

images is negligible for imaging purposes. The third image is produced only with spectral window 2, which amplitude was almost flat. This image is a bit brighter in both cases, which makes the contrast of the structures less visible. The measurements of these images listed in Tables 8 and 15 show this as well. The image containing only 1 spectral window (panel c) has the highest intensity peak and integrated flux, but also has the highest rms noise, resulting in the lowest signal to noise ratio, which might make the contrast in the structures less visible. For my final images I used all three spectral windows, but for producing images for the public, this difference is barely visible so does not have to be taken into account.

Weighting

In Figures 16, 32 and 34 we compare different weighting settings and Tables 9 and 16 list some of the properties of these images. In the image with the natural weighting, the edges of the rings and structures are smoothed out because of the lower angular resolution, this is also shown by the measurements, as the beam size of the natural weighted image is the largest. Whereas for the uniform weighting the image becomes grainy and you can see that the flux density and peak intensity are a lot lower (resulting in the lowest signal to noise ratio), making the rings and other structures less visible. The images with the Briggs weighting are a compromise between the other two weighting schemes. The edges of the structures are a bit clearer, but the image is not too grainy and does not blend in with the background. The numbers also show that the rms noise of the Briggs weighted image is lowest, resulting in the highest signal to noise ratio. When comparing these numbers the figures of AS209 (Figure 32 and Table 16) are most useful, as the images of Elias 24 (Figure 16 and Table 9) show striping due to problematic baselines, discussed in detail later in this section. Table 16 makes the differences even clearer, as the uniform weighting has the highest rms noise and by far the lowest signal to noise ratio making the structures hardly visible. The natural weighting has a rms noise a bit higher than the Briggs weighting but also a flux density and intensity peak a lot higher which is visible by the bright rings. Finally, Briggs weighting has a lower peak intensity and flux density, making the rings less bright, but does have the lowest rms noise and highest signal to noise ratio making the structures appear best. This holds for both sources making the Briggs weighting setting very useful, but Briggs weighting has a "robust" parameter, which sets the relative importance of the uniform and natural weighting.

Figures 17, 33 and 35 show the images produced by three different robust parameters and Tables 10 and 17 show the properties of these images. The lower the robust value, the more the image looks like the uniform weighting and thus the grainier the image looks. The image not only looks more like the uniform weighting, but the lower the robust parameter, the lower the peak intensity, the higher the rms noise and the lower the signal to noise ratio. This grainy appearance may also give rise to more questions in conveying the theory of planet formation because of the odd texture that is shown in the structures, so the image should be weighted more towards the natural weighting than to the uniform weighting for public communication purposes. The exact appearance of the image depends on the story it needs to convey and on personal preferences. If there is time this is a parameter that can be experimented with, but $\text{robust} = 0.5$ is generally a safe choice and does give the highest signal to noise ratio and is thus recommended.

As mentioned before, the natural weighted images of Figure 16 have striping. Figure 36 panel (a) shows the full (zoomed out) image and a clear pattern of brighter patches can be seen. This is caused by one or more baselines that had a different signal, mainly stronger, compared to most

baselines.

To fix this problem, certain baselines in the observation can be flagged, this was done by S. M. Andrews, Huang, et al. 2018, and the way the pattern looks says something about which baselines should be flagged. I also looked for other ways to overcome this problem. It can be seen that the weighting does make a difference, as for Briggs weighting this pattern is hardly visible and with the uniform weighting it is not visible. That is because uniform weighting reduces the side lobes and weighs the baselines more evenly. Since Briggs weighting is in between natural and uniform, the patches are less visible for Briggs weighting and makes it thus less necessary to flag the baselines. The best way to get rid of the patches without flagging baselines (which is a more advanced data reduction skill and not expected from the targeted audience), is to use interactive cleaning, which is explained in the next section. I also tried different deconvolver settings as can be seen in Figure 36, but all these images show the same pattern. Figures 16, 32 and 34 also show the difference between the hogbom and multi scale deconvolver for all weighting schemes. In all these images, there is not a clear difference between these two settings and even the measurements shown in Tables 9 and 16 are exactly the same for the different deconvolver settings. So we can conclude that the deconvolution does not influence the images of these objects noticeably, therefore to image these disks the default deconvolver (hogbom) can be used (note for extended objects the multi-scale deconvolver is faster according to Cornwell 2008).

Interactive cleaning

When interactive cleaning is used, the user can choose their own mask after every iteration, this is used to look for extra emission after one iteration. When it seems like the cleaning is going well, a threshold can be set and CASA will finish the rest of the cleaning automatically. In Figure 19 three images are shown that were made using interactive cleaning but with different weighting schemes and Table 11 shows some of the properties. It is difficult to compare these images since the way the masks were defined in the cleaning process can be different (as it is done manually for each image) and thus might influence the way the image looks, but it can be seen that the interactive cleaning with natural weighting has produced a very clear image. The integrated flux and the peak intensity of the image shown in Figure 19 panel (a) is way higher than the one shown in Figure 17 panel (a). Even though the rms noise is also higher, resulting in a slightly lower signal to noise ratio, it can be seen that the higher flux results in a brighter structure, making the edges of the structures best visible in Figure 19 panel (a). The interactive cleaning also gets rid of the pattern of brighter patches produced by a deviating baseline, as these patches can be neglected by the user when choosing the mask. This can also be seen in the measurements shown in the first row of Table 9 and the first row of Table 11. It shows that the rms noise and thus the signal to noise ratio is way higher for the image shown in Figure 16 than for the image produced with interactive cleaning, which means interactive cleaning can help to get rid off the striping pattern. So if there is time or if the image shows a pattern, it is worth trying interactive cleaning, as it can improve resolution and remove striping patterns.

Compare with DSHARP

In Figure 26 I used most of the *tclean* settings that were used in DSHARP as well, for example the same weighting and tapering. But the images in S. M. Andrews, Huang, et al. 2018 do look different then the ones shown in Figure 26 as they use self calibration which I did not use, since self calibration is a time-consuming process and requires expertise. The images in Figure 26 do look similar to the final images. Especially for AS209, the differences between Figure 26

panel (a) and Figure 35 panel (a) are minimal. The main difference between these images is the tapering and the robust parameter. The robust parameter in 26 panel (a) is -0.5 which sets the weighting more towards the uniform weighting, causing a brighter background as the RMS noise is higher which makes the structures less visible, which is why a robust parameter of 0.5 was chosen for my final image. The tapering does not seem to influence the image noticeably with pipeline line cleaning and does therefore not have to be considered by our target user. The structures of Elias24 are better visible in Figure 19 panel (a) than in Figure 26 panel (b), which shows the power of interactive cleaning.

Instead of looking at the observable differences, the differences in measurements should be discussed as well. Table 14 lists some properties of the images I produced compared to the images produced by S. M. Andrews, Huang, et al. 2018.

Name	Elias24 (DSHARP)	Elias24 (reproduce DSHARP)	Elias24 (this work, Final)	AS209 (DSHARP)	AS209 (reproduce DSHARP)	AS209 (this work, Final)
ν (GHz)	231.9	239.7	239.7	239.0	239.8	239.8
θ_b, PA_b (mas, $^\circ$)	$37 \times 34, 82$	$57 \times 38, 85$	$72 \times 38, 88$	$38 \times 36, 68$	$80 \times 38, 83$	$99 \times 42, 86$
Rms Noise (μ Jy/beam)	19	31	49	19	30	23
Peak in- tensity (mJy/beam)	4.63	5.80	7.05	1.83	3.00	3.62
Flux density (mJy)	352	232	405	288	138	213
robust	0.0	0.0	-	- 0.5	-0.5	0.5
θ_{tap}, PA_{tap} (mas, $^\circ$)	$35 \times 10, 166$	$35 \times 10, 166$	-	$37 \times 10, 162$	$37 \times 10, 162$	-
SNR	244	187	143	96	100	157

Table 14: Properties of continuum images by DSHARP and this work. Columns are: Elias24 from S. M. Andrews, Huang, et al. 2018; Elias24 from Figure 26 (b); Elias24 from Figure 23 (b) (originally 19 (a)); AS209 from S. M. Andrews, Huang, et al. 2018; AS209 from Figure 26 (a); AS209 from Figure 23 (a) (originally from Figure 35 (a)). Rows are as follows: ν central frequency; θ_b Beam size and PA_b position angle of beam; rms noise level; peak intensity of the continuum; integrated flux over the disk; Robust parameter, if Briggs weighting is used (otherwise -); $\theta_{tap} PA_{tap}$ tapering parameters, if tapering is used; SNR Signal-to-noise ratio.

Table 14 shows properties of images I produced compared with the images produced by S. M. Andrews, Huang, et al. 2018. The column 'Elias 24 (reproduce DSHARP)' is produced with almost the same settings as the image produced in S. M. Andrews, Huang, et al. 2018, with the only difference being that I did not only use spectral window 0 therefore my central frequency differs from theirs. Their rms is 39% lower compared to my image and their peak is 20% lower, making their signal to noise ratio 30% higher than the signal to noise ratio I got when using their settings. These differences are likely caused by their self-calibration and the flagging of baselines.

The column 'Elias 24 (this work, Final)' is produced with interactive cleaning (exact settings

can be found in Table 13), which made the structure best visible for communication purposes. The table shows that the peak intensity (52% higher than image produced by S. M. Andrews, Huang, et al. 2018) and the integrated flux (15% higher than image produced by S. M. Andrews, Huang, et al. 2018) are higher than in the other two images of Elias 24, but the rms noise level is also higher (1.5 times the rms of the image produced by S. M. Andrews, Huang, et al. 2018), resulting in a lower signal to noise ratio. These differences compared to the image produced by S. M. Andrews, Huang, et al. 2018 are likely also caused by their self-calibration and the flagging of baselines, but as the image produced with interactive cleaning still shows the structures clearly and takes less time and expertise, it is not necessary to take these extra steps and aim for the highest signal to noise ratio when producing an image to convey a story.

Even though the signal to noise ratio is lower than the image reproducing the DSHARP settings, the final Elias24 image does show the structures better, which makes it more useful for communication with the public and shows that the image with the highest signal to noise ratio does not always mean the best image for outreach purposes.

The same comparison can be done for the images of AS209. The rms of the image produced by S. M. Andrews, Huang, et al. 2018 is lower by 37% and their peak intensity is lower by 39 %, making their signal to noise ratio slightly lower than the signal to noise ratio I got when using their settings. These differences are likely caused by their self-calibration.

The rms noise of the image produced by S. M. Andrews, Huang, et al. 2018 is only 17% lower while the peak intensity is 49% lower compared to 'AS209 (this work, Final)', which makes the signal to noise ratio 64% higher compared to the image produced by S. M. Andrews, Huang, et al. 2018. This shows that doing self-calibration does not always result in the best signal to noise ratio.

S. M. Andrews, Huang, et al. 2018 produced a brightness profile of AS209, which can be compared to the profile I produced of my own image.

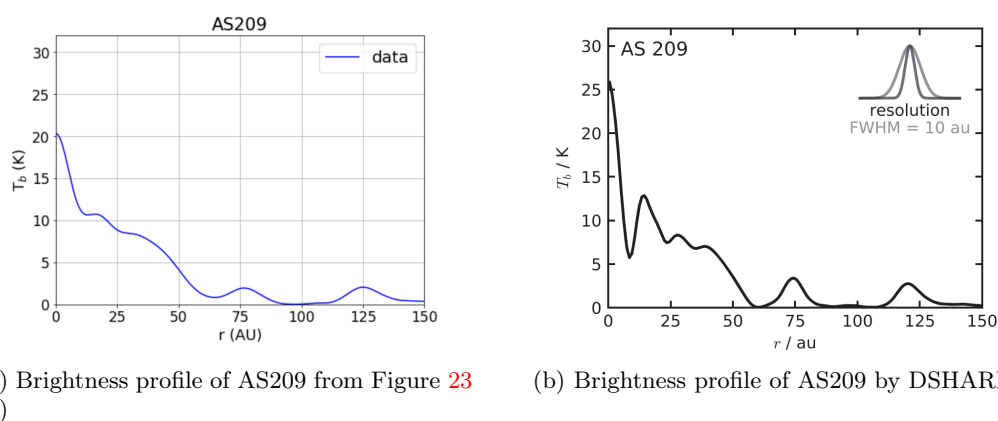


Figure 29: Comparison Brightness profile of AS209

When comparing the graphs shown in Figure 29, it can be seen that the peak brightness temperature peak of the graph produced by S. M. Andrews, Huang, et al. 2018 is higher and it shows more intensity peaks between 10 and 50 AU. These differences can be due to the

fact that S. M. Andrews, Huang, et al. 2018 used self-calibration, which could make the cleaning process more precise resulting in more visible structures. The peak brightness temperature could also be slightly different due to the conversion from Jy/beam to K which uses the beam size, the central frequency and the intensity profile.

However the main goal of this graph is to show the dips in intensity, which points to the existence of gaps, and the peaks in intensity, which points to the existence of rings. These main structures are still clearly visible in the brightness profile of the continuum map made for outreach purposes.

8.3 Final images

For the moment 1 and 0 map the colors that are used are important, they should be aesthetically pleasing and convey the purpose of the image. As the image shows the kinematics based on Doppler shifts the colors red and blue were chosen. For the general public, these colors are not immediately clear as they might also represent hot and cold, so a detailed explanation should be added, preferably with an animation of the Doppler shift effect. The way I defined the used color scheme makes the red-white-blue gradient also appropriate for color blind visitors (Figure 22) and thus improves accessibility.

The size of our solar system was added to the image with a green line, to give the audience a scale which helps them comprehend the image. The axis are also in astronomical units, counting from the central point of the object where the relative velocity is zero, to give more perspective. These final moment maps are shown in Figure 21.

The final continuum images are shown in Figure 23 and the arguments used in the cleaning process are stated in Table 13. Because the best image was produced using interactive cleaning, it is difficult to get the exact same result. Therefore the settings of AS209 given in Table 13 can also be used for Elias 24 to get a clear image without having to perform interactive cleaning.

For the continuum map, the colors are of great importance as well. The non-experts in Smith et al. 2015, specified that they prefer a red/orange color scheme for both aesthetics and conveying the story. On the other hand, the colors should be chosen so that the contrast of the structures is clearly visible, also for colorblind people so I created my own color palette that show the structures for colorblind people as well. Finally I set the bar scale starting at 0, letting most of the noise disappear, making the background darker and the structures more visible.

Figure 23 shows the final images, whereas Figure 24 shows the images as they might look for colorblind people, since this is something to keep in mind when producing images for a greater public as more than 8 % of the population is color blind. It can be seen that with the chosen color scheme the features are still visible.

In addition to the custom color scheme, the size of our solar system was added to the image with a white ellipse, to give the audience a scale which helps in comprehending the image. The axis are also in astronomical units, counting from the central point of the object to give more perspective. Finally the beam size is also added in the left corner to make the radio image complete.

HR8799

To complete the story it would be great to have the sub-mm continuum of HR8799, as it shows a band of dust outside the four orbiting planets, which thus shows most dust is cleared out by the orbiting planets inside this dust ring. This has not yet been imaged at high angular resolution, which made me neglect it for now, but in the future, it would be beneficial to image the continuum of this source as well to complete the story.

9 Conclusions

To explain planet formation to the public, at least four stages should be shown. The first stage is a molecular cloud, where the stars are born due to a gravitational collapse in dense regions. The second stage is the rotating gas, which means that, due the conservation of angular momentum, a disk is forming. This stage can be visualized using a moment 1 map of a Class 0 or I protostar. The third stage that needs to be shown are the structured disks of Class II or Class III protostars that show signs of planet formation. For this stage a continuum image of dust emission, ideally containing clear gaps or other substructures, should be used. Finally, a planetary system should be shown in which most of the dust has been accreted to planets and the gas has dissipated away.

To explain these stages of planet formation a planetarium can be used. A planetarium is a useful medium to communicate astronomy, as a full dome planetarium show results in greater attention, reduces cognitive loads, and thus leads to greater learning. By using a relatively easy way of showing new data, namely by zooming into the new graphs and images from patches in the night sky, the boundary to overcome in producing a new planetarium show is reduced. The show can be complemented with older full dome content, as the planetarium already contains lots of informative clips and tools to show the basic astronomy concepts.

In this thesis, I have produced guidelines for communicating science, specifically for communicating astronomy. A red coloration is preferred to convey the story and together with orange found to be most pleasing for the viewers. The colors, the observation method and the history of the object should be explained, and the location and scale should be shown. Finally, storytelling techniques should be used to make the talk more memorable.

The moment maps are produced using *immoments* and are used to show the rotation of the disk where $C^{17}O$ traces the disk the best. The argument *includepix* determines what intensity is included and should be set to approximately 3σ but should be altered based on amount of noise in the output images.

To produce continuum images, the command *tclean* is used with the newest version of CASA. The *tclean* command has many different arguments that influence the cleaning process. Although I did not test every parameter combination, I did look at some of the settings that can be used when making a continuum and compared the results both visually and numerically.

When making a continuum it is advised that the amplitude should be observed for each channel, using *plotms* and if it shows lines that they should be excluded. However, the data sets I used for continuum imaging only contained weak lines and slight unevenness, which did not obviously influence the image. So, it is important to look for lines to be sure no strong lines are imaged, but I found that for communication purposes weak lines (1.67 times the continuum amplitude) can be neglected. When a measurement set has more than one useful spectral window the user can choose to image all of them or just one, as the result does not give a big difference, but imaging multiple spectral windows together does reduce the background noise slightly resulting in a higher signal-to-noise ratio, thereby improving the appearance of the image.

If an image is used for measurements the primary beam correction should be done before any measurements are made, but for outreach purposes, the primary beam correction should be skipped as it makes the structures less visible and changes the intensity, making the entire image

less pleasing, which is important when presenting to the public.

The deconvolver argument changes the minor cycle of the cleaning procedure, the measurements show that the beam size, rms noise, peak intensity and integrated flux is the same for both deconvolver settings and the appearance does not seem to change. So, the deconvolver settings can be neglected when imaging for outreach purposes.

One important argument is the weighting which can be set to natural, uniform or a compromise between the two with Briggs weighting, which has a robust parameter to set the weighting towards uniform or natural. I have imaged most of the weighting possibilities for three different continuum images and concluded that the natural weighting has a higher peak intensity and flux density making the structures brighter. Natural weighting has a lower angular resolution, also confirmed by the larger beam size, and thus the structures are less well defined. The uniform weighting has a very grainy appearance making the structure blend in with the background which is caused by a low peak intensity, a low flux density, and a higher RMS noise resulting in a low signal-to-noise ratio. The best option for communication purposes is therefore the Briggs weighting with robust parameter 0.5 which has the highest signal-to-noise ratio and shows the structure the best compared to other weightings schemes using automatic masking. If desired the robust parameter can be altered to look for a better result.

If there is indeed time or interest in more detailed imaging, I recommend interactive cleaning, where a new mask can be defined by the user for every cycle. Interactive cleaning has turned out to be very useful as imaging artifacts can be excluded and faint structures might be identified better by the user themselves. Using interactive cleaning showed that the image that shows the structures the best and is used for outreach purposes is not always the image that is best for research purposes, as it is not always the image with the highest signal to noise ratio. S. M. Andrews, Huang, et al. 2018 used self-calibration and flagged certain baselines to produce their continuum images which requires time and expertise. Comparing my final images to theirs concludes that this is not necessary to undergo these steps when imaging for outreach purposes as the goal is to show the structures which are clearly visible in the continuum image and the brightness profile.

In short moment maps that are used to map the disk, are best for Class I sources using CO isotopologues and an *includepix* of approximately 3σ . An appropriate color map goes from red to white to blue and should be checked for colorblindness. And continuum maps should be made using as many line-free channels as possible, Briggs weighting with robust of 0.5, the default deconvolver, no primary beam correction and interactive cleaning (if possible). An appropriate color map includes red and orange and should be checked for colorblindness.

The resulting products of this thesis are: (1) a set up for a planetarium show on planet and star formation based on both astronomical as communication research; (2) four images showing two different stages of planet formation with settings based on experimental imaging and formatted correctly for outreach purposes; and (3) a set of detailed instructions for non-experts on imaging moment maps and continuum images from ALMA archival data including the CASA script for imaging and SkySkan scripts for integrating the images into the planetarium.

This work will lead to the improvement in the public understanding of planet formation and simplified imaging of ALMA data for outreach purposes. As ALMA data is used in other

subfields in astronomy, this work can be extended to different subfields with scientific input of other astronomers. And in the future, the same research could be done to broaden the types of observations and telescopes that can be brought to the public.

Acknowledgement

I would like to thank the people that have supported me during this research. First of all I want to thank Jake Noel-Storr, who made this research possible as we came up with the subject together and helped to shape this research. I especially want to thank Veronica Allen, my second supervisor, as she gave me the motivation for this project to begin with but also kept me motivated with constructive feedback. Whenever I encountered a problem I could go to Veronica for help and seek for a solution together, very grateful for her help. I also want to thank Inga Kamp and Floris van der Tak for their help during the brainstorm period of my storyboard. Next I would like to thank my boyfriend Sean Walsh for making this period way less stressful. Next I would like to thank my room mates for the support during this process and especially Sarah Arentsen, who always provides a sympathetic ear or I can go to to blow off some steam. And finally I want to thank Evan van der Voort for the help with my foolish questions, discussions and the lunch breaks in the sun.

References

- 't Hof, Merel Lydia Roselinda van (Oct. 2019). “Chemistry in embedded disks: setting the stage for planet formation”. PhD thesis, pp. 4–43.
- ALMA (2021). *About ALMA, at first glance | ALMA*. About ALMA. URL: <https://www.almaobservatory.org/en/about-alma/> (visited on 06/12/2022).
- ALMA Science Archive* (2022). [almascience.nrao.edu](https://almascience.nrao.edu/aq/?result_view=observation). URL: https://almascience.nrao.edu/aq/?result_view=observation (visited on 05/19/2022).
- Alt, Michael B and KM Shaw (1984). “Characteristics of ideal museum exhibits”. In: *British Journal of Psychology* 75.1, pp. 25–36.
- André, Ph et al. (2010). “From filamentary clouds to prestellar cores to the stellar IMF: Initial highlights from the Herschel Gould Belt Survey”. In: *Astronomy & Astrophysics* 518, p. L102.
- Andrews, Sean M (2020). “Observations of protoplanetary disk structures”. In: *Annual Review of Astronomy and Astrophysics* 58, pp. 483–528.
- Andrews, Sean M, Jane Huang, et al. (2018). “The disk substructures at high angular resolution project (DSHARP). I. Motivation, sample, calibration, and overview”. In: *The Astrophysical Journal Letters* 869.2, p. L41.
- Andrews, Sean M, David J Wilner, et al. (2011). “Resolved images of large cavities in protoplanetary transition disks”. In: *The Astrophysical Journal* 732.1, p. 42.
- Arcand, K et al. (2010). “Surveying Aesthetics & Astronomy: A project exploring the public’s perception of astronomical images and the science within”. In: *Communicating Astronomy with the Public Journal* 10, pp. 13–16.
- Arcand, Kimberly K et al. (2013). “Processing color in astronomical imagery”. In: *arXiv preprint arXiv:1308.5237*.
- Arce, Héctor G and Anneila I Sargent (2006). “The evolution of outflow-envelope interactions in low-mass protostars”. In: *The Astrophysical Journal* 646.2, p. 1070.
- Armitage, Philip J (2020). *Astrophysics of planet formation*. Second edition. Cambridge University Press, pp. 49–53.
- Aso, Yusuke et al. (2015). “ALMA observations of the transition from infall motion to Keplerian rotation around the late-phase protostar TMC-1A”. In: *The Astrophysical Journal* 812.1, p. 27.
- Bae, Jaehan and Zhaohuan Zhu (2018). “Planet-driven Spiral Arms in Protoplanetary Disks. I. Formation Mechanism”. In: *The Astrophysical Journal* 859.2, p. 118.
- Bemis, Ashley (Nov. 2021). *“Imaging ALMA Data”*. Youtube video. URL: <https://www.youtube.com/watch?v=yuLKAfroHu4&t=4s> (visited on 06/03/2022).
- Bitsch, Bertram, Michiel Lambrechts, and Anders Johansen (2015). “The growth of planets by pebble accretion in evolving protoplanetary discs”. In: *Astronomy & Astrophysics* 582, A112.
- Boss, Alan P (2000). “Possible rapid gas giant planet formation in the solar nebula and other protoplanetary disks”. In: *The Astrophysical Journal* 536.2, p. L101.
- Brogan, CL et al. (2015). “The 2014 ALMA long baseline campaign: first results from high angular resolution observations toward the HL Tau region”. In: *The Astrophysical journal letters* 808.1, p. L3.
- Catalog of Circumstellar Disks* (2022). www.circumstellardisks.org. URL: <https://www.circumstellardisks.org/index.php> (visited on 06/18/2022).
- Chen, H et al. (1995). “Bolometric temperature and young stars in the Taurus and Ophiuchus complexes”. In: *The Astrophysical Journal* 445, pp. 377–392.
- Christensen, Lars Lindberg (2007). *The hands-on guide for science communicators: A step-by-step approach to public outreach*. Springer Science & Business Media.

- Christensen, Lars Lindberg et al. (2016). “Data to Dome”. In: Cornwell, Tim J (2008). “Multiscale CLEAN deconvolution of radio synthesis images”. In: *IEEE Journal of selected topics in signal processing* 2.5, pp. 793–801.
- Cortes, P. C. et al. (Mar. 2022). *ALMA Technical Handbook*. ALMA Doc. 9.3. Vol. ver. 1.0. ALMA, p. 17.
- Cosmos (n.d.). *Emission Line | COSMOS*. astronomy.swin.edu.au. URL: <https://astronomy.swin.edu.au/cosmos/e/emission+line>.
- Dipierro, G et al. (2018). “Rings and gaps in the disc around Elias 24 revealed by ALMA”. In: *Monthly Notices of the Royal Astronomical Society* 475.4, pp. 5296–5312.
- Ercolano, Barbara and Ilaria Pascucci (2017). “The dispersal of planet-forming discs: theory confronts observations”. In: *Royal Society Open Science* 4.4, p. 170114.
- ESO (n.d.). *ESA/Hubble Space Telescope*. esahubble.org. URL: <https://esahubble.org/>.
- Fasoglio, Daniela and Dirk Tuin (Jan. 2018). *Speaking skill levels of English attained in Dutch secondary education*.
- Fedele, D et al. (2018). “ALMA continuum observations of the protoplanetary disk AS 209—Evidence of multiple gaps opened by a single planet”. In: *Astronomy & Astrophysics* 610, A24.
- Groningen, Rijksuniversiteit (2020, 2021). *Key figures*. University of Groningen. URL: <https://www.rug.nl/about-ug/profile/facts-and-figures/?lang=en>.
- Heinemann, T and JCB Papaloizou (2009). “The excitation of spiral density waves through turbulent fluctuations in accretion discs—II. Numerical simulations with MRI-driven turbulence”. In: *Monthly Notices of the Royal Astronomical Society* 397.1, pp. 64–74.
- Hiramatsu, Masaaki and Stella G Amano (2021). “Virtual ALMA Tour in VRChat: A Whole New Experience”. In: *Communicating Astronomy with the Public Journal* 30, p. 18.
- Hoek, Carmen (2022). *English planetarium shows at DOT*.
- Johansen, Anders, Andrew Youdin, and Hubert Klahr (2009). “Zonal flows and long-lived axisymmetric pressure bumps in magnetorotational turbulence”. In: *The Astrophysical Journal* 697.2, p. 1269.
- Jørgensen, Jes K et al. (2009). “PROSAC: a submillimeter array survey of low-mass protostars—II. The mass evolution of envelopes, disks, and stars from the Class 0 through I stages”. In: *Astronomy & Astrophysics* 507.2, pp. 861–879.
- Kraus, Stefan et al. (2017). “Dust-trapping vortices and a potentially planet-triggered spiral wake in the pre-transitional disk of v1247 orionis”. In: *The Astrophysical Journal Letters* 848.1, p. L11.
- Lada, Charles J and BA Wilking (1984). “The nature of the embedded population in the Rho Ophiuchi dark cloud—Mid-infrared observations”. In: *The Astrophysical Journal* 287, pp. 610–621.
- Larson, Richard B (1969). “Numerical calculations of the dynamics of a collapsing proto-star”. In: *Monthly Notices of the Royal Astronomical Society* 145.3, pp. 271–295.
- Marel, Nienke van der, Jonathan P Williams, and Simon Bruderer (2018). “Rings and gaps in protoplanetary disks: planets or snowlines?” In: *The Astrophysical Journal Letters* 867.1, p. L14.
- Marois, Christian, Bruce Macintosh, et al. (2008). “Direct imaging of multiple planets orbiting the star HR 8799”. In: *science* 322.5906, pp. 1348–1352.
- Marois, Christian, B Zuckerman, et al. (2010). “Images of a fourth planet orbiting HR 8799”. In: *Nature* 468.7327, pp. 1080–1083.

- Martinez-Conde, Susana et al. (2019). “The storytelling brain: how neuroscience stories help bridge the gap between research and society”. In: *Journal of Neuroscience* 39.42, pp. 8285–8290.
- Maury, AJ et al. (2019). “Characterizing young protostellar disks with the CALYPSO IRAM-PdBI survey: large Class 0 disks are rare”. In: *Astronomy & Astrophysics* 621, A76.
- Monnier, John D et al. (2019). “Multiple spiral arms in the disk around intermediate-mass binary HD 34700A”. In: *The Astrophysical Journal* 872.2, p. 122.
- Murillo, Nadia M et al. (2013). “A Keplerian disk around a Class 0 source: ALMA observations of VLA1623A”. In: *Astronomy & Astrophysics* 560, A103.
- Myers, PC and EF Ladd (1993). “Bolometric temperatures of young stellar objects”. In: *The Astrophysical Journal* 413, pp. L47–L50.
- NASA (Jan. 2006). *Hubble’s Sharpest View of the Orion Nebula*. HubbleSite.org. URL: <https://hubblesite.org/contents/media/images/2006/01/1826-Image.html>.
- (n.d.). *National Aeronautics and Space Administration*. NASA. URL: <https://www.nasa.gov/>.
- NRAO (2016). *image.moments - Function*. Casa Toolkit Reference Manual. URL: <https://casa.nrao.edu/docs/casaref/image.moments.html> (visited on 05/19/2022).
- (Release 6.5). *Common Astronomy Software Applications, CASA*. casa.nrao.edu. URL: <https://casa.nrao.edu/> (visited on 05/19/2022).
- (2022). *Description*. CASA Documentation. URL: https://casa.nrao.edu/casadocs/casa-5.6.0/global-task-list/task_tclean/about (visited on 06/06/2022).
- (n.d.). *tclean*. casa.nrao.edu. URL: <https://casa.nrao.edu/docs/taskref/tclean-task.html>.
- Observatory, W. M. Keck (Nov. 2018). *Exoplanet Stepping Stones – W. M. Keck Observatory*. Exoplanet Stepping Stones. URL: <https://keckobservatory.org/hr8799c/> (visited on 07/08/2022).
- Pérez, Laura M et al. (2016). “Spiral density waves in a young protoplanetary disk”. In: *Science* 353.6307, pp. 1519–1521.
- Pinilla, P et al. (2017). “Dust density distribution and imaging analysis of different ice lines in protoplanetary disks”. In: *The Astrophysical Journal* 845.1, p. 68.
- Robitaille, Thomas P et al. (2006). “Interpreting spectral energy distributions from young stellar objects. I. A grid of 200,000 YSO model SEDs”. In: *The Astrophysical Journal Supplement Series* 167.2, p. 256.
- Rosotti, Giovanni P et al. (2016). “The minimum mass of detectable planets in protoplanetary discs and the derivation of planetary masses from high-resolution observations”. In: *Monthly Notices of the Royal Astronomical Society* 459.3, pp. 2790–2805.
- Schwertly, Scott (May 2022). *The Positive Impacts of Storytelling When Giving a Presentation*. ethos3.com. URL: <https://ethos3.com/the-positive-impacts-of-storytelling-when-giving-a-presentation/> (visited on 06/21/2022).
- SIMBAD (2022). *Orion Nebula*. simbad.u-strasbg.fr. URL: <http://simbad.u-strasbg.fr/simbad/sim-id?Ident=Orion+Nebula> (visited on 06/18/2022).
- SkySkan (2022). *Home*. Sky-Skan. URL: <https://skyskan.com/> (visited on 05/19/2022).
- Smith, Lisa F et al. (2015). “Is that real? understanding astronomical images”. In: *Journal of Media and Communication Studies* 7.5, pp. 88–100.
- Space-Telescope-Science-Institute (n.d.). *Home*. STScI.edu. URL: <https://www.stsci.edu/>.
- Stahl, Stephen M and Richard L Davis (2009). “Applying the principles of adult learning to the teaching of psychopharmacology: storyboarding a presentation and the rule of small multiples”. In: *CNS spectrums* 14.6, pp. 288–294.

- Takahashi, Sanemichi Z and Takayuki Muto (2018). “Structure Formation in a Young Protoplanetary Disk by a Magnetic Disk Wind”. In: *The Astrophysical Journal* 865.2, p. 102.
- Takeuchi, Taku and DNC Lin (2002). “Radial flow of dust particles in accretion disks”. In: *The Astrophysical Journal* 581.2, p. 1344.
- Terebey, SUsAN, FRANK H Shu, and PATRICK Cassen (1984). “The collapse of the cores of slowly rotating isothermal clouds”. In: *The Astrophysical Journal* 286, pp. 529–551.
- Tobin, John J, Lee Hartmann, et al. (2012). “A 0.2-solar-mass protostar with a Keplerian disk in the very young L1527 IRS system”. In: *Nature* 492.7427, pp. 83–85.
- Tobin, John J, Patrick D Sheehan, et al. (2020). “The VLA/ALMA Nascent Disk and Multiplicity (VANDAM) Survey of Orion protostars. II. A statistical characterization of class 0 and class I protostellar disks”. In: *The Astrophysical Journal* 890.2, p. 130.
- Tychoniec, Łukasz (Mar. 2021). “Protostellar jets and planet-forming disks: Witnessing the formation of Solar System analogues with interferometry”. PhD thesis, pp. 1–15.
- Tychoniec, Łukasz, Ewine F van Dishoeck, et al. (2021). “Which molecule traces what: chemical diagnostics of protostellar sources”. In: *Astronomy & Astrophysics* 655, A65.
- Tychoniec, Łukasz, Carlo F Manara, et al. (2020). “Dust masses of young disks: constraining the initial solid reservoir for planet formation”. In: *Astronomy & Astrophysics* 640, A19.
- University, Iowa State (n.d.). *Nondestructive Evaluation NDE Engineering : Radiation Safety*. www.nde-ed.org. URL: <https://www.nde-ed.org/NDEEngineering/RadiationSafety/theory/production.xhtml>.
- Van’t Hoff, Merel LR et al. (2020). “Temperature structures of embedded disks: young disks in Taurus are warm”. In: *The Astrophysical Journal* 901.2, p. 166.
- Whitney, Barbara A et al. (2003). “Two-dimensional radiative transfer in protostellar envelopes. II. An evolutionary sequence”. In: *The Astrophysical Journal* 598.2, p. 1079.
- Wibisono, Affelia (June 2022). *Storytelling and other arts – European Citizen Science Association (ECSA)*. Storytelling and other arts. URL: <https://ecsa.citizen-science.net/working-groups/storytelling-and-other-arts/> (visited on 06/21/2022).
- Wilner, David (2005). “*Radio Astronomy and Interferometry Fundamentals*”. Youtube video. URL: <https://www.youtube.com/watch?v=0TwnZhiEc3A> (visited on 06/12/2022).
- Yen, Hsi-Wei et al. (2014). “ALMA observations of infalling flows toward the Keplerian disk around the Class I protostar L1489 IRS”. In: *The Astrophysical Journal* 793.1, p. 1.
- Yu, Ka Chun, Kamran Sahami, Grant Denn, et al. (2016). “Immersive planetarium visualizations for teaching solar system moon concepts to undergraduates”. In: *Journal of Astronomy & Earth Sciences Education (JAESE)* 3.2, pp. 93–110.
- Yu, Ka Chun, Kamran Sahami, Victoria Sahami, et al. (2015). “Using a Digital Planetarium for Teaching Seasons to Undergraduates.” In: *Journal of Astronomy & Earth Sciences Education* 2.1, pp. 33–50.
- Zhu, Zhaohuan et al. (2011). “Transitional and Pre-transitional Disks: Gap Opening by Multiple Planets?” In: *The Astrophysical Journal* 729.1, p. 47.

10 Appendix

10.1 Images

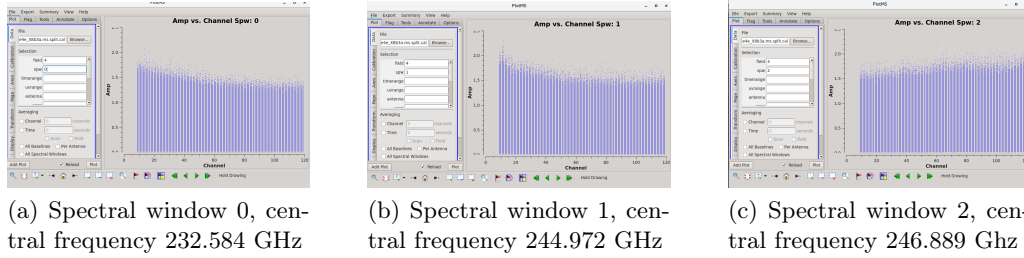


Figure 30: Signal amplitude in each channel of three spectral windows of AS209 indicated by blue points, shown in *plotms*.

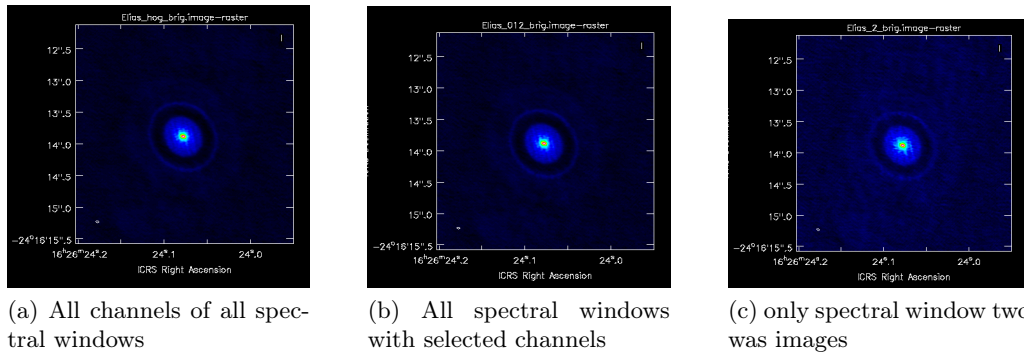


Figure 31: 140 GHz continuum (color scale) images of Elias24. Left (31a) includes all channels of all spectral windows. Middle (31b) excludes the slope channels (0-50 of spectral window 0 and 1) both have approximately beam size $0.0494'' \times 0.0287''$. Right (31c) includes all channels of spectral window 2 and has beam size $0.0476'' \times 0.0277''$.

Image	ν (GHz)	Beam size	Flux density (mJy)	Peak intensity (mJy/beam)	Rms Noise (μ Jy/beam)	SNR
(1)	(2)	(3)	(4)	(5)	(6)	(7)
31a	239,7	$0.0494'' \times 0.0287''$	216	4,41	29	154
31b	239,8	$0.0494'' \times 0.0287''$	222	4,40	32	138
31c	246,9	$0.0476'' \times 0.0277''$	261	4,49	53	84,2

Table 15: Properties of Figure 31, which shows the effect of difference of channel selection. Columns as in Table 8

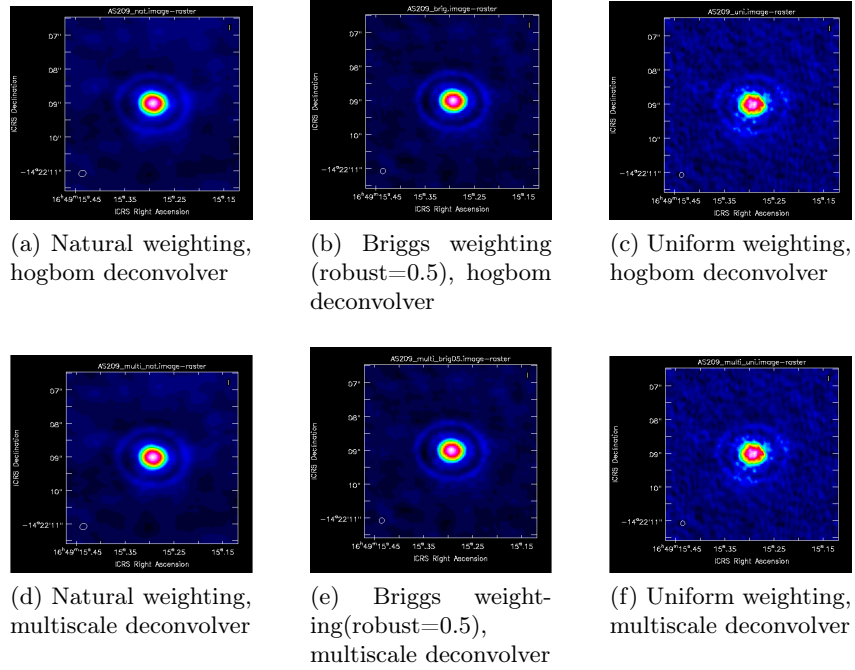


Figure 32: 230 GHz continuum (color scale) images of AS209. The left images (32a & 32d) are produced with natural weighing and have beam size $0.2184'' \times 0.1827''$. The middle images (32b & 32e) are produced with Briggs weighting with robust parameter 0.5 and have beam size $0.1680'' \times 0.1566''$. The right images (32c & 32f) are produced with uniform weighing and have beam size $0.1511'' \times 0.1243''$. Images in the upper row (32a & 32b & 32c) are produced with the hogbom deconvolver. Images in the lower row (32d & 32e & 32f) are produced with the multi-scale deconvolver.

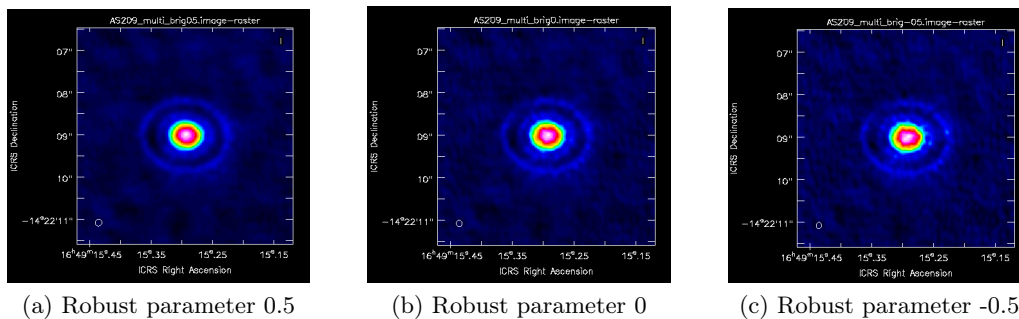


Figure 33: 230 GHz continuum (color scale) images of AS209 produced with Briggs weighting. Left (33a) robust parameter 0.5. Beam size $0.16802'' \times 0.1566''$. Middle (33b) robust parameter 0. Beam size $0.1548'' \times 0.1353''$. Right (33c) robust parameter of -0.5. Beam size $0.1520'' \times 0.1272''$

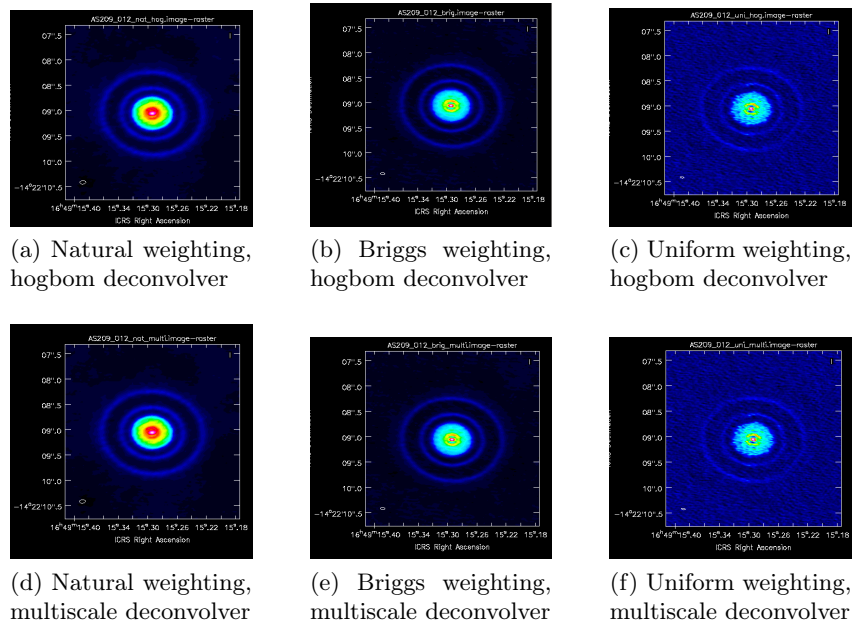


Figure 34: 240 GHz continuum (color scale) images of AS209. The left images (34a & 34d) are produced with natural weighing and have beam size $0.1191'' \times 0.0714''$. The middle images (34b & 34e) are produced with Briggs weighing with robust parameter 0.5 and have beam size $0.0992'' \times 0.0429''$. The right images (34c & 34f) are produced with uniform weighing and have beam size $0.0842'' \times 0.0278''$. Images in the upper row (34a & 34b & 34c) are produced with the hogbom deconvolver. Images in the lower row (34d & 34e & 34f) are produced with the multi-scale deconvolver.

Image	ν (GHz)	Beam size	Flux density (mJy)	Peak intensity (mJy/beam)	Rms Noise (μ Jy/beam)	SNR
(1)	(2)	(3)	(4)	(5)	(6)	(7)
34a	239.8	$0.2184'' \times 0.1827''$	236	5.56	37	149
34b	239.8	$0.1680'' \times 0.1566''$	213	3.62	23	161
34c	239.8	$0.1511'' \times 0.1243''$	154	2.36	64	37
34d	239.8	$0.2184'' \times 0.1827''$	235	5.54	36	155
34e	239.8	$0.1680'' \times 0.1566''$	213	3.63	23	161
34f	239.8	$0.1511'' \times 0.1243''$	146	2.37	64	37

Table 16: Properties of Figure 34, which shows the effect of difference weightings and deconvolver settings. Columns as in Table 8.

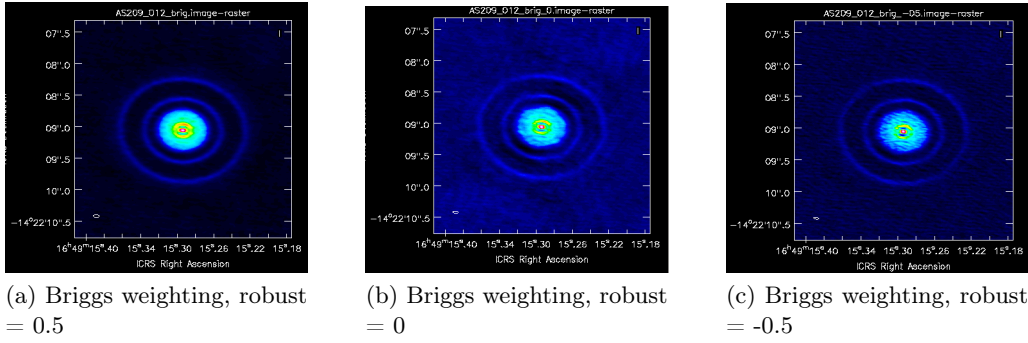


Figure 35: 240 GHz continuum (color scale) images of AS209 produced with Briggs weighting. Left (35a) robust parameter 0.5. Beam size $0.0992'' \times 0.0429''$. Middle (35b) robust parameter 0. Beam size $0.0890'' \times 0.0331''$. Right (35c) robust parameter of -0.5. Beam size $0.0860'' \times 0.0290''$

Image	ν (GHz)	Beam size	Flux density (mJy)	Peak intensity (mJy/beam)	Rms Noise (μ Jy/beam)	SNR
(1)	(2)	(3)	(4)	(5)	(6)	(7)
35a	239.8	$0.16802'' \times 0.1566''$	213	3.62	23	161
35b	239.8	$0.1548'' \times 0.1353''$	108	2.60	31	83
35c	239.8	$0.1520'' \times 0.1272''$	164	2.49	34	74

Table 17: Properties of Figure 33. Column 1: figure number. Column 2: central frequency. Column 3: synthesized beam size and position angle. Column 4: flux density of the disk. Column 5: peak intensity in the image. Column 6: averaged rms noise level of image. Column 7: signal to noise ratio.

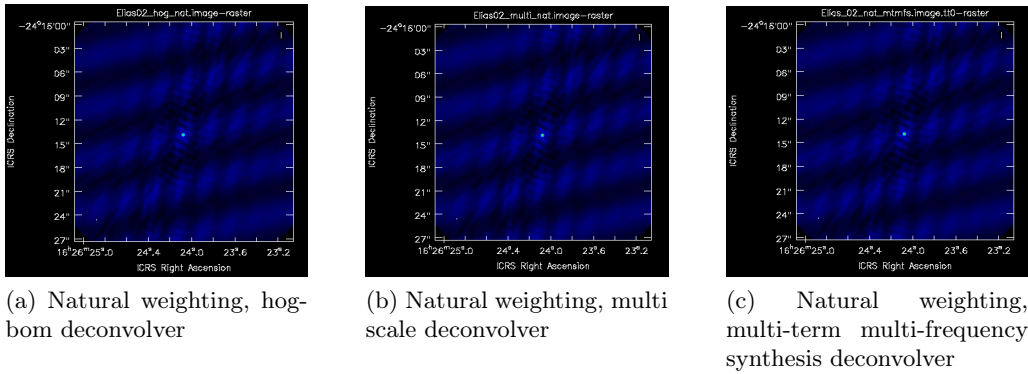


Figure 36: Non zoomed 240 GHz continuum (color scale) images of Elias24 natural weighting. Beam size $0.0722'' \times 0.0381''$. Left (36a) is produced using the hogbom deconvolver. Middle (36b) is produced using the multi-scale deconvolver. Right (36c) is produced using the multi-term multi-frequency synthesis deconvolver.

10.2 Instruction data reduction

The next few pages show the instructions for data reduction and imaging of a moment map and a continuum image in pdf format.

How to make moment maps and continuum out of ALMA data?

Contents:

Introduction

Step 1 – Downloading

Step 2 – Calibration

Step 3 – Inspecting the data

Step 4 – Preparing the data

Step 5 – Cleaning the MS

Step 6 – Moment map

Step 7 – Observe the produced images

Introduction

In the following instructions the steps that need to be taken to produce a continuum image or a moment map are specified. A continuum image shows the dust emission of a source, and the moment maps show the intensity, extend and kinematics of the gas.

These instructions are intended to be used for data downloaded from the ALMA archive (<https://almascience.nrao.edu/aq/>). For analyzing the data initially, CARTA (the Cube Analysis and Rendering Tool for Astronomy) can be used, which can be opened from the archive. The calibration and imaging in these instructions is done with CASA (the Common Astronomy Software Applications). The data reduction is all done in the command line of the terminal, the commands will be shown in *italic*. A script with the exact commands is added as well.

The version of CASA needed to calibrate the data is specified in the README files in the ALMA archive and can be downloaded here:

<https://almascience.nrao.edu/processing/science-pipeline> .

Step 1— Downloading

Download the data that is needed for your imaging. First the right data should be searched for using for example the right location on the sky, the source name, or a project code. When the source is found, there are many ways to select the right data, looking at the publications, angular resolution etc. If the right data set is found, click the check box of the data needed and click the arrow in the right top corner to explore and download your data.

Project code	ALMA source name	RA	Dec	Band	Conf. sens.	Frequency support	Release date	Publications	Ang. res.	Min. vel. res.	Array	Mosaic	Max. reso. scale	FOV	Scientific category	Science keyword	Int. Time	Gal. lon.	Gal. lat.
2015.1.00078.S	AS_209	16:49:15.294	-14:22:09.010	7	0.0508	276.08..290.74GHz	2018-01-09	9	0.204	0.151	12m	5.023	20.522	Disks and planet format...	Disks around low-mass ...	3602.539	4.838	18.966	
2015.1.00486.S	AS_209	16:49:15.294	-14:22:09.016	6	0.0415	216.08..232.96GHz	2018-02-01	12	0.172	0.159	12m	3.914	25.934	Disks and planet format...	Disks around low-mass ...	4717.358	4.838	18.966	
2016.1.00484.L	AS_209	16:49:15.293	-14:22:09.038	6	0.0160	230.07..247.89GHz	2016-10-16	28	0.033	0.034	12m	1.208	24.367	Disks and planet format...	Disks around low-mass ...	4136.000	4.838	18.966	
2021.1.00092.S	AS_209	16:49:15.292	-14:22:09.173	7	0.0414	288.56..304.32GHz	In progress	0	0.327	0.140	12m	4.280	19.645	Disks and planet format...	Disks around low-mass ...	4112.109	4.837	18.966	
2021.1.00092.S	AS_209	16:49:15.293	-14:22:09.171	7	0.0278	288.56..304.32GHz	In progress	0	0.898	0.140	12m	8.921	19.643	Disks and planet format...	Disks around low-mass ...	1391.040	4.837	18.966	
2016.1.00484.L	AS_209	16:49:15.294	-14:22:09.030	6	0.0349	230.07..247.89GHz	2016-05-26	28	0.254	0.034	12m	3.188	24.366	Disks and planet format...	Disks around low-mass ...	756.000	4.838	18.966	
2016.1.01055.L	AS_209	16:49:15.296	-14:22:09.020	6	0.0350	248.06..266.00GHz	2020-02-08	21	0.408	0.159	12m	7.098	22.655	Disks and planet format...	Disks around low-mass ...	2116.800	4.838	18.966	
2016.1.01198.S	AS_209	16:49:15.293	-14:22:09.087	3	0.0134	89.51..105.49GHz	2021-12-23	1	0.242	30.515	12m	6.095	59.744	Disks and planet format...	Disks around low-mass ...	2115.813	4.837	18.966	
2021.1.00092.S	AS_209	16:49:15.292	-14:22:09.172	7	0.0592	349.96..365.42GHz	2023-06-03	0	0.320	0.116	12m	4.534	16.279	Disks and planet format...	Disks around low-mass ...	3328.398	4.837	18.966	
2021.1.00138.S	AS_209	16:49:15.292	-14:22:09.138	7	0.0794	306.73..372.69GHz	2023-01-10	0	0.258	0.114	12m	3.388	15.966	Disks and planet format...	Disks around low-mass ...	1481.760	4.837	18.966	

Case 1: Continuum

To produce a continuum image, the raw and auxiliary data must be downloaded. The continuum images originally produced by the pipeline, can be found under the 'product' tab. They can be inspected using CARTA opened by clicking on the button with the blue logo. If the continuum is found to be useful all the raw and auxiliary data should be downloaded. The data can be downloaded by clicking on the datafile name or the boxes of the raw and auxiliary data should be checked (while all other boxes are un-checked) then 'download selected' can be used to download the data using a command line in your terminal. Note that these files are enormous (10s to 100s of GB), so make sure there is enough disk space available when downloading these files.

Case 2: Moment map

To produce a moment map, a data cube is needed.

2a. For data from cycle 1 and up (from 2012-now), a cube can be downloaded immediately. First the cube that you want to make a moment map of should be selected, as many cubes produced from different spectral windows are available. All the cubes can be found under the 'product' tab.

To inspect the cube before downloading, the cube can be opened in CARTA, by clicking the button with the blue logo. To analyze the cube, the layout setting underneath the 'view' tab needs to be set to 'Cube Analysis'. To scroll through the cube the scroll bar for channels can be used. This is used to look for a peak in intensity, that can be mapped.

A useful cube can be downloaded in two ways; the filename can be clicked to download the cube immediately, or the box can be checked (all other boxes should be unchecked) then 'download selected' can be used to download the data using a command line in your terminal.

2b. Extra: For data from cycle 0 (2011), all files available should be downloaded. These files need to be extracted in your directory. The data should first be calibrated.

Step 2 – Calibration

This step needs to be done for case 1 (and case 2b):

A terminal needs to be opened in the 'script directory' and the 'scriptForPI' needs to be executed using: `execfile('scriptForPI.py')` which will produce a calibrated MS directory. Some calibrated MS's from after Cycle 5 are directly available on <https://data.nrao.edu/portal/>

The command for calibrating data can be found in step 1 (calibration) of the instruction:

```
##### STEP 1: Calibration #####
## Reducing data, making an MS file

# Download auxiliary and raw data from ALMA archive
# Untar or extract the files
# Open the right version of CASA
# Execute the script for PI in the 'script' directory
execfile('scriptForPI.py')
```

Step 3 – Inspecting the data**Case 1:**

First the data should be inspected. To get the properties of the MS, the command: `listobs(vis='name ms file')` can be used. Information on observation time, the fields, spectral windows, the sources and the antennas will be listed in the logger. Here the field which specifies the object and spectral windows that are useful should be denoted, as they are useful later in the process of imaging.

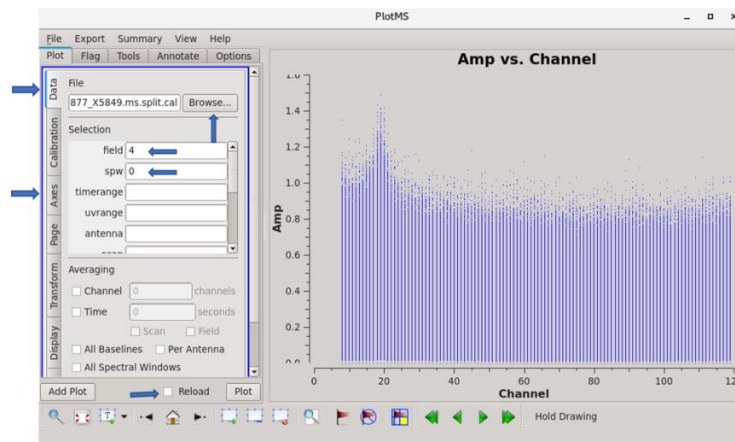
To visually inspect the visibilities, the command 'plotms' can be used.

All arguments of the plotter can be found typing the command: **inp plotms** :

```
# plotms -- A plotter/interactive flagger for visibility data.
vis = '' # Input MS or CalTable (blank for none)
gridrows = 1 # Number of subplot rows
gridcols = 1 # Number of subplot columns
rowindex = 0 # Row location of the plot (0-based)
colindex = 0 # Column location of the plot (0-based)
plotindex = 0 # Index to address a subplot (0-based)
xaxis = '' # Plot x-axis (blank for default/current)
yaxis = '' # Plot y-axis (blank for default/current)
yaxislocation = '' # Location of the y-axis (blank for default: left)
selectdata = True # Enable data selection parameters
  field = '' # Field names or ids (blank for all)
  spw = '' # Spectral windows:channels (blank for all)
  timerange = '' # Time range (blank for all)
  uvrange = '' # UV range (blank for all)
  antenna = '' # Baseline/antenna names or ids (blank for all)
  scan = '' # Scan numbers (blank for all)
  correlation = '' # Correlations/polarizations (blank for all)
  array = '' # (Sub)array numbers (blank for all)
  observation = '' # Observation IDs (blank for all)
  intent = '' # Observing intent (blank for all)
  feed = '' # Feed numbers (blank for all)
  msselect = '' # MSSelection TaQL string (blank for none)
averagedata = True # Enable data averaging parameters
  avchannel = '' # Average over channel (blank = False, otherwise value in channels)
  avtime = '' # Average over time (blank = False, otherwise value in seconds)
  avscan = False # Average over scans. Only valid with time averaging
  avfield = False # Average over fields. Only valid with time averaging
  avgbaseline = False # Average over all baselines (mutually exclusive with avgantenna)
  avgantenna = False # Average per antenna (mutually exclusive with avgbaseline)
  avgspw = False # Average over all spectral windows
  scalar = False # Scalar averaging (False=vector averaging)
transform = True # Enable data transformations
  freqframe = '' # The frame in which to render frequency and velocity axes
  restfreq = '' # Rest frequency to use for velocity conversions
  veldef = 'RADIO' # The definition in which to render velocity
  shift = [0.0, 0.0] # Adjust phases by this approximate phase center shift [dx,dy] (arcsec)
extendflag = False # Extend flagging to other data points not plotted
iteraxis = '' # The axis over which to iterate
customsymbol = [] # Enable custom symbol(s) for unflagged points
coloraxis = '' # Selects data axis for coloring
customflaggedsymbol = False # Enable custom symbol(s) for flagged points
xconnector = '' # Set connector for data points (blank="none"; "line","step")
plotrange = [] # Plot axes ranges: [xmin, xmax, ymin, ymax]
title = '' # Title at top of plot
titlefont = 0 # Font size for plot title
xlabel = '' # Text for horizontal x-axis. Blank for default.
xaxisfont = 0 # Font size for x-axis label
ylabel = '' # Text for vertical y-axis. Blank for default.
yaxisfont = 0 # Font size for y-axis label
showmajorgrid = False # Show major grid lines
showminorgrid = False # Show minor grid lines
showlegend = False # Show a legend on the plot.
  legendposition = '' # Legend position, default upperRight.
plotfile = '' # Name of plot file to save automatically
showgui = True # Show GUI
clearplots = True # Remove any existing plots so new ones can replace them.
callib = [] # Calibration library string or filename for on-the-fly calibration.
headeritems = '' # Comma-separated list of pre-defined page header items.
showatm = False # Compute and overlay the atmospheric transmission curve
showsky = False # Compute and overlay the sky temperature curve
showimage = False # Compute and overlay the image sideband curve
```

The default x- and y- axis are time and amplitude respectively. For imaging purposes it's useful to plot amplitude on the y- axis and channel on the x-axis. The correct field and spectral window should be specified in the command. If there are multiple useful spectral windows, iteration can be done over spectral windows. In the plot Gui that pops up, switches can be made between the different spectral windows the green arrows in the bottom.

After calling plotms the gui will appear. On the left side there are multiple tabs in which all parameters can be changed. Under the 'data' tab the specified file, field and spectral window can be altered, whereas under the axis tab the x and y axis can be changed. Plotting the new conditions can be done with the button 'plot' on the bottom, make sure that the reload box is checked. The data could also be averaged over time or channel to save some time, but information on the data will be removed. More information on the command plotms and the plotms gui can be found at: <https://casa.nrao.edu/casadocs/casa-5-1.2/data-examination-and-editing/using-plotms-to-plot-and-edit-visibilitys-and-calibration-tables>



For inspecting the data, the commands can be found in step 2 (inspection) of the script:

```
##### STEP 2 : Inspection #####
# List the properties of the MS file
listobs( vis = '<Your ms file>' )

# Show the input arguments of plotms
inp plotms

# Plot the visibilities for the right field and spectral window
# If more than 1 spw is useful, iterate over spectral windows
plotms( vis = '<Your ms file>',
        xaxis = 'channels',
        yaxis = 'amplitude',
        field = '<Your appropriate field>',
        spw = '<chosen spectral window>' OR iteraxis = 'spw' )
```

Step 4 – Preparing the data

Case 1: Continuum

To clean the calibrated MS file and make a continuum image, there are many arguments that need to be specified.

- The field which represents the object that needs to be imaged can be found with the *listobs* command.
- The spectral window that works best for making a continuum image, is the one with the largest 'ChanWid', which can be found with the *listobs* command as well. → If there are multiple spectral windows with the same channel width, they can either be imaged all together or one window can be chosen.
- The lines should be excluded when making a continuum. 'plotms' can be used to detect line emission. The lines can then either be flagged using the *flagdata* command or the channels that represent the lines can simply be excluded in the channel range when cleaning the image, so these channels should be noted down.
- 'plotms' can also be used to calculate the cell and image size, which are needed to clean the image later:

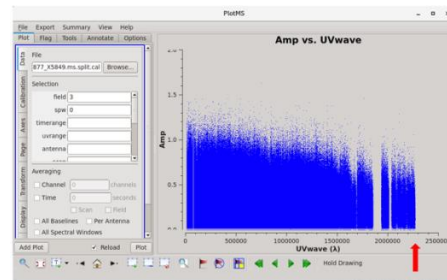
The cell size, in arc seconds, can be calculated using the following formula:

$$Cell = \frac{206265}{\text{longest baseline in wavelength} * \text{number of cells across the beam.}}$$

The longest base line is the wavelength where the visibility's end, if UVwave (which is the baseline-length in wavelengths) is plotted on the x-axis (see figure). The rule of thumb for the number of cells across the beam is 5 cells.

The image size can be found by calculating the Half Power Beam Width of the Primary Beam which is calculated using:

$HPBW = \frac{1.02}{\lambda D}$ and should be multiplied by some factor (1.5-2).



Case 2: Moment map

For the moment map, the cube needs to be inspected, using the CARTA application at the ALMA archive. To analyze the cube, the layout setting under the 'view' needs to be set to 'Cube Analysis'. To scroll through the cube the slider for channels can be used. Now the channels need to be noted down that show intensity peaks, since those are the channels that needs to be used for the moment maps in step 6.

Step 5 – Cleaning the calibrated measurement set

The calibrated measurement set should be cleaned, making a continuum image, a cube or both. For cleaning the image, the command *tclean* should be used. The *tclean* command has many input arguments which should be specified based on the data and imaging preferences.

Use the argument **inp tclean** to get a list of all arguments:

```

IPython: member.uid..._A00L_X8c5_X62/calibrated
File Edit View Search Terminal Help
# tclean -- Radio Interferometric Image Reconstruction
vis = '' # Name of input visibility file(s)
selectdata = True # Enable data selection parameters
field = '' # field(s) to select
spw = '' # spw(s)/channels to select
timerange = '' # Range of time to select from data
uvrange = '' # Select data within uvrange
antenna = '' # Select data based on antenna/baseline
scan = '' # Scan number range
observation = '' # Observation ID range
intent = '' # Scan Intent(s)
datacolumn = 'corrected' # Data column to image(data,corrected)
imagename = '' # Pre-name of output images
imsize = [100] # Number of pixels
cell = [] # Cell size
phasecenter = '' # Phase center of the image
stokes = 'I' # Stokes Planes to make
projection = 'SIN' # Coordinate projection
startmodel = '' # Name of starting model image
specmode = 'mfs' # Spectral definition mode (mfs,cube,cubedata,
# cubesource)
reffreq = '' # Reference frequency
gridding = 'standard' # Gridding options (standard, wproject, widefield,
# mosaic, wproject)
vptable = '' # Name of Voltage Pattern table
pblimit = 0.2 # PB gain level at which to cut off normalizations
deconvolver = 'hogbom' # Minor cycle algorithm
# (hogbom,clark,multiscale,mtmfs,mem,clarkstokes)
restoration = True # Do restoration steps (or not)
restoringbeam = [] # Restoring beam shape to use. Default is the PSF main
# lobe
pbcor = False # Apply PB correction on the output restored image
outlierfile = '' # Name of outlier-field image definitions
weighting = 'natural' # Weighting scheme (natural,uniform,briggs,
# briggsabs[experimental],
# briggsbtaper[experimental])
# uv-taper on outer baselines in uv-plane
uvtaper = []
niter = 0 # Maximum number of iterations
usemask = 'user' # Type of mask(s) for deconvolution: user, pb, or
# auto-multithresh
mask = '' # Mask (a list of image name(s) or region file(s) or
# region string(s) )
pbmask = 0.0 # primary beam mask
fastnoise = True # True: use the faster (old) noise calculation. False:
# use the new improved noise calculations
restart = True # True : Re-use existing images. False : Increment
# imagename
savemodel = 'none' # Options to save model visibilities (none, virtual,
# modelcolumn)
calcrs = True # Calculate initial residual image
calcpfs = True # Calculate PSF
psfcutoff = 0.35 # All pixels in the main lobe of the PSF above

```

Case 1 – Continuum

Here the arguments are given that need to/ can be specified when producing a continuum:

- The name of the MS file should be specified -- **vis**
- The name of the new produced file should be specified -- **imagename**
- The spectral mode should be set to 'mfs' for a continuum -- **specmode**
- The field that represents the source, found in listobs, should be specified -- **field**
- The spectral window best suited for making a continuum should be specified -- **spw** + which is the spectral window with the largest 'ChanWid'.
- When specifying the spectral window, the channels that have lines should be excluded in this command, if they have not been flagged -- **spw**
- The image size should be specified in the arguments, this value can be found in the header of the continuum, if it already exists in the ALMA or JVO database, using the first two digits of 'shape'. Or the image size can be calculated using the HPBW of the primary beam as explained in step 4. -- **imsize**
- The pixel size can be specified in the argument 'cell'. This value can be found in the header under 'pixel increment' if available, or it can be calculated using the formula given in step 4. -- **cell**
- The maximum number of iterations can be specified in the arguments: -- **niter**
 - To produce a dirty image this value should be zero.
 - To produce a cleaned image, this value should be a large number, often. 10.000 is used.
- The weighting argument has three possibilities and should be specified -- **weighting**
 - The natural weighting results in a lower RMS noise level but also a lower angular resolution.
 - Uniform weighting results in a higher angular resolution, but the RMS noise will also be higher.
 - Briggs weighting is a compromise between the natural and uniform weighting, and has a robust parameter that sets the relative importance of uniform (robust = -2) and natural (robust = 2) weighting. Often the robust parameter of 0.5 is chosen but can be adjusted to preference.
- Tapering can be used to adjust the weighting of the visibilities, which can be useful to obtain a resolution that is comparable to another data set. -- **uvtaper**
- The way the mask is produced can be chosen. – **mask , usemask**
 - The mask can be set to automatic. Then the threshold can be set automatic as well or specified by the user based on the RMS threshold, often twice the RMS is used.
 - The mask can also be specified by the user by making the residual interactively. This can be useful if the mask needs to be changed after every iteration to see if sources of emission occur. The cleaning should stop when the image looks like the residual. – **interactive**

The *tclean* command will return a folder of images containing the main science image, the point spread function, the residual map, the model, the primary beam, the sum weight image.

More information on the arguments of *tclean* can be found here:

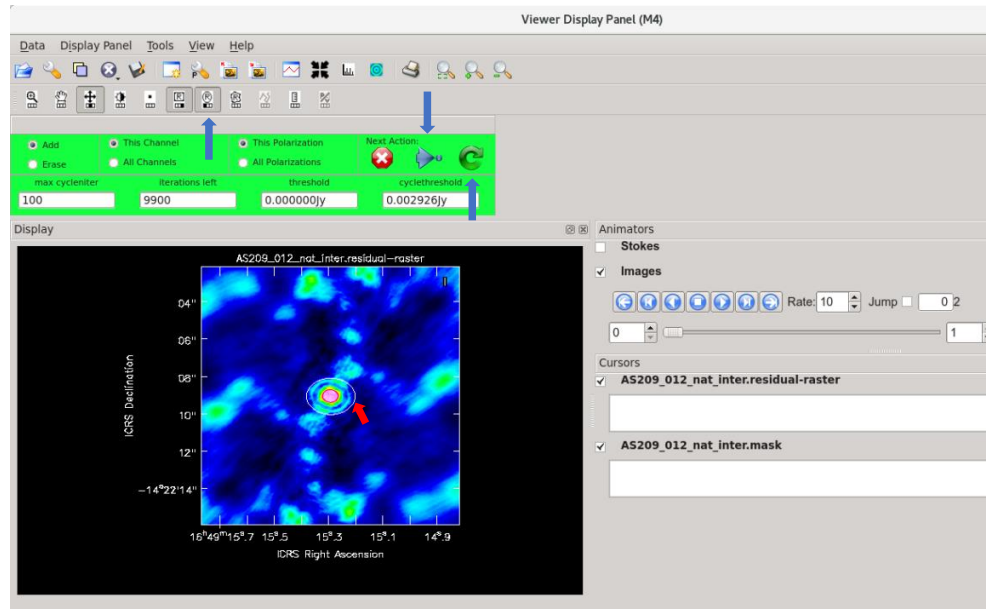
<https://casa.nrao.edu/docs/taskref/tclean-task.html>

Extra: Interactive cleaning

If there is enough time to use the interactive cleaning, it might be worth to try it out. For interactive cleaning the settings of `tclean` need to be:

`usemask = 'user'` and `interactive = 'True'`

When running `tclean`, the next window will appear:



The user should define a mask him/herself, by making use of the button with a circle or square on it. When the source is outlined, the form should be double clicked to be saved as a mask. Next the green circular arrow should be clicked, which will run a cleaning cycle. After each cycle a new mask can be made by first erasing the old mask and adding a new one using the circular check boxes on the left. If the cleaning process seems to happen all good and the process can continue automated, the blue arrow with a dot can be used, a threshold for stopping the cleaning process can be set by the user him/herself.

To produce a continuum, use the commands specified in step 3 (imaging) option 1 (Continuum map) of the script:

```
##### STEP 3: imaging #####
#### OPTION 1 : Continuum map ####
# Show the input arguments of tclean
inp tclean

# Use listobs to find the field that represents your source
# Use listobs to find the spectral window with the largest ChanWid
# Use plotms to find and note down the channels that have a line OR flag the line

# Select the ms file you want to make a continuum out of
vis = '<Your ms file>'

# Select the field
field = '< number >'

# Select the spectral window and the channels you want to use of each spectral window
spw = '<number spw>' ->begin channel-->end channel-'
# Example: '0:40-120'

# Name your output file containing the continuum
im名称 = '<Your specified output file name>'

# Specify image size based on header or calculations
# Use 1 number if square, and 2 if rectangular
insize = [<number>]

# Specify the pixel size based on header or calculations
cell = [<number><unit>]
# Example: cell = ['0.01arcsec']

# Specify your type of image, for continuum use 'rms'
specmode = 'rms'

# Set a maximum number of iterations
# To produce a dirty image use:
niter = 0
# To produce a continuum: set to a large number.
niter = 10000

# Select the weighting type
weighting = '<Type>'
# If briggs weighting is used:
(robust = <number between -2 and 2>)

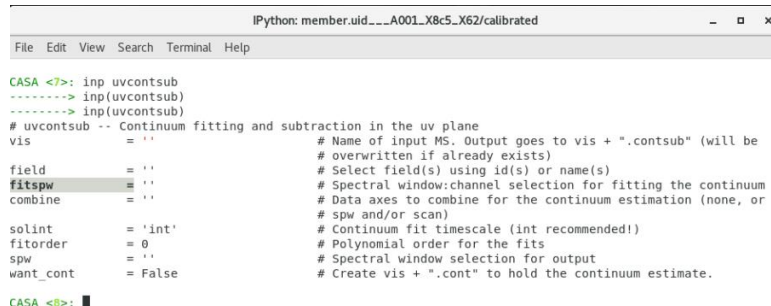
##IF you want to use interactive cleaning and make the mask yourself:
usemask = 'user'
interactive = True

# IF you want the mask to be made automatic:
usemask = 'auto-multithresh'
interactive = False
```

Case 2 – Data cube for moment map

The command 'uvcontsub' can be used to subtract the continuum from the MS file and produce a new MS.contsub file, from which a data cube can be made.

Use the argument **inp uvcontsub** to get all arguments:



```

IPython: member.uid...A001_X8C5_X62/calibrated
File Edit View Search Terminal Help

CASA <7>: inp uvcontsub
-----> inp(uvcontsub)
-----> inp(uvcontsub)
# uvcontsub -- Continuum fitting and subtraction in the uv plane
vis           = ''           # Name of input MS. Output goes to vis + ".contsub" (will be
                        # overwritten if already exists)
field         = ''           # Select field(s) using id(s) or name(s)
fitspw       = ''           # Spectral window: channel selection for fitting the continuum
combine      = ''           # Data axes to combine for the continuum estimation (none, or
                        # spw and/or scan)
solint       = 'int'        # Continuum fit timescale (int recommended!)
fitorder     = 0            # Polynomial order for the fits
spw          = ''           # Spectral window selection for output
want_cont    = False        # Create vis + ".cont" to hold the continuum estimate.

CASA <8>: █

```

Some important arguments of uvcontsub

- Name of the MS file should be specified -- **vis**
- The field that represents source should be specified -- **field**
- What spectral windows that are useful should be specified -- **spw**
- Channels per spectral window can be specified -- **fitspw**
- If the channels specified in fitspw needs to be excluded – **Excludechans**

To make a data cube from the new MS.contsub file, **tclean** is used. Most arguments are given at Case 1. But note that there are some differences:

- The spectral mode should be 'cube' when a data cube is produced -- **specmode**
- The channels that have line emission should NOT be excluded
- The spectral window does not have to be the one with the largest Chanwid. All spectral windows can be included. – **spw**

To make a data cube, the commands can be found at step 3 (imaging), option 2 (moment map), step 1 (making a data cube), of the instructions:

```

#### OPTION 2: moment map ####
## STEP 1: making a data cube ##
# Subtract the continuum from the ms file to obtain a calibrated data cube

# Show the input arguments of uvcontsub:
inp uvcontsub

# Select the ms file from which you want to make a cube
vis = '<Name of ms file>'

# Select the correct field
field = '<number>'

# Select the spectral windows you want to use + the appropriate channels per spectral window
fitspw = '<spectral window>: <begin channel> -- <end channel>, <repeat for different spectral windows>'
Example: fitspw = '0: 80-200, 1: 50-100; 150-200, 2'

# If the channels listed in above represent the lines, the channels should be excluded:
excludechans = True

# If the channels did already represent the continuum, the channels need to be included.
excludechans = False

# Use tclean to make a data cube
inp tclean
vis = '<contsub file >'
imagename = '<New data cube name>'
specmode = 'cube'
msize = [<Number>]
cell = [<Number>:<freq>]
nter = 0 OR 10000
usemask = 'auto-multithresh'

# Add rest frequency of the line if known, otherwise correct the velocities later
restfreq = '<Freq line>-GHz'

```

Step 6 – Producing a moment map

A data cube is used for line imaging, as it contains a full spectrum of every point in the image. A moment map means 'collapsing' one of these axes to gather a value from the combined moment axis into 1 pixel. A moment 0 map essentially gives the amount of gas at a certain point, whereas a moment 1 map essentially tells whether the gas is moving towards or away from the observer and thus gives information on the kinematics.

The data cube which is needed for the moment maps is can either be downloaded directly from the ALMA archive or can be produced out of the calibrated MS file. The command used for producing moment maps is *immoments*, and has different arguments to specify.

Use the argument `inp immoments` to get all arguments:

```

IPython: member.uid_...A001_X8c5_X62/calibrated
File Edit View Search Terminal Help
CASA <5>: inp immoments
-----> inp(immoments)
-----> inp(immoments)
# immoments -- Compute moments from an image
imagename = '' # Name of the input image
moments = [0] # List of moments you would like to compute
axis = 'spectral' # The moment axis: ra, dec, lat, long,
# spectral, or stokes
region = '' # Region selection. Default is to use the
# full image.
box = '' # Rectangular region(s) to select in
# direction plane. Default is to use the
# entire direction plane.
chans = '' # Channels to use. Default is to use all
# channels.
stokes = '' # Stokes planes to use. Default is to use
# all Stokes planes.
mask = '' # Mask to use. Default is none.
includepix = -1 # Range of pixel values to include
excludepix = -1 # Range of pixel values to exclude
outfile = '' # Output image file name (or root for
# multiple moments)

CASA <6>:

```

Most important arguments that need to be specified:

- All moment maps ranging from -1 till 11 can be specified or created together. The meaning of all moment maps can be found at: <https://casa.nrao.edu/docs/taskref/immoments-task.html>
- The axis over which to collapse can also be specified in the arguments. For a moment 0 or 1 map, the axis of collapse is the spectral axis, which is also the default.
- There are different arguments to specify what selected part of the cube needs to be imaged: e.g. a box, a certain region, a polarization plane (stokes) or the useful channels.
- The channels that show line emission, when the cube is analyzed in CARTA, need to be selected.
- An argument to specify a mask that contains information on what parts of the data needs to be imaged and which cannot be used
- An argument to include or exclude pixels with a certain value of intensity for example to neglect the noise level, can be used
 - For a moment 0 map this argument should be neglected, as all signal should be included.
 - For the moment 1 map this argument should be specified, to make sure only the signal is imaged of about 3 times the RMS level.

More information on the command *immoments* can be found at <https://casa.nrao.edu/docs/taskref/immoments-task.html> .

To make a moment map the commands can be found at step 3 (imaging), option 2 (moment map), step 2 (making a moment map) of the instructions:

```
## Step 2: making a moment map ##
# Show what input arguments there are for the command 'mmoments'
no mmoments

# Select the file containing the datacube of which you want to make a moment map
imagenam = '<YourFilename>'

# Pick what moment map you want to make
# Moment 0 gives integrated spectrum
# Moment 1 gives velocity fields
moments = [-<Number>]

# Select the axis over which it will collapse, depending on the moment map
# For moment 0 and 1 the spectral axis can be used
axis = 'spectral'

# Pick the channels that show emission, by looking at the cube with CARTA
Chan = '<Begin>--<End>'
example: '200--300'

# To select a certain region or box you want to consider instead of the full image
box = '<Your box>'
region = '<Your preferred region >'

# To select a polarization plane
stokes = '<Your plane >'

# Specify which parts of the image you want to use and which you don't, using a mask
mask = '<Your mask>'

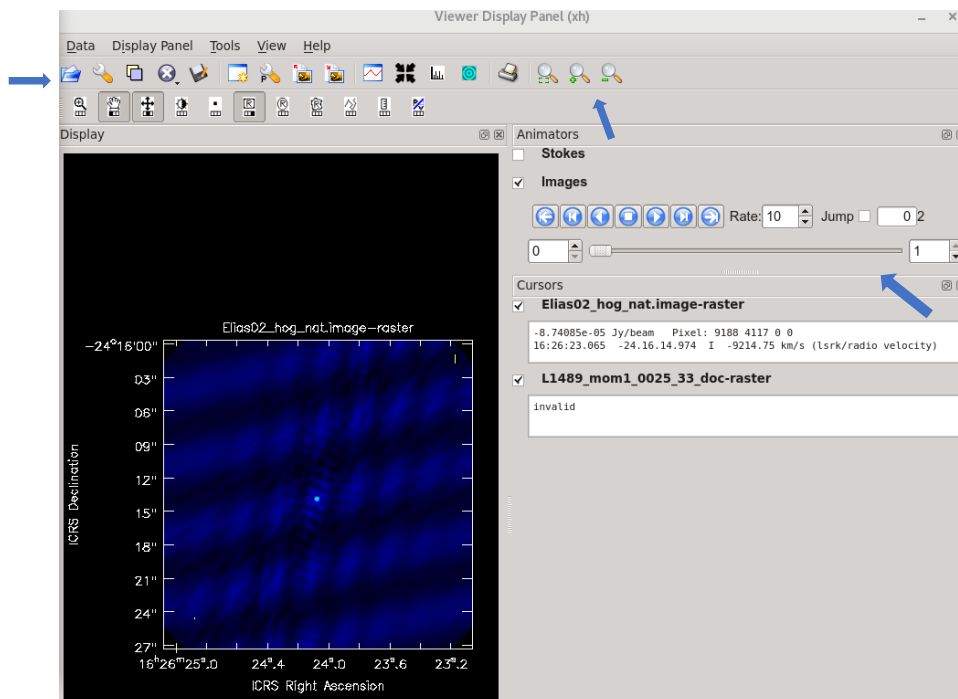
# Pick what pixels you want to include based on their intensity to only include the signal
# Use as lower bound about 3 times the RMS value and upper bound a high number
includepix = [-<3sigma>, 100]

# Pick what pixels you want to exclude based on their intensity to exclude the noise
excludepix = [-<Fill in>,<Fill in>]

# Name your output file containing your moment map: be specific
outfile = '<YourOutputFile>'
```

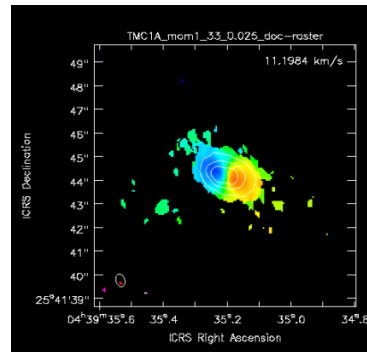
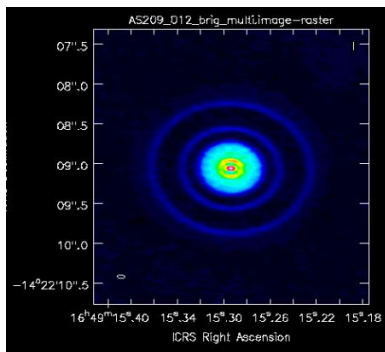
Step 7 – Observe the produced images

To view the images produced the command *imview* should be used so the viewer panel will show up. Files can be opened with the directory pictogram in the left corner. For a continuum image or a moment map 1 the image should be loaded as raster image, whereas moment 0 map can be loaded as contour map. In the data viewer there are buttons to zoom in and out and drag the image around. The scroll bar in the right can be used to switch between images opened at the same time, useful for comparing images with different settings.



These instructions can be used to make a continuum image out of the raw data and to make a moment map from a selected data cube. The exact commands to produce a continuum image or a moment map image can be found in the accompanying script for imaging.

The left image shows a continuum map, with briggs weighting, a multiscale deconvolver and selected channels and spectral windows. The right image shows a moment 1 map in color, and a moment 0 map in contours.



10.3 Script for imaging

The next few pages show a txt script produced for imaging a moment map or a continuum image in pdf format.


```

##### This script is for imaging moment maps and the continuum out of ALMA data #####
##### Recommend to use this together with the instructions

## NOTE: < Fill in your self >

##### STEP 1: Calibration #####
## Reducing data, making an MS file

# Download auxiliary and raw data from ALMA archive
# Untar or extract the files
# Open the right version of CASA
# Execute the script for PI in the 'script' directory
execfile('scriptForPI.py')

##### STEP 2 : Inspection #####

# List the properties of the MS file
listobs( vis = '<Your ms file>' )

# Show the input arguments of plotms
inp plotms

# Plot the visibilities for the right field and spectral window
# If more than 1 spw is useful, iterate over spectral windows
plotms( vis = '<Your ms file>' ,
        xaxis = 'channels',
        yaxis = 'amplitude'
        field = '<Your appropriate field>' ,
        spw = '< chosen spectral window>' OR iteraxis = 'spw' )

##### STEP 3: imaging #####

##### OPTION 1 : Continuum map #####

# Show the input arguments of tclean
inp tclean

# Use listobs to find the field that represents your source
# Use listobs the find the spectral window with the largest ChanWid
# Use plotms to find and note down the channels that have a line OR flag the line

# Select the ms file you want to make a continuum out of
vis = '<Your ms file>'

# Select the field
field = '< number >'

# Select the spectral window and the channels you want to use of each spectral window
spw = '<number spw> : <begin channel> ~ <end channel>'
# Example: ' 0:40~120 '

# Name your output file containing the continuum

```

```

imagername = ' <Your specified output file name> '

# Specify image size based on header or calculations
# Use 1 number if square, and 2 if rectangular
imsize = [ <number> ]

# Specify the pixel size based on header or calculations
cell = [ ' <number><unit>' ]
# Example: cell = ['0.01arcsec']

# Specify your type of image, for continuum use 'mfs'
specmode = 'mfs'

# Set a maximum number of iterations
# To produce a dirty image use:
niter = 0
# To produce a continuum: set to a large number.
niter = 10000

# Select the weighting type
weighting = '<Type>'
# If briggs weighting is used:
(robust = <number between -2 and 2>)

##IF you want to use interactive cleaning and make the mask yourself:
usemask = 'user'
interactive = True

# IF you want the mask to be made automatic:
usemask = 'auto-multithresh'
interactive = False

##### OPTION 2: moment map #####

## STEP 1: making a data cube ##
# Subtract the continuum from the ms file to obtain a calibrated data cube

# Show the input arguments of uvcontsub
inp uvcontsub

# Select the ms file from which you want to make a cube
vis = '<Name of ms file> '

# Select the correct field
field = ' <number> '

# Select the spectral windows you want to use + the appropriate channels per spectral window
fitspw = '<spectral window> : <begin channel> ~ < end channel> , <repeat for different spectral
windows>'
Example: fitspw = '0: 80~200, 1: 50~100; 150~200 , 2 '

# If the channels filled in above represent the lines, the channels should be excluded:
excludechans = True

# If the channels did already represent the continuum, the channels need to be included.

```

```

excludechans = False

# Use tclean to make a data cube
inp tclean
vis = '<contsub file >'
imagename = '<New data cube name>'
specmode = 'cube'
imsize = [<Number>]
cell = [<number>arcsec]
niter = 0 OR 10000
usemask = 'auto-multithresh'

# Add rest frequency of the line if known, otherwise correct the velocities later
restfreq = '<Freq line>GHz'

## STEP 2: making a moment map ##

# Show what input arguments there are for the command 'immoments'
inp immoments

# Select the file containing the datacube of which you want to make a moment map
imagename = '<YourFilename>'

# Pick what moment map you want to make
# Moment 0 gives integrated spectrum
# Moment 1 gives velocity fields
moments = [<Number>]

#Select the axis over which it will collapse, depending on the moment map
# For moment 0 and 1 the spectral axis can be used
axis = 'spectral'

# Pick the channels that show emission, by looking at the cube with CARTA
Chans = '<Begin> ~ <End>'
example: '200~300'

#To select a certain region or box you want to consider instead of the full image
box = '<Your box>'
region = < Your preferred region >

# To select a polarization plane
stokes = '<You plane >'

# Specify which parts of the image you want to use and which you don't, using a mask
mask = '<Your mask>'

# Pick what pixels you want to include based on their intensity to only include the signal
# Use as lower bound about 3 times the RMS value and upper bound a high number
includepix = [ <3sigma> , 100 ]

# Pick what pixels you want to exclude based on their intensity to exclude the noise
excludepix = [<Fill in>,<Fill in>]

# Name your output file containing your moment map:be specific
outfile = '<YourOutputFile>'

```

10.4 Script for implementing data in planetarium

The next few pages show a txt script produced for implementing images in a planetarium show, in pdf format.

```
##### Implementing the images in SkyScan #####

## Loading images onto to dome

##### Text Add #####
# Specify the name and path of the image
Text Add "<Name object>" "<File Path>" <Pixel Width> <Pixel Height> <Coordinate
system> <Maximum size image> <X location origin image> <Y location origin image> <Type
of lens distortion effects> <MIP Map Level>

###Notes for arguments Text Add
# The pixel width and height need to be a power of 2
# Coordinate systems: -1 = Equal, 0 = local (Alt/Az), 1 = Equat, 2 = sidereal (Ra / Dec), 3=
precess, 4 = Eclip
# Maximum radius is in degrees
# X location: -0.5 is left and 0.5 is right. Y location: -0.5 is top, 0.5 is bottom
# Lens type: -1 = Full screen without rectilinear geometrical correction
0 = normal lens
1 = Fisheye lens
2 =Panoramic lens
# MIP Map Level, 0 =activating map, 1 = one surface

# Add a delay time, so not all processes try to run at the same time.
+ 1

##### Text Locate #####
# Give the right location to the image

Text Locate <Name object> <Rate time to complete function> <X location object> <Y
location object> <Rotation angle object> <Scaled image width> <Scaled image height>

###Notes for arguments Text Locate
# The Rate time can also be specified with acceleration and deceleration components —>
see Rate Time parameter
# X and Y location of centre of object depending on your coordinate system specified in Text
Add
# Rotation angles in degrees: negative is clockwise, positive is counterclockwise.
# Scale width and hight are in degrees, # used for preserving original aspect ratio
# NOTE: Locate text can be done later as well, so flying images can be created

##### Text view #####
# Display the loaded and placed images

Text View <Name object> <Rate time to complete function> <Opacity image> <Red
brightness> <Green brightness> <Blue brightness>

### Notes fot arguments Text view
# Opacity: 0 is completely transparant while 100 is completely opaque
# The colors are all in percentage of brightness
```

```

# Add a button text switch for simplicity for the operator
  ButtonText = " ....."
STOP

##### Text remove #####
Text remove <Name object>

##### Example #####
#Make an image appear on the dome looking like it's magnified from the right location and
let it move to a different location

# The sun is loaded from the directory: Example. The size is set to 1024x512 pixels, the
sidereal coordinate system is chosen. The maximum radius of image is set to 90
degrees. The Origin is in the centre of the image, the Fisheye lens distortion effect is applied,
and the MIP mapping is not used.
Text Add "Sun" "ShowPath\Example\sun.jpg" 1024 512 2 90 0 0 1 1

# Wait 1 second before next process happens
+1

# View the image over 0 seconds, to 100% opacity and at full brightness of all colors
Text View Sun 0 100 100 100 100

# Let the image be located at a Right Ascension of 10:0:0 and a declination of +13:0:0. The
image is not rotating and its scale width and height is zero, to make the image enlarge
Text Locate Sun 0 10 +13 0 0 0

# The image of the sun is now located at the same location, and will get a width of 20
degrees and a height that is scaled to the width to maintain the original aspect ratio over a
timescale of 3 seconds.
Text Locate Sun 3 10 +13 0 20 #

# Make the button change name so the operator knows what the next step is
  ButtonText = "Move Sun"
STOP

# Let the object with the same settings is moved to a different location: Right Ascension of
10:0:0 and a declination of -13:0:0
Text locate Sun 3 10 -13 0 20 #

# Make the button change name so the operator knows what the next step is
  ButtonText = "Remove Sun"
STOP

# Let the image of the sun be faded away to be fully transparent in 1 second
Text view Sun 1 0

```

```
# Add a small waiting time after this command  
+1  
  
# Let the image be removed  
Text Remove Sun
```